UNIVERSITY OF CALIFORNIA SAN DIEGO

Materials Engineering for Compatible Chemistries in Sodium Solid-State-Batteries and Thin-Film Solid Oxide Fuel Cells

A dissertation submitted in partial satisfaction of the
requirements for the degree Doctor of Philosophy

in

NanoEngineering

by

Erik Austin Wu

Committee in charge:

Ying Shirley Meng, Chair
Eric Fullerton
Jian Luo
Nguyen Minh
Shyue Ping Ong
Michael Sailor

2020

The dissertation of Erik Austin Wu is approved, and it is acceptable in quality and form for publication on microfilm and electronically:

_____

_____

_____

_____

_____

_____
Chair

University of California San Diego

2020

DEDICATION

To my family, for their unwavering support and encouragement.

TABLE OF CONTENTS

LIST OF ABBREVIATIONS

AAO: Anodized Aluminum oxide

AB: Acetylene Black

AIMD: Ab-initio Molecular Dynamics

ALD: Atomic Layer Deposition

ASSB: All-Solid-State Battery

a.u.: Arbitrary Units

C: Carbon

CEI: Cathode-Electrolyte Interphase

CO_2: Carbon Dioxide

cps: Counts per second

CV: Cyclic Voltammetry

CVD: Chemical Vapor Deposition

DFT: Density Functional Theory

EELS: Electron Energy Loss Spectroscopy

EIS: Electrochemical Impedance Spectroscopy

eV: Electron Volt

GDC: Gadolinium-doped Ceria

HAADF: High-Angle Annular Dark Field (imaging)

I-V: Current-Voltage

I-P: Current-Power

LBO: Lithium Borate

LE: Liquid Electrolyte

LiIn: Lithium-Indium Alloy

LNO: Lithium Niobate

LPSCl: Li_6PS_5Cl

LSCF: Lanthanum Strontium Cobalt Ferrite

LSM: Lanthanum Strontium Manganite

LTO: Lithium Titanate

MSD: Mean-squared Displacement

MPa: Megapascal

Na: Sodium

NAS: Na_3SbS_4, Sodium Antimony Sulfide

NASICON: Na Superionic Conductor

Na_2S: Sodium Sulfide

NCM811: $LiNi_{0.8}Co_{0.1}Mn_{0.1}O_2$

NPS: Na_3PS_4

NPSC: Cl-doped Na_3PS_4

NYC: Na_3YCl_6

NYZC: $Na_{3-x}Y_{1-x}Zr_xCl_6$

NZC: Na_2ZrCl_6

ORR: Oxygen Reduction Reaction

PEEK: Polyether ether ketone

PLD: Pulsed Laser Deposition

PVD: Physical Vapor Deposition

SEM: Scanning Electron Microscopy

SOFC: Solid Oxide Fuel Cell

SE or SSE: Solid(-State) Electrolyte

SEI: Solid-Electrolyte Interphase

SSEI: Sodium (Na) Solid-Electrolyte Interphase

SSSB: Sodium Solid-State Battery

STEM: Scanning Transmission Electron Microscopy

TEM: Transmission Electron Microscopy

TF-SOFC: Thin-Film Solid Oxide Fuel Cell

VGCF: Vapor-grown carbon fiber

XPS: X-ray Photoelectron Spectroscopy

XRD: X-ray Diffraction

YSZ: Yttria-Stabilized Zirconia

LIST OF FIGURES

LIST OF TABLES

ACKNOWLEDGEMENTS

I would like to thank my advisor Professor Ying Shirley Meng for all the opportunities and for her guidance in helping to develop my approach to research. I would also like to recognize my committee, Professor Shyue Ping Ong, Professor Jian Luo, Professor Eric Fullerton, Professor Michael Sailor, and Dr. Nguyen Minh.

I am extremely thankful for the team members on the solid-state project, Dr. Han Nguyen, Chris Kompella, Dr. Abhik Banerjee, Dr. Jean-Marie Doux, Darren Tan, Grayson Deysher, Yu-Ting Chen, and Dr. Enyue Zhao, as over the years the team has always gotten along very well and has continued to work very effectively. Their input and contributions were paramount, and I was very fortunate to work with such great colleagues.

I would like to thank the solid oxide fuel cell project team, Dr. Yoon Ho Lee, Haowen Ren, Dr. Nguyen Minh, and Dr. Tuyen Tran, for all their hard work, contributions, and discussions. It was a pleasure to work with everyone on the project.

I would also like to thank my collaborators: Dr. Shyue Ping Ong's Materials VirtualLab (Dr. Iek-Heng Chu, Dr. Zhuoying Zhu, Dr. Hanmei Tang, Dr. Swastika Banerjee, and Ji Qi) for all of their hard work and for the invaluable computational contributions to the solid-state research. I would also like to acknowledge Dr. Raphaële Clément's group at UCSB (Dr. Peter Richardson) for NMR, and Dr. Karena Chapman's group (Dr. Antonin Grenier) at Stony Brook for their help with synchrotron XRD and the helpful discussions.

I would like to thank my family and friends for giving me their support during my time at UCSD.

I would like to thank my other colleagues in Professor Shirley Meng's group: Dr. Thomas Wynn, Dr. Jungwoo Lee, and Dr. Hyeseung Chung for their assistance in experimental planning and data gathering, especially for XPS and TEM.

I acknowledge the financial support from the National Science Foundation's Designing Materials to Revolutionize and Engineer our Future (DMREF) program under Grant No. 1436976,

from the Energy & Biosciences Institute through the EBI-Shell program, contract number PT78832, from LG Chem through the Battery Innovation Contest (BIC) program, and from the U. S. Department of Energy/National Energy Technology Laboratory (DOE/NETL) under the Cooperative Agreement DE-FE0026211.

XPS was performed at the University of California, Irvine Materials Research Institute (IMRI) using instrumentation funded in part by the National Science Foundation Major Research Instrumentation Program under grant no. CHE-1338173. Characterization work was performed in part at the San Diego Nanotechnology Infrastructure (SDNI), a member of the National Nanotechnology Coordinated Infrastructure, which is supported by the National Science Foundation under grant no. ECCS-1542148. Some of the computational work mentioned were performed using the Extreme Science and Engineering Discovery Environment (XSEDE), which is supported by National Science Foundation grant number ACI-1053575. TEM work was also performed at the UC Irvine Materials Research Institute (IMRI).

I acknowledge the assistance from the UCSD Crystallography Department, Dr. Milan Gembicky and Dr. Han Nguyen, for their assistance on air-sensitive capillary XRD measurements and their willingness to discuss data and experiments at all times.

Chapter 1, in part, is a reprint of the material “Interfaces and Interphases in All-Solid-State Batteries” as it appears in Chemical Reviews. Banerjee, A.*, Wang, X.*, Fang, C., Wu, E. A., and Meng, Y. S. 2020, 120, 6878-6933. The dissertation author was one of the authors of this paper and all authors contributed.

Chapter 2, in full, is a reprint of the material “New Insights into the Interphase between the Na Metal Anode and Sulfide Solid-State Electrolytes: A Joint Experimental and Computational Study” as it appears in ACS Applied Materials and Interfaces. Wu, E. A.*, Kompella, C. S., Zhu, Z., Lee, J. Z., Lee, S. C., Chu, I.-H., Nguyen, H., Ong, S. P., Banerjee, A., and Meng, Y. S. 2018, 10, 12, 10076-10086. The dissertation author was the first author of this paper. The dissertation author carried out all the experiments and electrochemical testing herein, except for the

NPS/NPSC electrochemical testing and XPS for NPS/NPSC, which were carried out by Kompella, C. S., and Lee, J. Z.

Chapter 3, in part, has been submitted for publication as “A Stable Cathode-Solid Electrolyte Composite for Long-Cycle-Life, High Voltage Solid-State Sodium-ion Batteries” in Nature Energy. Wu, E. A.*, Banerjee, S.*, Tang, H.*, Richardson, P. M., Doux, J.-M., Qi, J., Zhu, Z., Grenier, A., Li, Y., Zhao, E., Deysher, G., Nguyen, H., Stephens, R., Verbist, G., Chapman, K. W., Clément, R. J., Banerjee, A., Meng, Y. S., and Ong, S. P. The dissertation author was one of the three co-first authors for this study. The dissertation author carried out all the sample preparation, the experiments, and electrochemical testing.

Chapter 4, in full, has been submitted for publication as “A Facile, Dry-Processed Lithium Borate-Based Cathode Coating for Improved All-Solid-State Battery Performance” in the Journal of the Electrochemical Society. Wu, E. A.*, Jo, C.*, Tan, D. H. S., Zhang, M., Doux, J.-M., Chen, Y.-T., Deysher, G., and Meng, Y. S. The dissertation author was the one of the two co-first authors for this study; Wu, E. A. wrote the paper while Jo, C. did most of the experiments. All authors had input on the paper.

Chapter 5, in part, is a reprint of the material “All-Sputtered, Superior Power Density Thin-Film Solid Oxide Fuel Cells with a Novel Nanofibrous Ceramic Cathode” as it appears in Nano Letters. Lee, Y. H.*, Ren, H.*, Wu, E. A.*, Fullertron, E. E., Meng, Y. S., and Minh, N. Q. 20, 5, 2943–2949. The dissertation author was one of the three co-first authors for this study. The dissertation author performed FIB/SEM characterization as well as electrochemical analysis.

VITA

2011 Bachelor of Science, Materials Science and Engineering, University of California Berkeley

2016 Master of Science, NanoEngineering, University of California San Diego

2020 Doctor of Philosophy, NanoEngineering, University of California San Diego

PUBLICATIONS

(* = authors contributed equally to the work)

1. Nguyen, H., Hy, S., Wu, E. A., Deng, Z., Samiee, M., Yersak, T., Luo, J., Ong, S. P., and Meng, Y. S. Experimental and Computational Evaluation of a Sodium-Rich Anti-Perovskite for Solid State Electrolytes. *Journal of the Electrochemical Society* **2016**, 163**,** 10, A2165-A2171 (2016).

2. Wu, E. A.*, Kompella, C. S., Zhu, Z., Lee, J. Z., Lee, S. C., Chu, I.-H., Nguyen, H., Ong, S. P., Banerjee, A., and Meng, Y. S. New Insights into the Interphase between the Na Metal Anode and Sulfide Solid-State Electrolytes: A Joint Experimental and Computational Study. *ACS. Appl. Mater. Interfaces* **2018**, 10, 12, 10076-10086.

3. Parikh, P., Sina, M., Banerjee, A., Wang, X., D'Souza, M., Doux, J.-M., Wu, E. A., Trieu, O. Y., Gong, Y., Zhou, Q., Snyder, K., and Meng, Y. S. Role of Polyacrylic Acid (PAA) Binder on the Solid Electrolyte Interphase in Silicon Anodes. *Chem. Mater.* **2019**, 31, 7, 2535-2544.

4. Nguyen, H., Banerjee, A., Wang, X., Tan, D. H. S., Wu, E. A., Doux, J.-M., Stephens, R., Verbist, G., and Meng, Y. S. Single-step synthesis of highly conductive Na_3PS_4 solid electrolyte for sodium all-solid-state batteries. *J. Power Sources* **2019**, 435, 126623.

5. Tan, D. H. S., Wu, E. A., Nguyen, H., Chen, Z., Marple, M. A. T., Doux, J.-M., Wang, X., Yang, H., Banerjee, A., and Meng, Y. S. Elucidating Reversible Electrochemical Redox of Li_6PS_5Cl Solid Electrolyte. *ACS Energy Lett.* **2019**, 4, 2418-2427.

6. Tan, D. H. S., Banerjee, A., Deng, Z., Wu, E. A., Nguyen, H., Doux, J.-M., Wang, X., Cheng, J.-H., Ong, S. P., Meng, Y. S., and Chen, Z. Enabling Thin and Flexible Solid-State Composite Electrolytes by the Scalable Solution Process. *ACS Appl. Energy Mater.* **2019**, 2, 9, 6542-6550.

7. Banerjee, A., Tang, H., Wang, X. Cheng, J.-H., Nguyen, H., Zhang, M., Tan, D. H. S., Wynn, T. A., Wu, E. A., Doux, J.-M., Wu, T., Sterbinsky, G. E., D'Souza, M. S., Ong, S. P., and Meng, Y. S. Revealing Nanoscale Solid-Solid Interfacial Phenomena for Long-Life

and High-Energy All-Solid-State Batteries. *ACS Appl. Mater. Interfaces* **2019**, 11, 46, 43138-43145.

8. Doux, J.M., Nguyen, H., Tan, D. H. S., Banerjee, A., Wang, X., Wu, E. A., Jo, C., Yang, H., and Meng, Y. S. Stack Pressure Considerations for Room-Temperature All-Solid-State Lithium Metal Batteries. *Adv. Energy Mater.* **2020**, 10, 1, 1903253.

9. Lee, Y. H.*, Ren, H.*, Wu, E. A.*, Fullertron, E. E., Meng, Y. S., and Minh, N. Q. All-Sputtered, Superior Power Density Thin-Film Solid Oxide Fuel Cells with a Novel Nanofibrous Ceramic Cathode. *Nano Lett.* **2020**, 20, 5, 2943–2949.

10. Banerjee, A., Wang, X., Fang, C. Wu, E. A., and Meng, Y. S. Interfaces and Interphases in All-Solid-State Batteries with Inorganic Solid Electrolytes. *Chemical Reviews* **2020**, 120, 14, 6878–6933.

11. Ren, H., Lee, Y. H., Wu, E. A., Chung, H., Meng, Y.S., Fullerton, E. E., and Minh, N. Nano-Ceramic Cathodes via Co-sputtering of Gd-Ce Alloy and Lanthanum Strontium Cobaltite for Low-Temperature Thin-Film Solid Oxide Fuel Cells. Accepted, *ACS Applied Energy Materials.*

12. Wu, E. A.*, Jo, C.*, Tan, D. H. S., Zhang, M., Doux, J.-M., Chen, Y.-T., Deysher, G., and Meng, Y. S. A Facile, Dry-Processed Lithium Borate-Based Cathode Coating for Improved All-Solid-State Battery Performance. Accepted, *J. Electrochem. Soc.*

13. Wu, E. A.*, Banerjee, S.*, Tang, H.*, Richardson, P. M., Doux, J.-M., Qi, J., Zhu, Z., Grenier, A., Li, Y., Zhao, E., Deysher, G., Nguyen, H., Stephens, R., Verbist, G., Clément, R. J., Banerjee, A., Meng, Y. S., and Ong, S. P. A Stable Cathode-Solid Electrolyte Composite for Long-Cycle-Life, High Voltage Solid-State Sodium-ion Batteries. Submitted.

ABSTRACT OF THE DISSERTATION

Materials Engineering for Compatible Chemistries in Sodium Solid-State-Batteries and Thin-Film Solid Oxide Fuel Cells

by

Erik Austin Wu

Doctor of Philosophy in NanoEngineering

University of California San Diego, 2020

Professor Ying Shirley Meng, Chair

Energy storage and conversion devices need to continue to develop to keep up with the ever-increasing global energy consumption. As the percentage of energy coming from renewable sources continues to rise, a cost-effective and safe solution to store the generated energy must

also be implemented. In this regard, all-solid-state batteries (ASSBs), which do not contain the flammable and corrosive liquid electrolyte, have been highly sought after, as they have the potential for enhanced energy density and safety in addition to lowered cost and reduced maintenance considerations.

Many classes of lithium-ion-conducting and sodium-ion-conducting solid-state electrolytes (SSEs) have been developed and reported over the years, and Na-based ASSBs have the potential for additional cost savings. Since are now many solid electrolytes with adequate ionic conductivity, our research focus turns to studying cell degradation mechanisms at the electrode/SSE interface, as understanding these mechanisms will enable the selection of compatible chemistries toward longer-lasting ASSBs.

In terms of energy conversion, Thin Film Solid Oxide Fuel Cells (TF-SOFCs) are of research interest as they can operate at lower temperatures than conventional SOFCs, allowing for a wider range of materials and lowered maintenance costs while far surpassing the fuel-to-electricity conversion efficiency compared to burning conventional fossil fuels. Applications for such high-power devices range from transportation to large-scale power plants.

In this dissertation, for the Na solid-state battery system, the reactivity between the Na anode and the Na_3SbS_4 electrolyte was studied to gain insight on cell degradation, and on the cathode side, a new, stable, halide chemistry, $Na_{3-x}Y_{1-x}Zr_xCl_6$, was evaluated for its compatibility when paired with the oxide cathode $NaCrO_2$. For the Li-based solid-state system, the properties of a dry-processed protective lithium borate coating on the $LiNi_{0.8}Co_{0.1}Mn_{0.1}O_2$ (NCM811) cathode were investigated, and lastly, a sputtering platform to fabricate an entire TF-SOFC was developed and tested in order to enable a more practical and scalable SOFC fabrication method. These methods to understand and develop stable, longer-lasting, and higher-performing materials will inform strategies to mitigate the effects of climate change and enable a cleaner energy future.

Chapter 1. Introduction

1.1 Motivation – The Need for Effective Energy Storage

As global energy demand continues to increase, there is also a correlated rise in CO_2 emissions and global temperatures, since even in the present day, much of the generated electricity comes from burning fossil fuels such coal and oil. Figure 1.1a shows the historical global temperature data, extrapolated to 2050 if current trends continue, and Figure 1.1b shows the historical CO_2 emissions.[1,2] To combat this trend, energy generation from renewable energy sources such as wind and solar have seen rapid growth, additionally due to the lowered costs of implementing renewables as they continue to be developed. Figure 1.2 shows the global breakdown of energy generation sources and it can be seen that renewables and natural gas are the two sources that are clearly gaining in market share or adoption, while all other sources have either stayed steady or slightly declined.[3]

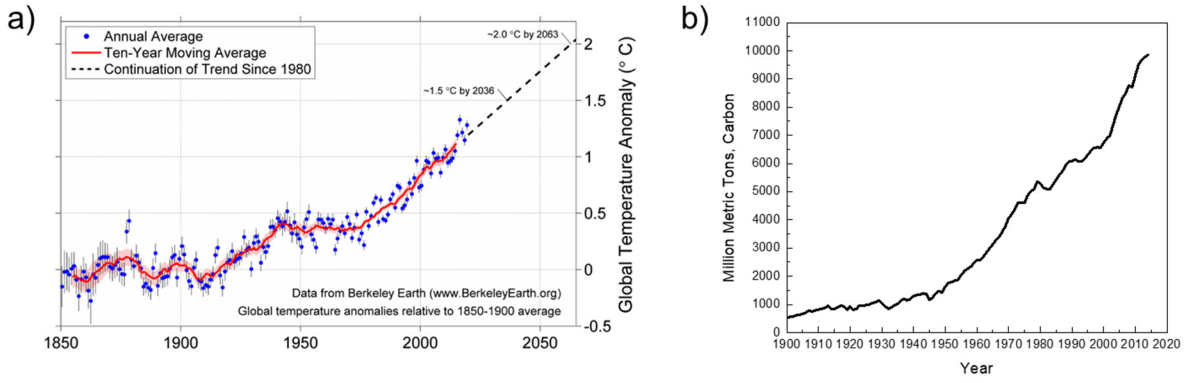

Figure 1.1 a) Global Temperature anomaly relative to 1850-1900 average, extrapolated to 2050.[1] b) Global CO_2 emissions, in millions of metric tons, from 1900-2014.[2]

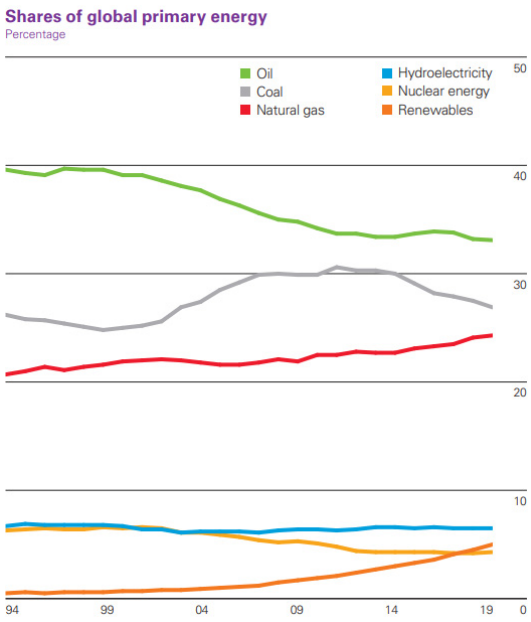

Figure 1.2. Global percentage of energy generated from specific sources.[3]

While Figure 1.2 illustrates an optimistic trend, currently, renewables still only make up a small percentage of the overall energy generation picture. In addition, this rapid implementation has ramifications on the grid. Figure 1.3 illustrates a typical energy demand curve over the course of a spring day in California. During midday, when renewables generate the most electricity, most people are away from home, so the net electricity demand goes down during this time. With more and more energy generation from renewables over the years, this “dip” in demand becomes more and more severe if the grid cannot accommodate the generated energy; when the electricity demand increases in the evenings, the grid must rapidly ramp up to meet the surge in energy demand. If the ramp-up is too steep, there would be service problems or outages. Although certain policy solutions have been proposed, such as selling the excess generated electricity to other service areas or states or to incentivize customers to use electricity during the day, these are not long-term, sustainable solutions; one of the ways forward to mitigate the strain on the grid is to implement safe and effective energy storage solutions.

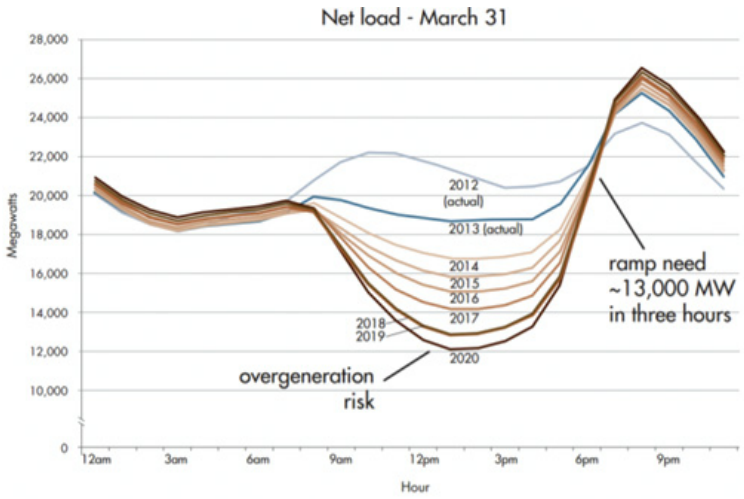

Figure 1.3. Energy generation (in megawatts) over a typical spring day in California. Data from CAISO 2016.[4]

1.2 Solid-State Batteries

Lithium-ion batteries have become one of our life's necessities, ubiquitous and playing essential roles in a multitude of applications ranging from consumer electronics and electric vehicles to aerospace products. They are widely used to store energy and provide power. As demand for electrification continues to grow, the adoption of Li-ion batteries in turn is growing exponentially. Thus, batteries that are safe and have high energy densities are exceedingly desired. Current Li-ion batteries that contain liquid electrolytes (LEs) have a significant risk of catching fire and even exploding due to the highly flammable organic solvents used in LEs. Replacing the liquid electrolytes with solid-state electrolytes (SSEs) will definitely enhance battery safety, as flammability and electrolyte leakage are not issues for SSEs. Additionally, SSEs potentially enable the use of the Li metal anode, which would greatly increase the energy density of batteries.[5] As a consequence, all-solid-state batteries (ASSBs) are regarded as one of the critical future technologies and have continued to attract enormous attention over recent years.

1.2.1 The Development of Solid-State Electrolytes

ASSB research began with seeking suitable materials that can serve as SEs, namely, materials with high ionic conductivity (σ_{Li+} > 0.1 mS/cm, commonly referred to as “superionic conductors”) but low electronic conductivity (σ_e < 10^{-7} mS/cm). Such materials include polymer-, oxide-, and sulfide-based electrolytes.[6] Sulfide-based electrolytes have been shown to have higher ionic conductivities than oxide- and polymer-based electrolytes due to their *bcc*-like anion framework, favorable for Li-ion diffusion.[7] Recently, sulfide-based superionic conductors have achieved ionic conductivities close to or higher than those of conventional LEs (~1 mS/cm). These include $Li_7P_3S_{11}$ (17 mS/cm), $Li_{10}GeP_2S_{12}$ (12 mS/cm), and $Li_{9.54}Si_{1.74}P_{1.44}S_{11.7}Cl_{0.3}$ (25 mS/cm).[8–10] A summary of representative Li-based SSEs and their ionic conductivities are summarized in Figure 1.4a.[11]

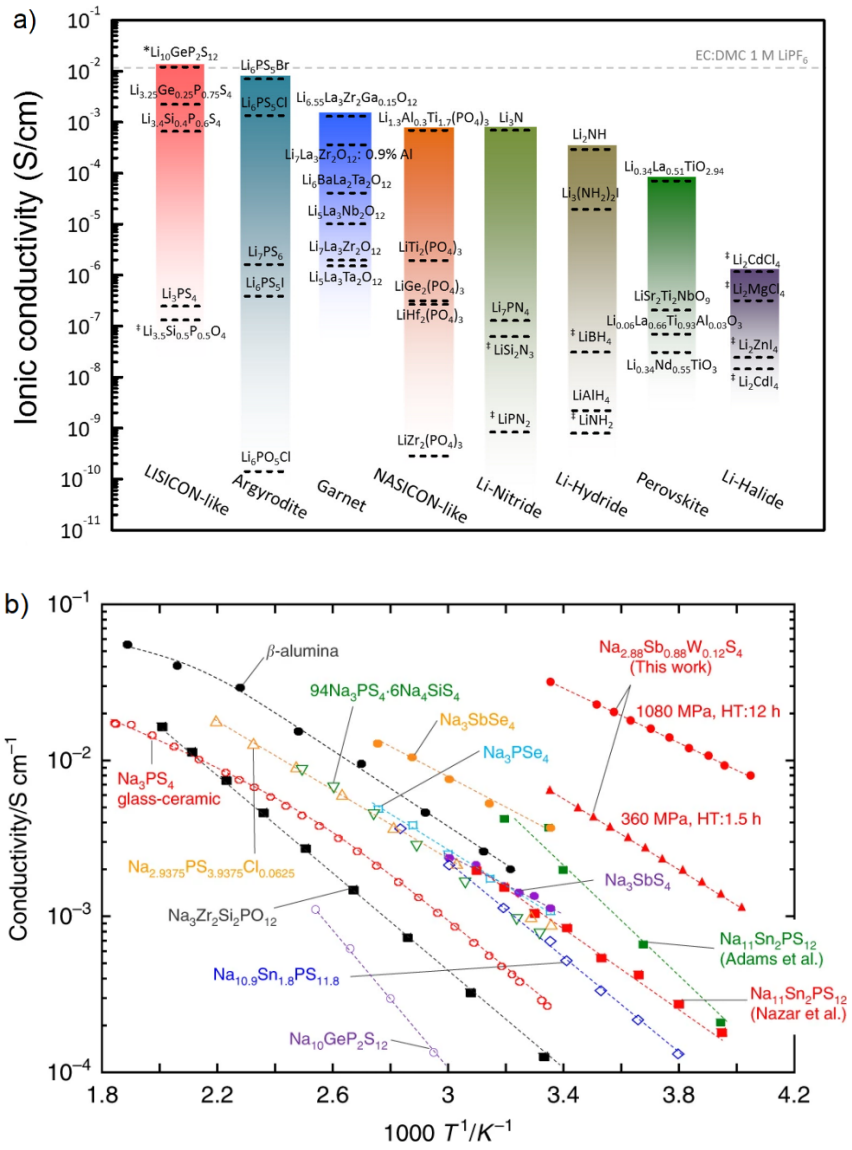

Figure 1.4. a) Room-temperature Li-ion conductivity of various Li SSE compounds[11] and b) Temperature-dependent Na-ion conductivity of Na SSE compounds.[12]

In parallel to the development of Li-ion conducting SSEs, Na-ion conducting SSEs have also seen much research interest, and many Na analogs to Li-ion conductors have been investigated in parallel. As such, a survey of the developed Na-based SSEs with their ionic conductivity values is shown in Figure 1.4b.[12] Interest in Na ASSBs is due to the fact that Na is a few magnitude more abundant than Li in the Earth's crust; not only are the environmental considerations lessened with obtaining Na, the cost of comparable, battery grade Na carbonate

(Na_2CO_3) is also orders of magnitude less than Li_2CO_3.[13] Since Na has a redox potential of -2.70 V compared to -3.04 V for Li (versus standard hydrogen electrode) and is heavier than Li, therefore, Na-based ASSBs will have lower energy density than a comparable Li system.[14] Thus, unlike for transportation and other high-power applications where absolute performance is paramount, Na-based ASSBs could occupy a market space where a higher performance-to-cost ratio is required, and grid storage is one such application.

1.2.2 Current ASSB Limitations

Regardless of whether an ASSB is Li- or Na-based, compared with conventional LE cells, ASSBs typically have higher polarization, lower capacity, and inferior power and cycling capabilities, which are attributed to severe interfacial problems, and these problems remain a primary bottleneck towards commercialization of ASSBs.[7] Thus, an ideal SSE has to possess high ionic conductivity, low electronic conductivity, and electrochemical, chemical, and mechanical compatibility with electrodes. Currently, no one electrolyte or class of electrolyte possesses all these qualities simultaneously, and as a result, any non-idealities can manifest as poor physical contact, the presence of grain boundaries, and chemical and electrochemical reactions, just to name a few, which can all contribute to increasing resistance at the cathode-electrolyte, electrolyte-electrolyte, and electrolyte-anode interfaces (diagrammed in Figure 1.5). This is partially due to the SSE properties; the sulfides, in particular, have a narrow electrochemical stability window, meaning they begin to undergo oxidative decomposition at relatively low voltages, such as $Li_{10}GeP_2S_{12}$ (LGPS) at 2.15 V and Li_3PS_4 (LPS) at 2.41 V vs. Li/Li^+.[15] Furthermore, due to the inherent chemical potential incompatibility of sulfide SEs with cathode/anode materials, spontaneous chemical reactions can occur. Such reactions will form a resistive solid electrolyte interphase (SEI) on the anode side or a cathode electrolyte interphase (CEI) on the cathode side (schematically shown in Figure 1.6) thereby hindering both Li-ion diffusion and charge transfer inside the ASSBs.[16,17]

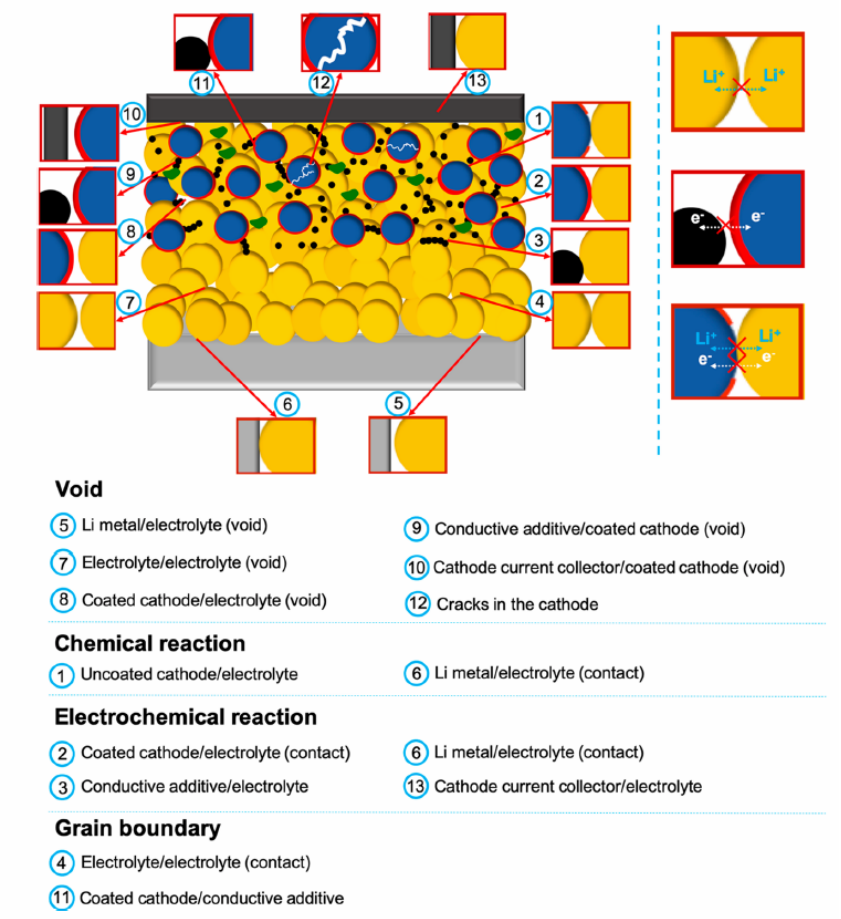

Figure 1.5. Schematic illustration of interfacial phenomena experienced in ASSBs.

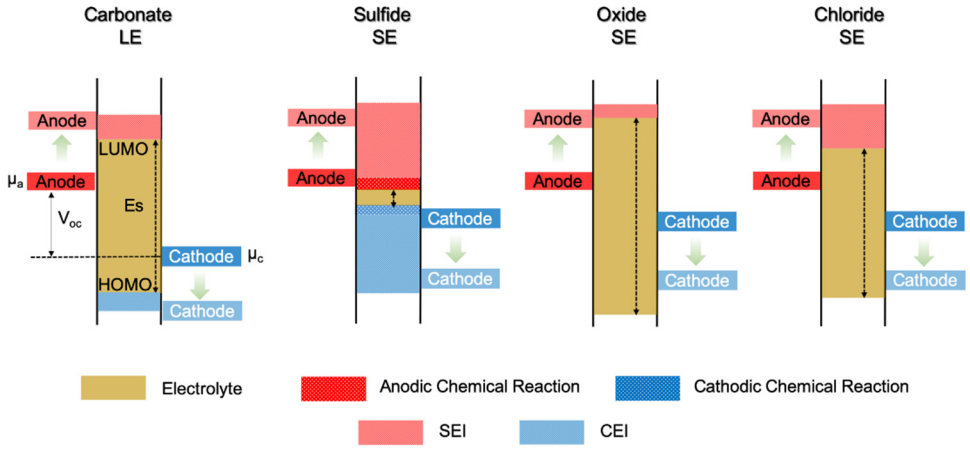

Figure 1.6. Schematic band diagrams of the HOMO and LUMO of different classes of electrolytes. If the μ_c is below the HOMO of the electrolytes, a CEI will form; an SEI will form if the μ_a is above the LUMO of the electrolytes.

Both computational and experimental methods are useful to explore the complex nature of the interfaces in ASSBs. Density functional theory (DFT) calculations and molecular dynamics simulations can provide microscopic viewpoints on thermodynamic stability, favorable kinetics, and atomic interactions at an interface. Although DFT calculations can predict the decomposition products, experimentally determining and confirming the presence of specific species and their distribution as well as their physical/chemical properties remains a challenging and rarely addressed problem. The physically buried nature of the interface along with the fact that most cathodes are composites, brings about much of the difficulty in isolating, probing, and identifying the chemical species. Such characterization requires proper experimental design and the use of various complementary techniques with a wide range of detection energy and spatial and temporal scales. Microscopy techniques, such as transmission electron microscopy (TEM), enables the visualization of the structure, morphology, and distribution at the interface. Spectroscopic techniques in turn provide the chemical state and electronic structure of the interfacial components. Electrochemical techniques can provide kinetic information on Li-ion diffusion and charge transfer at the interface. Identifying the chemical species and determining their distribution at the interface is very important because their chemical and physical properties directly govern the interfacial charge transfer resistance and ultimately, the electrochemical performance of ASSBs.

1.2.3 Interfaces in ASSBs

Unlike LEs, SSEs cannot flow or infiltrate into gaps and voids in an ASSB, resulting in poorer physical contact between particles. Since all of the components in ASSBs are solid, fabricating ASSBs requires stacking the cathode, electrolyte, and anode sequentially, resulting in numerous interfaces. As shown in Figure 1.5, 13 scenarios (that can all exist simultaneously in an ASSB) are listed, including the cathode/electrolyte, electrolyte/electrolyte, anode/electrolyte, current collector/electrolyte, and additive/electrolyte interfaces. These interfaces can be further

categorized into the following classes: voids, those formed via chemical reactions or electrochemical reactions, and grain boundaries. It is important to note that all of these interfacial phenomena will apply to both Li and Na ASSBs.

(1) **Voids:** although a high pressure (≥ 370 MPa) can be applied during cell fabrication, both the electrode and electrolyte are still far from the ideal closest-packing scenario; both remain quite porous. Such porosity usually ranges from 10%-40% depending on the pressure and mechanical properties of the electrolyte and electrode materials. Voids can also form during cell operation due to electrode pulverization caused by cracks forming in cathode particles and dendritic growth of Li metal. The presence of voids could i) hinder Li-ion diffusion and charge transfer, resulting in high contact resistance, ii) induce dendritic growth of Li metal, and iii) increase the cell volume which decreases the volumetric energy density of ASSBs.

(2) **Chemical reaction:** If an electrode and the solid electrolyte have a mismatch of chemical potential, spontaneous chemical reaction(s) may occur once these two materials are put in contact. Consequently, solid electrolyte interphases (SEI) and cathode electrolyte interphases (CEI) form at the anode and cathode side, respectively. A beneficial SEI/CEI should be a passivating layer that is and conductive to Li ions but not electrons, and extend the working voltage window of electrolytes, as shown in Figure 2. However, if the SEI/CEI is a mixed electronic and ionic conductor (MIEC), the SEI/CEI will continue to grow, deteriorating the performance of ASSBs. Protecting the cathode/anode with relatively inert materials has proven to be an effective way to mitigate chemical reactions.

(3) **Electrochemical reaction:** most SEs have a narrow electrochemical stability window and cannot operate at the full voltage range of the cathode and anode materials. SEs can be oxidized at high voltages or reduced at low voltages if they have sufficient contact with electronically conductive materials, which can include the cathode/anode materials, current collector, and/or conductive additives. Note that oxide- and chloride-based SEs have a wider stability window than sulfide-based SEs (Figure 2); they are stable at high voltages but not stable

at low voltages. The electrochemically decomposed electrolytes will also contribute to forming the SEI/CEI and increase the charge transfer resistance. Coupling electrode materials with matching operating voltage windows and slowing down reaction kinetics are beneficial as they reduce the electrochemical reactivity of SEs.

(4) **Grain boundaries:** a grain boundary is present if two particles are in contact and if they have different electrochemical potentials. The Li ions will then transfer from one particle to another particle, leaving a Li-deficient space-charge layer at the interface, which greatly suppresses ionic conduction at the interface.

Although all of the interfaces can exist simultaneously and degrade cell performance (and are thus all important to investigate and understand), among the many scenarios presented, the focus of this dissertation will be on the chemical reactivity and electrochemical reactivity between the SSE toward finding and engineering compatible battery chemistries.

1.2.3.1 The Anode/Solid-Electrolyte Interface

One of the reasons behind the growing interest in SEs is the potential application of the high-capacity Li or Na metallic anode, which would dramatically increase the energy density of the ASSB. It is well-known that these metals are very electropositive and reactive, which means it will spontaneously react with most SSEs at room temperature to form a SEI. The chemical, mechanical, and electronic properties of this interphase are crucial for determining the long-term electrochemical behavior and viability of ASSBs.

Depending on the reactivity of the SSE with the metallic anode and the properties of the SEI, the interface can be categorized into three types (Figure 1.7): 1) A chemically stable interface with no SEI layer, allowing efficient Li-ion transfer from Li metal to SE (Figure 1.7a). 2) An ionically conductive but electronically-insulating interphase, where at least one of the SEI components is ionically conductive and is stable once formed (Figure 1.7b), 3) A mixed ionic- and electronically conducting (MIEC) interface where both ionically and electronically conductive materials are

present. The MIEC interface is not stable and will continue to grow during cycling, which means the interfacial resistance will continue to increase (Figure 1.7c).

In this dissertation, for the anode/solid electrolyte interface, the interface between the Na metal anode and the electrolyte Na_3SbS_4 (σ_{RT}: 1-3 mS/cm)[18,19] was investigated to determine which kind of aforementioned category the interface falls under. This electrolyte, while having high ionic conductivity, was not demonstrated to have long-term cycling in a battery application in the literature. Thus, understanding the interfacial phenomena through computational, electrochemical, and spectroscopic tools, was conducted in order to inform better design strategies for a stable anode interface in Na ASSBs.

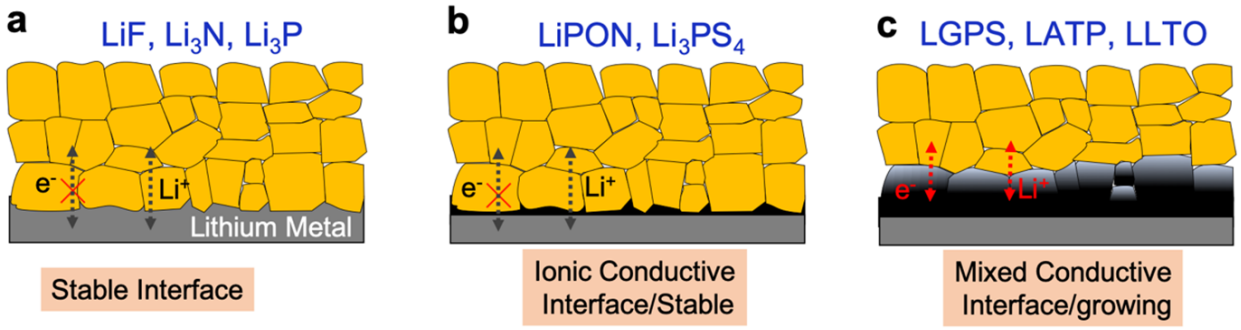

Figure 1.7. The Types of Anode Interfaces: (a) Interfacial products that are thermodynamically stable with Li metal, (b) SEs which form a stable, ionically conductive interface, and (c) SEs which form a mixed ionically-and electronically-conductive interface, which will grow continuously, eventually resulting in cell shorting

1.2.3.2 The Cathode/Solid-Electrolyte Interface

As shown in Figures 1.5 and 1.6, a chemical reaction will also arise from a chemical potential difference between cathode materials and SSEs. This difference will be more pronounced when electrochemical diffusion of Li ions occurs at the same time; in other words, chemical reactions between cathode materials and SEs will become exacerbated during electrochemical cycling, especially in the charged state.

Understanding the chemical and physical properties of the cathode/SSE interface is necessary because just like the anode interface, it can directly affect ASSB performance. Multi-scale characterization has been applied to identify interfacial products, their spatial distribution, their ionic/electronic nature, and their effect on cell performance. For instance, TEM and electron diffraction could be used to observe degradation (e.g. long-range Co distribution) at the bare cathode/SSE interface,[10] and surface-sensitive techniques such as XPS are again useful to identify interfacial products. Whether the interface that results from chemical reactions is passivating or not again depends on the ionic and electronic conductivity of the CEI products. Just as with the anode interface, any electronically-conductive components will result in a continuously growing interface that will hinder battery performance.

1.2.3.2.1 Protective coating layer

Applying a conformal, chemically inert coating has proven to be effective at both preventing chemical reactions between cathode materials and SSEs and lowering the interfacial resistance. For example, the addition of a $LiNbO_3$ layer (2 wt% Li-ion conductive and amorphous) on NCA drastically improves the CE and discharge capacity, reflected in not only lower cathodic charge transfer impedance,[51] but also in stabilizing impedance values over long durations. A schematic of the beneficial effects of a coating layer on cathode particles on minimizing unwanted reactions is shown in Figure 1.8. It is important to note that applying a coating will generate two new interfaces: (i) cathode-coating layer and (ii) SE-coating layer.

A suitable coating layer for ASSBs must have the following properties:

(1) **Phase stability.** The phase stability of coating materials is measured by the E_{hull} (in eV/atom); a lower E_{hull} means the coating is more thermodynamically stable.

(2) **Chemical compatibility.** Typically, a good coating will have a negligible or zero decomposition energy between the cathode/coating and the SE/coating, and thus many coatings are oxide-based if the cathode is also an oxide.

(3) **Electrochemical stability.** A suitable coating material should be electrochemically stable within the operating voltage range of the cathodes. Thus, the transition metal redox band should be well-separated from the oxygen 2p band of the coating layer to avoid redox activity.

(4) **Conductivity.** An ionically-conductive coating layer enables the transport of Li ions across the coating layer which improves the rate performance of ASSBs. However,highly electronically conductive coatings promote electrochemical decomposition of SEs (especially with sulfides that decompose at very low voltages) which results in increased cathode impedance. Thus, large band gap materials with high Li-ion conductivity are necessary to achieve better performance. However, a balance must be struck as poor electronic conductivity of the coating would also block electronic pathways, hindering the rate performance of ASSBs.[100]

(5) **Mechanical property.** Cathode volume changes will induce strain on the coating layer. Similar to the mechanical property of the electrolyte, the elasticity of the coating layer is important in order to accommodate the strain, i.e. plastic deformation without cracking. Usually a volume change of 10% and 30% (of the cathode) produces 1% and 10% strain, respectively, within the coating layer. LNO, the most common coating, is known for its high stiffness and is expected to form cracks rather than deform plastically.[105-107] Any cracks in the coating will make the cathode come into direct contact with SE, which will facilitate

both chemical and electrochemical decomposition of the SE, degrading the battery performance. Amorphous coatings are beneficial as they can more easily deform elastically during the charge-discharge process.

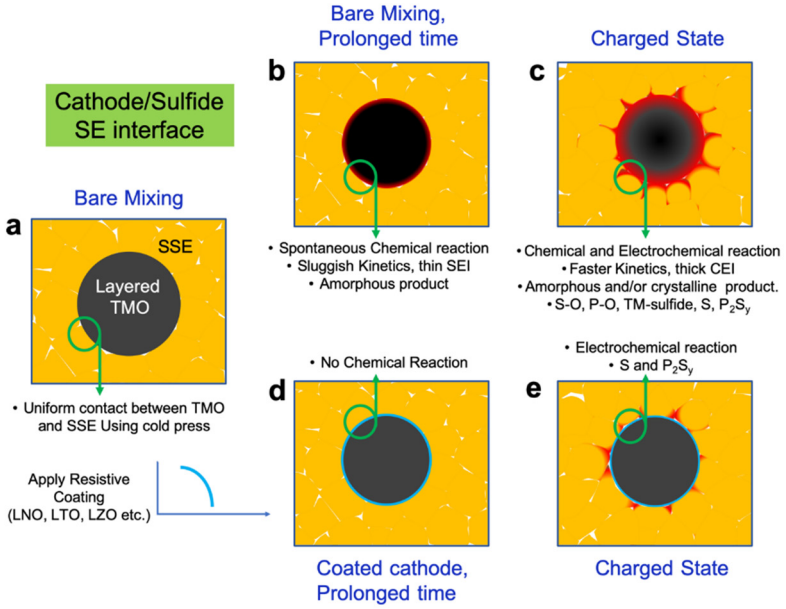

Figure 1.8. a) Schematic of a bare sulfide SSE mixed with a layered TM oxide cathode, where (b) a spontaneous chemical reaction occurs and (c) will be exacerbated in the charged state. (d) A coating layer is applied on the cathode, but (e) an interface still forms at the charged state from electrochemical decomposition.

In this dissertation, for the cathode/solid electrolyte interface, the research focus is placed on how to characterize such interfaces and how to engineer materials in order to stabilize these interfaces and prevent unwanted reactions to have longer-cycle-life ASSBs. With regards to sodium-based ASSBs, inspired by recent reports on a halide-based solid-state electrolyte, a new, stable, chloride-based sodium ion conductor was synthesized and evaluated experimentally and computationally in the context of its diffusion mechanism, its stability, its electrochemical window, and its performance with the oxide cathode $NaCrO_2$. In terms of the protective cathode coating, which are usually solution-processed, a dry-processed, lithium-borate-based coating on the oxide $LiNi_{0.8}Co_{0.1}Mn_{0.1}O_2$ (NCM811) cathode was investigated via electrochemical methods and TEM to evaluate its performance and properties against conventionally-processed coatings.

1.3 Fuel Cells

Solid-state batteries have now been discussed as a promising way to mitigate the strain on the grid introduced by the continued adoption of renewable energy generation. With regards to Figure 1.3, however, the other source that is seeing a rise in adoption is natural gas. While using natural gas still introduces emissions, the amount of CO_2, nitrogen oxides, sulfur dioxide, and particulates are many times lower than burning oil and coal[20], but extraction of natural gas (e.g. fracking) has potential long-term environmental considerations that still need to be addressed.[21] Fuel cells are another pathway to further advance cleaner energy generation, since they are energy conversion devices that convert chemical energy in fuels to electrical energy via redox reactions, which is much more efficient than combustion methods. Thus, they are electrochemical devices and not subject to thermodynamic limits such as the Carnot cycle; fuel cells can have fuel-to-electricity conversion rates around of 70%[21,22]. It is important to note that while fuel cells primarily operate with hydrogen (H_2) fuel and it has been reported that they output little to no emissions during operation, currently, 95% of the world's H_2 is produced via steam reforming of natural gas or fossil fuels.[23]

Many different kinds of fuel cells are been developed over the years, such as low temperature (60-100°C; Polymer Electrolyte Membrane) to temperatures up to 1000°C (Solid Oxide Fuel Cell)[24]. A comparison of different kinds of fuel cells are shown in Table 1.1.

Table 1.1 Comparison of various Fuel Cell technologies.[24]

Fuel Cell Type	Operating Temperature (°C)	Power (kW)	Efficiency (%)	Application
PEM (Polymer Electrolyte Membrane)	60-110	0.01-250	40-55	Portable, mobile, low-power generation
AFC (Alkaline fuel cell)	70-130	0.1-50	50-70	Portable, Mobile
PAFC (Phosphoric Acid Fuel Cell)	175-210	50-1000	40-45	Medium to large-scale power generation, combined heat and power (CHP)
MCFC (Molten Carbonate Fuel Cell)	550-650	200-100,000	50-60	Large-scale power generation, CHP
SOFC (Solid Oxide Fuel Cell)	500-1000	0.5-2000	40-72	Vehicle auxiliary power units, medium to large scale power generation, off-grid power, CHP.
DMFC (Direct Methanol Fuel Cell)	70-130	0.001-100	40	Portable, mobile

When considering grid storage and large-scale power-generation applications, solid oxide fuel cells (SOFCs) are of high research interest as they have many advantages compared to the other technologies – they contain a durable solid-state electrolyte that can withstand high temperatures, can to operate at very high efficiencies as shown in Table 1.1, do not require water management, and are a flexible platform that can accommodate a variety of fuels[24–26]. Figure 1.9 shows a Ragone plot (specific energy versus specific power) that compares various energy devices, which shows the high power and high energy properties of the SOFC due to their high efficiencies.

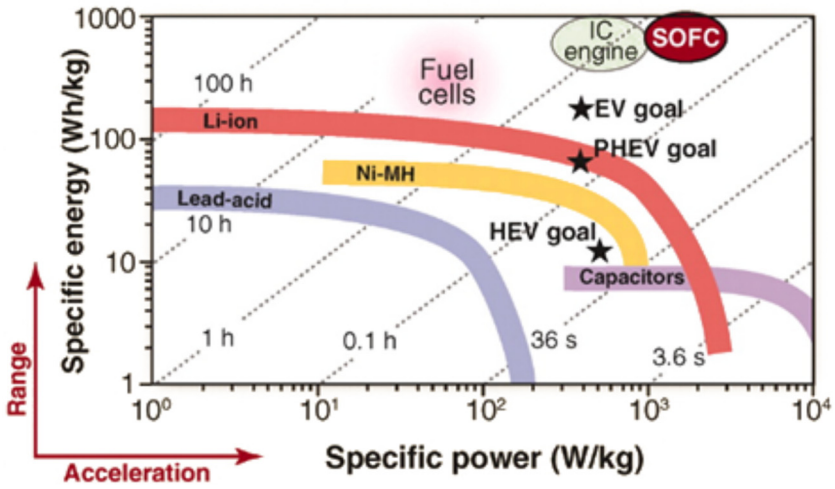

Figure 1.9. Ragone plot (specific energy versus specific power) for various battery chemistries, capacitors and the internal combustion engine as they compare to SOFCs.[27]

1.3.1 Conventional SOFCs

The basic operating principle of a fuel cell is that the reduction of oxygen (air) occurs at the porous cathode to form oxygen ions, and driven by the difference in oxygen partial pressure (high pO_2 at the cathode and low pO_2 at the anode), the oxygen ions will diffuse through the dense electrolyte to the porous anode, where the oxidation of H_2 will occur, generating electrical work in the process.[28] The schematic and working mechanism of a SOFC and a typical SEM micrograph is shown in Figure 1.10. It is important to note that the electrodes must be porous to enable oxygen diffusion at the cathode side and also gas diffusion and the extraction of byproducts (H_2O) and unused fuel at the anode side.

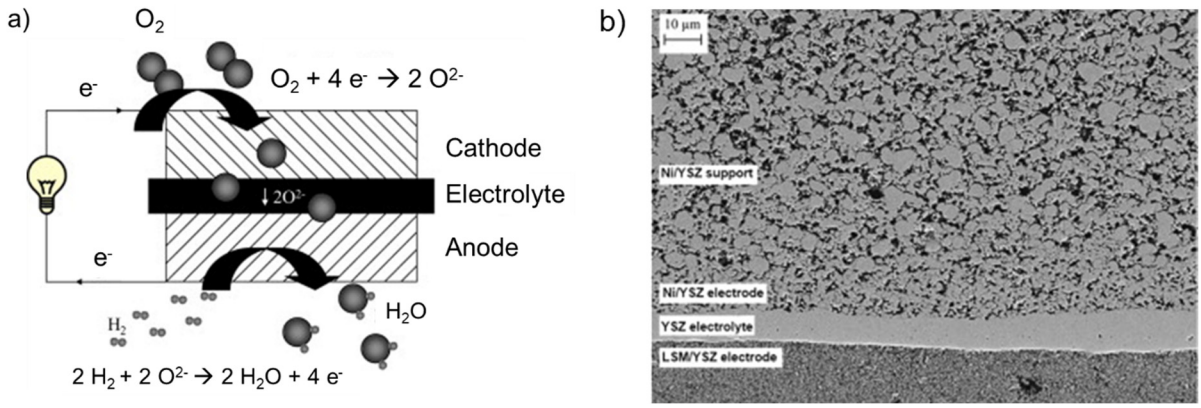

Figure 1.10. a) Schematic of the operation of a fuel cell depicting the redox reactions and b) a cross-sectional SEM image of the layers in a conventional anode-supported SOFC device.[28,29]

The micrograph in Figure 1.10b also labels the typical materials used in the conventional SOFC. For the cathode, perovskite-based oxides that are mixed electronic and ionic conductors (MIECs) are typically employed as they have high thermal stability (up to around 800°C) and provide catalytic activity to enhance the reduction of O_2; examples include Lanthanum Strontium Manganites ($La_xSr_{1-x}MnO_{3\pm\delta}$) and Lanthanum Strontium Cobalt Ferrites ($La_xSr_{1-x}Co_yFe_{1-y}MnO_{3\pm\delta}$)[28]. The electrolyte, which needs to be dense and pinhole-free to prevent short circuiting, needs to have high oxygen conductivity and also high stability; to this end, yttria-stabilized zirconia (YSZ) is widely used.[22] It is important to note that other oxides that conduct O^{2-} such as bismuth oxides become electronically conductive at temperatures around 800°C, which would also cause short circuits thus rendering the fuel cell inoperable.[28] Lastly, for the anode, which must have catalytic activity for fuel oxidation and be a MIEC. To this end, a composite anode, typically nickel and YSZ (Ni-YSZ), is used to satisfy the requirements.[28]

1.3.1.1 Limitations of the Conventional SOFCs

A typical SOFC operates at temperatures from 800-1000°C in order for the electrolyte to have sufficient O^{2-} conduction. However, such temperatures limit the materials that can be used (such as the perovskite cathodes or other electrolytes previously mentioned), as high temperatures can induce thermal degradation or induce electronic conduction in the electrolyte, which will inevitably shorten the life of the cell. In addition to these durability concerns and material limits, maintaining and sustaining the operating temperature will also introduce high energy costs. Thus, these are the main obstacles toward SOFC commercialization and widespread adoption.

If the operating temperature can be reduced to intermediate temperatures such as 600°C, the mentioned cell and device lifetime, material costs, and thermal management costs will all reduce. To this end, the following strategies can be implemented: either the continued development of new materials that have a much higher O^{2-} conductivity, or a drastic reduction in the thickness of the SOFC; the development of μ-SOFCs, or Thin-Film SOFCs (TF-SOFCs), where the SOFC thickness decreases from ~100s of μm (as shown in Figure 1.10b) to just a few μm, is thus highly desired.

1.3.2. Development of Thin-Film SOFCs

Compared with the bulk SOFCs, by virtue of having a reduced thickness of the device, the overall impedance will drop according to the following equation:

$$R = \frac{\rho L}{A}$$

Where ρ is the resistivity of the material, L is its thickness, and A is the cross-sectional area. Thus, a decreased device thickness will provide all of the aforementioned benefits of cost reduction, lifetime increase, and a wider selection of materials.

To fabricate thin-film SOFCs, various thin-film processing techniques have been employed to deposit high-quality films (porous films for the electrodes and dense films for the electrolyte).

Among them include chemical vapor deposition (CVD) methods such as atomic layer deposition (ALD),[30] pulsed laser deposition (PLD),[31] solution-based methods,[32] and physical vapor deposition (PVD) methods.[33,34] While TF-SOFCs have successfully been fabricated using these methods, ALD, PLD, and solution-based methods have drawbacks such as: high maintenance costs, a limited deposition area, low deposition rates (due to the atomic layer-by-layer deposition method),[28] a complicated experimental setup,[35] or that a single fabrication processes cannot make every component of the TF-SOFC, hindering the practicality and manufacturability.

PVD methods such as sputtering are highly desired compared to the chemical methods; sputtering, where a target material is bombarded with ionized inert gas (e.g. Ar^+) and ejected, where it ultimately gets deposited as a film on a substrate, is one such PVD method that has seen growing interest. Sputtering has been used in industrial applications such as the semiconductor industry and based on the target material, target size, and chamber size, the deposition process can be readily tuned to fabricate a variety of films and larger-area devices.

In this thesis, taking the common SOFC materials Ni-YSZ, YSZ, and LSCF as the anode, electrolyte, and cathode, respectively, sputtering methods were investigated and developed to fabricate the different layers of the TF-SOFC. This way, a single process can be used to minimize contamination, and the fabrication process can be vastly simplified and potentially adapted to a wide range of ceramic materials. The all-sputtered cells were then evaluated for their performance, and the nanostructured and porous LSCF-YSZ composite cathode exhibited superior performance compared to its LSCF counterpart. We highlight the development of this sputtering platform that can be adapted and tuned to various SOFC materials and desired deposition areas.

Chapter 1, in part, is a reprint of the material “Interfaces and Interphases in All-Solid-State Batteries” as it appears in Chemical Reviews. Banerjee, A.*, Wang, X.*, Fang, C., Wu, E. A., and Meng, Y. S. 2020, 120, 6878-6933. The dissertation author was one of the authors of this paper and all authors contributed.

Chapter 2. Investigating the Sodium Metal/Na_3SbS_4 Interface

In this work, we investigated the interface between the sodium anode and the sulfide based solid electrolytes Na_3SbS_4 (NAS), Na_3PS_4 (NPS), and Cl-doped NPS (NPSC) in all-solid-state-batteries (ASSB). Even though these electrolytes have demonstrated high ionic conductivities in the range of 1 mS cm^{-1} at ambient temperatures, sulfide sold-state electrolytes (SSEs) are known to be unstable with Na metal, though the exact reaction mechanism and kinetics of the reaction remain unclear. We demonstrate that the primary cause of capacity fade and cell failure is a chemical reaction, spurred on by electrochemical cycling that takes place at the interface between the Na anode and the SSEs. To investigate the properties of the Na-solid electrolyte interphase (SSEI) and its effect on cell performance, the SSEI was predicted computationally to be composed of Na_2S and Na_3Sb for NAS and identified experimentally via X-ray photoelectron spectroscopy (XPS). These two compounds give the SSEI mixed ionic- and electronic-conducting properties, which promotes continued SSEI growth, which increases the cell impedance at the expense of cell performance and cycle life. The SSEI for NPS was similarly found to be comprised of Na_2S and Na_3P, but XPS analysis of Cl-doped NPS (NPSC) showed the presence of an additional compound at the SSEI, NaCl, which was found to mitigate the decomposition of NPS. The methodologies presented in this work can be used to predict and optimize the electrochemical behavior of an all-solid-state cell. Such joint computational and experimental efforts can inform strategies for engineering a stable electrolyte and SSEI to avoid such reactions. Through this work we call for more emphasis on SSE compatibility with both anodes and cathodes, essential for improving the electrochemical properties, longevity, and practicality of Na-based ASSBs.

2.1 Introduction

Liquid electrolytes are the dominant technology used in lithium-ion (Li-ion) batteries as they have suitable properties such as high ionic conductivity, intimate contact with electrodes, and allow the formation of a stable SEI that enables long-term battery cycling. However, liquid electrolytes typically contain toxic, flammable, and corrosive materials[36,37]. These hazards become more pronounced when pertaining to large-scale energy storage applications. To ameliorate this issue, solid-state electrolytes (SSEs) are gaining traction as they do not contain such flammable components, thus avoiding the possibility of catastrophic failure. A practical SSE would make batteries lower-maintenance and enable even longer cycling life. Furthermore, the use of metallic Li or Na as the anode, which would dramatically increase the energy density of the battery, is not achievable with current conventional liquid electrolyte cells. For these reasons, research interest in SSEs has been steadily growing[38].

However, SSEs also have their drawbacks, such as having an ionic conductivity typically an order of magnitude lower than liquid electrolytes and inherently poorer contact with neighboring electrodes[9,39]. Much of the previous effort in SSE research was directed toward increasing the ionic conductivity to be comparable with liquid electrolytes, with a now oft-stated benchmark value of at least 1 mS cm^{-1} at room temperature[7]. The recent development of $Li_{10}GeP_2S_{12}$, a solid electrolyte that has a reported room temperature conductivity of 12 mS cm^{-1}, has driven further interest in SSEs as this number is comparable to or even exceeds that of commonly used liquid electrolytes[9]. Recently, many new SSEs with high ionic conductivities have been developed and reported[11].

In parallel to the development of Li-ion-conducting SSEs is the rise in interest in Na-ion conductors for all-solid-state batteries. To that end, many Na analogs to Li-ion conducting SSEs have been explored both computationally and experimentally[40–42]. All-solid-state Na ion batteries have the potential to be a lower-cost alternative; Na is orders of magnitude more abundant than

Li in the Earth's crust which makes the cost of Na around 20-30 times less than Li[39,40]. The precursors to synthesize Na-ion conducting solid electrolytes are readily available Na salts or compounds. Furthermore, the electrochemical behavior of Na is similar to that of Li. Although Na has a redox potential of -2.70 V compared to -3.04 V for Li (versus standard hydrogen electrode), the significant cost reduction for raw Na metal suggests that Na batteries can still occupy a market space where cost is a more important consideration than having the absolute highest energy density[39,40]. One such application is the aforementioned large- or grid-scale energy storage[43,44].

An ideal Na solid-state electrolyte must have several properties, among which are: an ionic conductivity of 1 mS cm^{-1} or greater at room temperature, intimate contact with solid electrodes, the ability to operate over a wide electrochemical window, and have good stability against elemental Na[38]. However, no single electrolyte material or class of materials currently possesses every one of these characteristics[45]. As an example, much research effort has been put into SSEs such as β-alumina and NASICON, but these oxides only exhibit good conductivity at elevated temperatures[46–50].

Chalcogenides, or S- and Se-based compounds, have been shown to have favorable properties for use as a solid-state electrolyte[48]. Although they have their own issues such as air- and moisture-sensitivity, they have potentially higher ionic conductivities[47,51–53] and a lower Young's modulus compared to oxide materials[51,54]. A more elastic solid electrolyte would be more able to accommodate volume changes associated with the intercalation and de-intercalation of Li^+ or Na^+ ions without the onset of cracks or mechanical failure. Another benefit of sulfides is that they do not need energy-intensive processing steps such as high-temperature sintering to obtain a high ionic conductivity value; Oxides usually require this to overcome a larger grain boundary impedance, but for chalcogenides, room-temperature cold-pressing is sufficient[18,19]. Various Na solid electrolytes have been studied, among them Na_3PS_4 and Na_3PSe_4[42,53,55–59]. It was postulated that selenides have greater conductivity than sulfides as a larger unit cell would subsequently have more channels for Na-ion conduction. For example, Na_3PSe_4 has a room temperature

conductivity of 1.16 mS cm^{-1} compared to 0.2 mS cm^{-1} for Na_3PS_4. Since the SbS_4^{3-} ion is similar in size to the PSe_4^{3-} ion, NAS could also have a favorable structure to be used as an SSE, and indeed, NAS has been reported to have an ionic conductivity in the range of 1 mS cm^{-1} [18,19]. Along with structural modification, aliovalent doping has also been proven to increase ionic conductivities on sulfide-based glasses and glass-ceramics[18,53,60–63]. Our previous work highlighted Cl-doped tetragonal Na_3PS_4 (NPSC) which demonstrated an ionic conductivity exceeding 1 mS cm^{-1} [55].

Although several sulfide SSEs have demonstrated high ionic conductivity, they also have the persistent problem of instability when put in contact with Na metal[19,64]. In this work, phase pure NAS, NPS, and NPSC were all successfully synthesized, their electrochemical properties were evaluated, and the species at the SSEI were investigated via computation, electrochemical experiments, and material characterization techniques. The aim in this investigation is to highlight degradation mechanisms such as unwanted reactions between the electrolyte and electrodes in an ASSB. We emphasize that although ionic conductivity of an electrolyte is important, elucidating the failure mechanisms of all-solid-state full cells can provide critical insights for further screening of SSEs, subsequent evaluation of compatible ASSB chemistries, and engineering of their electrochemical interfaces.

2.2 Methods

Due to the sensitivity of the precursor compounds and the SSEs to water and air, all synthesis and electrochemical testing steps took place in an Ar-filled glovebox (MBraun MB 200B, H_2O < 0.5 ppm, O_2 < 1.0 ppm) unless otherwise specified.

2.2.1 Synthesis of NAS, NPS, and NPSC

Solid-State synthesis of NAS was achieved by mixing Na_2S (99%, Sigma Aldrich), Sb powder (99.999%, Alfa Aesar), and S (99.998%, Sigma Aldrich) in a mortar and pestle for 30 minutes in the ratio outlined by Eq. 1.

$$3\ Na_2S + 2\ Sb + 5\ S \rightarrow 2\ Na_3SbS_4 \quad (1)$$

The mixture was pressed into a 13mm diameter pellet (Carver) at 370MPa, broken up into small pieces, loaded into a quartz tube and capped with a rubber septum. The edges of the septum were wrapped with paraffin film (Parafilm® “M”). The tube was brought outside of the glove box, connected to vacuum, flame-sealed, and heat-treated in a box furnace. The temperature was ramped to 550°C over one and a half hours, kept at 550°C for 24 hours, and subsequently naturally cooled down to room temperature. The quartz tube was brought back into the glovebox where the material was extracted and placed into a ball mill jar with eleven 10mm ZrO_2 grinding balls. The jar was sealed tightly in the glovebox to prevent ambient oxygen and water to be introduced upon removal of the jar from the glovebox. The material was ball-milled at 370rpm over a duration of 20 hours with 15-minute grinding and 15-minute rest intervals using a Retsch PM 100 Planetary Ball Mill. The jar was brought back into the glovebox and the material was extracted for further testing.

Pure tetragonal Na_3PS_4 (t-Na_3PS_4) was synthesized via solid-state reaction following the methods outlined in a previous work[55]. The material was synthesized from Na_2S (99%, Sigma Aldrich and P_2S_5 (99%, Sigma Aldrich). The precursors were ground with an agate mortar and pestle in a molar ratio of 75:25, respectively. To introduce the chloride dopant, NaCl (99.99%, Alfa Aesar) was mixed into the previous precursors according to Eq. 2:

$$(1.5 - x)Na_2S + 0.5P_2S_5 + xNaCl \rightarrow Na_{3-x}PS_{4-x}Cl_x. \quad (2)$$

The resulting mixture was then flame-sealed under vacuum in a quartz tube and heat-treated in a box furnace. The temperature was ramped to 850°C over 6 hours and then immediately quenched in water containing dry ice. Subsequently, the sample was re-introduced

into the glovebox, ground in a mortar and pestle, flame-sealed, and heat-treated again at 420 °C for 3 hours to stabilize the tetragonal phase.

2.2.2 X-Ray Diffraction - NAS

A 0.5mm-diameter Boron-rich capillary glass tube (Charles Supper) was loaded with a few milligrams of the Na_3SbS_4 powder after ball-milling. The tube opening was capped with clay and wrapped in paraffin film before being brought outside of the glovebox where it was flame-sealed using a handheld butane torch.

The sample was fixed in the Bragg-Brentano theta-theta configuration and the Debye-Scherrer method was used. The samples were measured on a Bruker Kappa goniometer equipped with a Bruker Vantec 500 detector. XRD data was collected using Cu Kα radiation at 45kV and 50mA, over a 2θ range of 5-90° with a step size of 0.01°. Rietveld refinement was conducted using the FullProf software suite[65].

2.2.3 Electrochemical Impedance Spectroscopy (EIS) - NAS

The ball-milled NAS powder was pressed into a 13mm polyether ether ketone (PEEK) die using two titanium plungers at a pressure of 370 MPa. The thickness of the pellet was recorded. Carbon powder was applied to both sides of the die to serve as blocking electrodes and to improve contact with the titanium current collectors. The carbon was pressed onto the NAS pellet at 370 MPa. The test cell was then secured into a cell holder and connected to a Solartron 1260 impedance analyzer. Impedance measurements were taken with an applied AC potential of 50mV over a frequency range of 1MHz to 1Hz. The Nyquist plot was fit to an equivalent circuit model similar to a Randles circuit with the exception of using constant phase elements (CPEs) instead of capacitors to account for any non-ideal capacitive behavior such as a non-uniform electrode surface[66]. Temperature-dependent impedance measurements were collected by heating the cell inside a box furnace inside the glovebox. The temperature was raised from 25°C to 95°C in 10°C

increments. For every increment, the heating rate was 1°C min^{-1} and the target temperature was held for an hour to allow for the temperature to stabilize before the EIS measurement was taken. The activation energy (E_a) for Na ion diffusion was calculated from the slope of the resulting Arrhenius plot.

2.2.4 Construction of Symmetric Cells for NAS, NPS, NPSC

For the symmetric cell construction, 250mg of the ball-milled NAS powder was pressed into a 13mm polyether ether ketone (PEEK) die using two titanium plungers at a pressure of 370 MPa. Na metal was pressed onto both titanium plungers to form a thin disc on the plunger surfaces. Excess Na metal and any visible surface oxidation was scraped away from the plunger. The plungers were placed into the PEEK die and pressed at 37MPa. The pressure was released immediately, and the cell was subsequently fastened into the holder. EIS was measured every 2 hours for a duration of 50 hours using a frequency range of 1MHz to 0.01Hz and an applied potential of 50mV.

For the NPS and NPSC symmetric cells, the same procedure was applied to construct the symmetric cells. Once constructed, a 50 μA galvanic square-wave waves applied for 10 minutes and then a reverse current was applied for the same duration to strip and plate Na metal, respectively. The voltage of the symmetric cell was measured and the area-specific resistance (ASR) was calculated by Ohm's law.

2.2.5 Construction of Full Cells – NAS, NPS, NPSC

The procedure to construct electrochemical full cells was the same regardless of the SSE used. Electrochemical cells were constructed using a Na metallic anode, solid electrolyte, and a composite cathode, consisting of the electrolyte mixed with ball-milled TiS_2 in a 1:2 ratio. The composite cathode was newly mixed each time before making a cell. 250mg of the SSE powder was pressed at 370 MPa for 5 minutes in a 13mm PEEK die. Roughly 10mg of the composite

cathode was measured, recorded, and placed onto the electrolyte on the tall titanium plunger side. The cathode was pressed at 370MPa for 5 minutes to ensure complete coverage. Na metal was pressed onto the opposite side, or the small titanium plunger in a similar manner as described for the symmetric cell. After pressing at 37MPa, the cell was fastened into a holder.

All cells were galvanostatically cycled from 1.2V to 2.4V using a Digatron cycler at a rate of C/10. Cycling was conducted at room temperature within the MBraun Ar-filled glovebox.

2.2.6 *In situ* impedance – NAS

A cell containing Na, 250mg of NAS, and 10mg of the TiS_2:NAS composite cathode was constructed as previously described. The cell was connected to the Solartron 1260 Impedance Analyzer and held at rest (open circuit voltage measurement) for 30 minutes. The cell was galvanostatically cycled from 1.2V to 2.4V at a rate of C/5 for 5 cycles. Every time the cell reached 1.2 or 2.4V, an EIS measurement was taken using a frequency range of 2MHz to 0.01Hz and an applied potential of 50mV.

2.2.7 Cyclic Voltammogram (CV) - NAS

An electrochemical cell was constructed as previously described, except instead of a NAS:TiS_2 composite cathode, a NAS:carbon 1:1 mixture (weight ratio) was used. The cell was connected to the Solartron 1260 impedance analyzer, where CV was conducted for 20 cycles between 1.2 to 2.4V at a scan rate of 5 mV sec^{-1}.

2.2.8 Electrochemical Stability Analysis – NAS

The electrochemical stability of NAS in contact with the electrodes is estimated using the Na grand potential approach, as detailed in our recent work[52]. In this approach, the solid electrolyte-electrode interface is modeled as an open system with respect to Na, and the relevant thermodynamic potential is the grand potential, given as $\Phi \approx E - \mu_{Na} N_{Na}$. E, N_{Na} and μ_{Na} are total energy from density functional theory calculations and the number of Na atoms in the open system

and Na chemical potential, respectively. Noted that the chemical potential of Na is related to the voltage vs Na/Na^+ (V) via the following relation, with $V = -(\mu_{Na} - \mu_{Na0})$ where μ_{Na0} is the reference chemical potential of bulk Na metal. We evaluate the electrochemical stability of NAS against electrodes by constructing the Na-Sb-S ternary phase diagrams with Na chemical potential varying between μ_{Na0} and (μ_{Na0} - 3.5) eV.

The electronic conductivity of the phase equilibria at NAS/Na interface is also assessed by computing their electronic band gap. Given the well-known band gap underestimation by semi-local functionals[67], the Heyd-Scuseria Ernzerhof (HSE)[68] hybrid functional is adopted. Non-spin-polarized calculations with a k-point density of 500/(number of atoms in the unit cell) were utilized.

2.2.9 X-ray Photoelectron Spectroscopy (XPS)

The electrochemical cells were disassembled within the glovebox. To obtain the interphase samples, the Na metal was scraped off the small titanium plunger with a razor blade and the powder of interest was then collected. For the standards, Na_2S powder was collected as-is. Na_3Sb was synthesized via a stoichiometric mixture of Na and Sb via ball milling for 2 hours at 550 rpm, verified via XRD. Pristine Na_3SbS_4 powder was directly collected after synthesis. All samples were placed into glass vials and the vial caps were sealed with paraffin film.

The sealed vials were placed into a metal canister and the metal lid was screwed tightly to prevent moisture and oxygen ingress during transport outside of the glovebox. The sealed metal canister was re-introduced into a glovebox and the samples were mounted and transferred into the attached XPS tool (Kratos Axis Supra) from within the glovebox to avoid any exposure to ambient air. All measurements were taken using 15kV Al Kα radiation (with a 500mm Rowland circle monochromator) at a chamber pressure of approximately 10^{-8} torr. For the survey scans, a pass energy of 160eV and a dwell time of 100ms was used. For the specific element region scans, a pass energy of 20 eV and a dwell time of 300ms was used. For insulating samples such as Na_2S, the charge neutralizer was enabled.

Data calibration, analysis, and fitting were all performed by using CasaXPS. All region spectra for a given compound were calibrated to their corresponding adventitious carbon peak (C 1s, 284.8 eV) and the spectra were fitted using a Shirley-type background.

2.3 Results and Discussion

2.3.1 Synthesis and Ionic Conductivity of NAS

To verify that phase-pure NAS was synthesized, XRD was conducted on the post-ball-milled Na_3SbS_4 powder. The data and Rietveld refinement results are shown in Figure 2.1. The lattice parameters are consistent with the tetragonal phase of Na_3SbS_4 and are in good agreement with previously published values; the structure was solved with the P -4 2_1 c space group (No. 114). Thus, using Na_2S and elemental Sb and S, phase pure NAS was synthesized. Ball-milling was conducted due to Zhang et al.'s statement that hand mixing results in a non-uniform particle size distribution unfavorable for cold-pressing[19]. The Rietveld refinement results show that NAS retains the tetragonal phase even after ball milling.

To measure the ionic conductivity, EIS of an NAS pellet with blocking electrodes was measured. The EIS data and Arrhenius plot can be seen in Figure 2.2. After fitting the Nyquist plot and normalizing for the pellet dimensions, the room temperature conductivity was determined to be 1.06 mS cm^{-1}. The activation energy was calculated from the slope of the resulting Arrhenius plot and is 216 meV. These values are comparable to literature values; the ball-milled NAS has high room temperature ionic conductivity as expected[53].

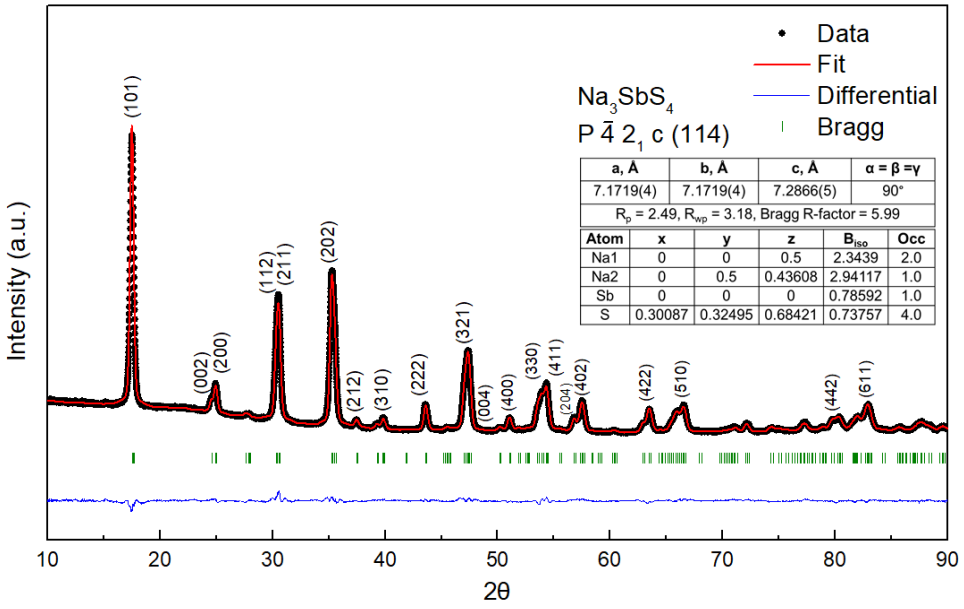

a, Å	b, Å	c, Å	α = β =γ
7.1719(4)	7.1719(4)	7.2866(5)	90°
R_p = 2.49, R_{wp} = 3.18, Bragg R-factor = 5.99			

Atom	x	y	z	B_{iso}	Occ
Na1	0	0	0.5	2.3439	2.0
Na2	0	0.5	0.43608	2.94117	1.0
Sb	0	0	0	0.78592	1.0
S	0.30087	0.32495	0.68421	0.73757	4.0

Figure 2.1. XRD data of heat-treated, post-ball-milled NAS. Inset: Rietveld refinement results, detailing lattice parameters, R-factors, atomic positions, thermal factors, and atom occupancies.

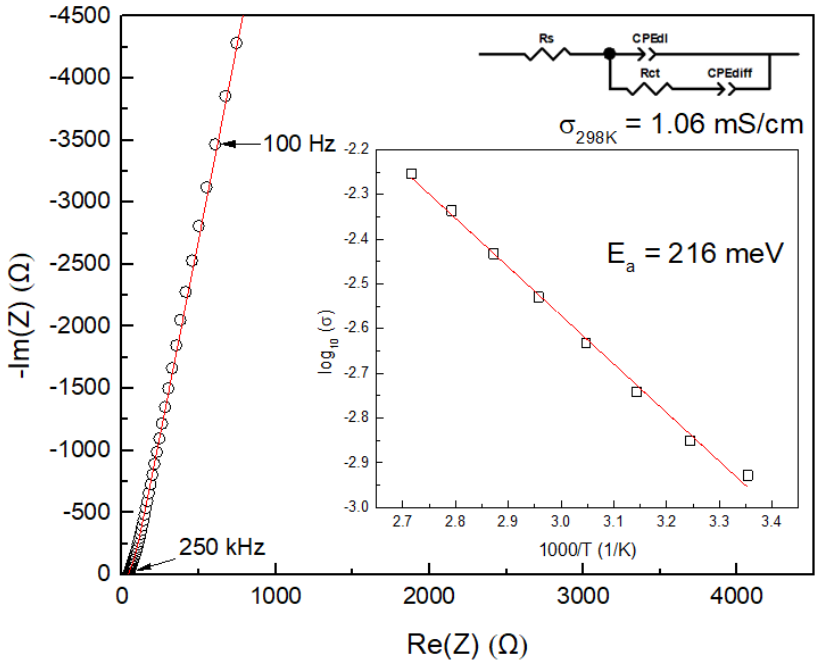

Figure 2.2. Room temperature Nyquist plot for ball-milled Na_3SbS_4 with the corresponding equivalent circuit model. Inset: Arrhenius plot of Na_3SbS_4, with the activation energy calculated from the slope.

2.3.2 Full Cell Electrochemical Behavior - NAS

Even though NAS possesses high Na ionic conductivity, to our knowledge there have been no reports on cycling of a full cell that utilizes NAS and a Na metal anode. To evaluate the performance of NAS in a full cell configuration, cells were constructed with a Na anode, NAS SSE, and a composite cathode (TiS_2:NAS in a 1:2 ratio). The choice of the TiS_2 cathode is motivated by its suitable operating voltage (~1.7 V versus Na/Na^+), its fast kinetics for Na^+ intercalation, as well as its high electronic conductivity[69,70]. The cell was galvanostatically cycled from 1.2 V to 2.4 V with a current density of approximately 50 $\mu A\ cm^{-2}$, corresponding to a C/10 rate. The typical cycling behavior of these cells is illustrated in Figure 2.3. The theoretical capacity of the $NaTiS_2$ active material is 198 mAh g^{-1}. The initial charge capacity is 115.9 mAh g^{-1}, yielding an initial Coulombic efficiency of 70.1%. One of the reasons that the observed specific capacity is lower than the theoretical is the low utilization of the cathode active material since the cathode composite was prepared via conventional hand mixing.

Rapid capacity fading is observed in the voltage profiles for the Na|NAS|NAS:TiS_2 full cell in Figure 2.3. The full cell lost over 92% of its capacity after 29 cycles which implies very poor cyclic stability. It is also interesting to note that around 98% of the capacity is retained between cycles 2-10, but eventually capacity fade becomes severe, until the cell can no longer cycle. This is certainly correlated with the polarization changes during cycling; there are negligible polarization changes for the first 10 cycles, but polarization becomes more pronounced upon subsequent cycling. Although NAS has a high ionic conductivity, the cyclic performance indicates that NAS is unstable against a Na metal anode. Capacity fade has also been observed in a $Na_{15}Sn_4$|NAS|$NaCrO_2$ full cell; therefore, it is crucial to understand the capacity fading mechanism for NAS[71].

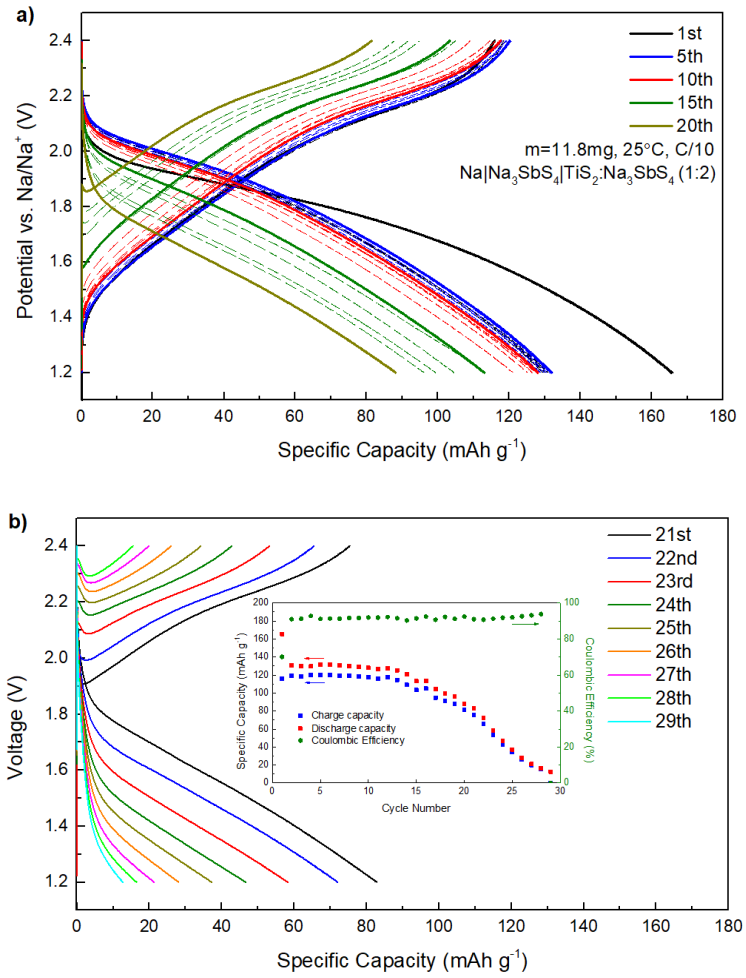

Figure 2.3. Electrochemical behavior of the Na|NAS|TiS_2:NAS cell. a) Voltage versus specific capacity for the first 20 cycles. Solid lines denote every 5th cycle and the dotted lines are the intermediate cycles. b) Cycles 21-29 for the same cell. Inset: Charge capacity, discharge capacity, and Coulombic efficiency versus cycle number.

To explore the reason behind the increasing polarization and the capacity fade, cyclic voltammetry (CV) was conducted on a Na|NAS|NAS:C (1:1 weight ratio) cell at a scan rate of 5 mV sec^{-1} to evaluate the electrochemical stability of NAS within the operating voltage window of the TiS_2-containing cell (1.2-2.4V). It is worth mentioning that we use NAS-C ball milled composite as a cathode to run the CV for electrochemical stability test; similar methods to measure the electrochemical stability of LGPS and NPS have also been previously reported[15,72]. The cyclic voltammogram for NAS is shown in Figure 2.4. The first cycle showed oxidation of NAS at a relatively low voltage of 1.4V along with a larger anodic current as the voltage increased past

1.95V which corresponds with the reduction peak at 1.84V. However, upon subsequent cycles, the anodic current decreases and the current response for cycles 2-20 is close to identical. This is indicative of the formation of the SSEI during the first cycle, as the observed current does not steadily increase with continued cycling, instead showing reversible oxidation and reduction as cycling proceeds. Therefore, we believe that the electrochemical stability of NAS within the 1.2 to 2.4V range does not contribute significantly to the observed poor cyclic performance of the full cell. Interestingly, LGPS was shown to have a narrow electrochemical stability window, but a full cell containing LGPS was still able to last for over 100 cycles[73]. The same observation was found in Li_3PS_4, which exhibited reversible oxidation and reduction within the voltage range of 0.8-3 V, and a cell lasted 300 cycles without a significant capacity loss[74]. This further suggests that degradation of NAS specifically within the 1.2-2.4V voltage window is not the primary cause of the capacity fade and cell failure.

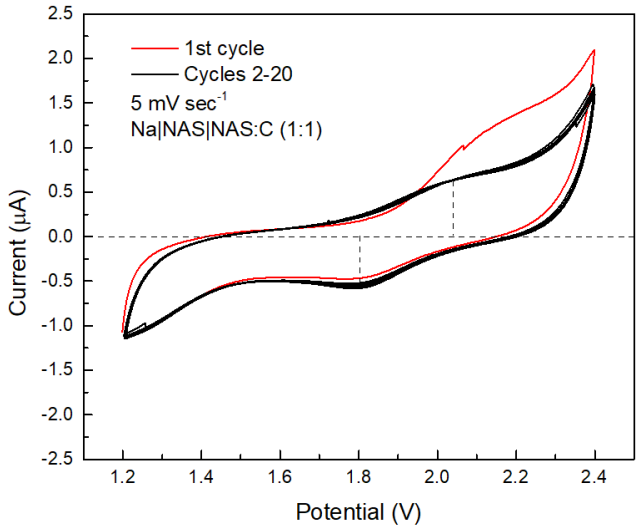

Figure 2.4. Cyclic Voltammogram of the Na|NAS|NAS:C (1:1) mixture. Cycle 1 is highlighted in red and subsequent cycles are in black.

Since electrochemical instability is not the major issue, the chemical stability of NAS with TiS_2 and Na metal was thus investigated. It is known that oxide cathodes react with sulfide SSEs which results in severe capacity fading and low power performance. However, since NAS and

TiS_2 are sulfides, the chemical potential difference is comparatively negligible and no chemical reaction at the NAS|TiS_2 interface is expected. XRD spectra of TiS_2 and NAS mixture was measured and the results are shown in Figure 2.5. In the pristine sample, the main observable peaks are attributed to NAS while after the first discharge and first charge, the onset of peaks from Na-intercalated $NaTiS_2$ and $Na_{0.55}TiS_2$ can be observed. The presence of these species in the charged sample can explain the initial irreversible capacity since that means not all the Na ions are extracted from TiS_2. More importantly, peaks from chemical reactions or from new phases are not present, clearly signifying chemical compatibility between NAS and TiS_2. While some Na ions remain in the TiS_2 upon charging, this is not the main reason of the onset of the severe capacity fade in the full cell.

The anode or Na|NAS interface was studied by constructing a Na|NAS|Na symmetric cell. The cell sat at rest and an EIS was recorded every hour over a time span of 50 hours and the Nyquist plot is shown in Figure 2.6. The cell was fit to an equivalent circuit to deconvolute the impedance contributions: the electrolyte resistance R_b, the SSEI resistance R_{int}, and the charge transfer resistance R_{ct} between the electrode and electrolyte[75]. Figure 2.6 shows that the magnitude of all of the components continually and gradually increases with time simply due to contact between NAS and Na metal without any biasing. We observe an increase in the bulk and charge transfer resistances, attributed to changes in the SSE as Na ions are continuously consumed from NAS to form and grow the SSEI. It is also interesting to notice that R_{ct} also increases for the symmetric cell which could be increasing due to poorer contact of the Na with NAS arising from the growth of the SSEI[76]. Since the cathodic contribution on cell fading is negligible, this result indicates that the anodic contribution is the dominant factor.

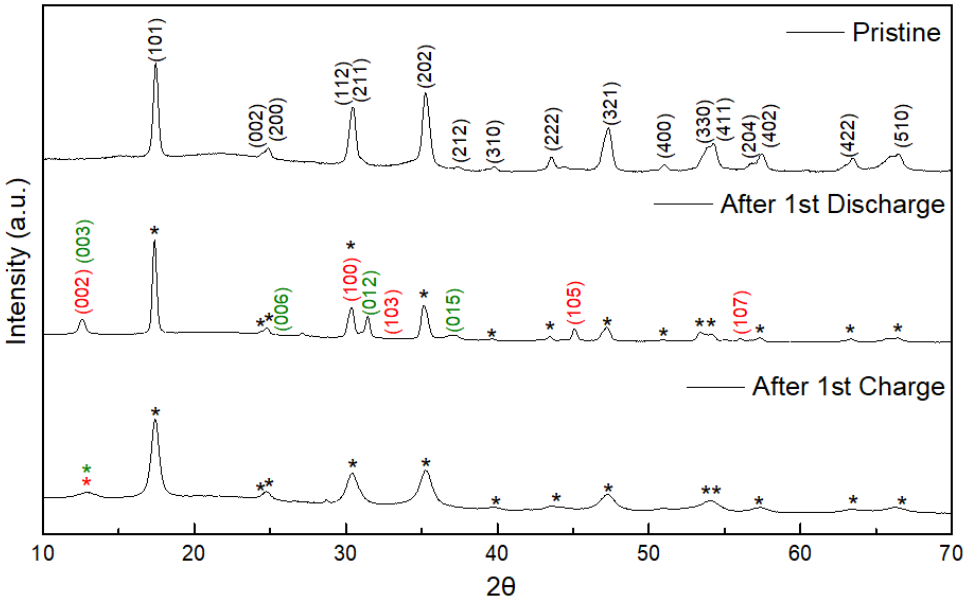

Figure 2.5. XRD of the TiS_2:NAS (1:2) composite cathode. NAS diffraction peaks are marked in black, while red and green are peaks associated with $NaTiS_2$ and $Na_{0.55}TiS_2$, respectively.

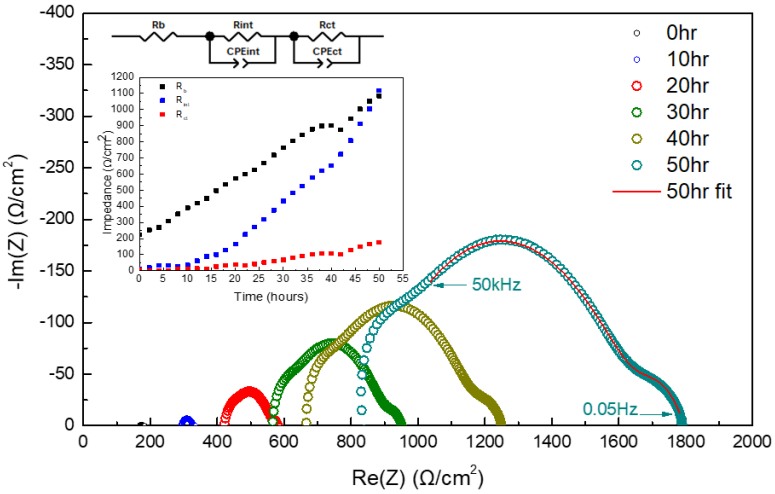

Figure 2.6. Nyquist plot of the Na|Na_3SbS_4|Na symmetric cell from 0 to 50 hours, showing the increasing impedance with time. Inset: equivalent circuit used to fit the data with a corresponding fit plotted on the 50 hr curve. Inset: the fitted impedance components with time.

As previously shown in Figure 2.3, the cell polarization increases as cycling proceeds, signifying a steady increase in the impedance of the cell as time goes on. This impedance increase over time is further suggested by the symmetric cell impedance in Figure 2.6. To correlate the symmetric cell impedance growth to the full cell behavior, impedance measurements

of the full cell after charging and discharging was also conducted, and the results are shown in Figure 2.7. The cell components were fit to the Li-ion battery equivalent circuit model[77,78]. As cycling proceeds, R_{sei} is the only component with a significant increase, consistent with the symmetric cell results. It is important to note that R_{sei} increases more drastically upon subsequent charging, as seen in Figure 2.7b. This is intuitive since Na nucleates on the anode side during charging, which would expose it to NAS. This means the reaction with NAS is electrochemically facilitated during cycling. From both the symmetric cell and full cell impedance measurements, the Na|NAS interphase appears to be not static, but rather dynamic, or growing significantly with time. Previous reports indicated that LGPS formed a dynamic interface with Li metal due to the formation of ion-conducting (Li_3P) and electronic-conducting components (Li-Ge alloy) at the interface[79]. In contrast, LPSI forms a stable SEI with Li metal as the SEI was a mixture of ionic-conducting and electronically-insulating components, which prevents continued decomposition of the SSE[79]. The nature of the impedance at the Na|NAS interface clearly indicates that there must be an electronically conductive component at the SEI. So far there have been no studies on the Na|NAS interface; therefore, it is necessary to find out the chemical species of the SSEI to explain their effects on the cycling behavior.

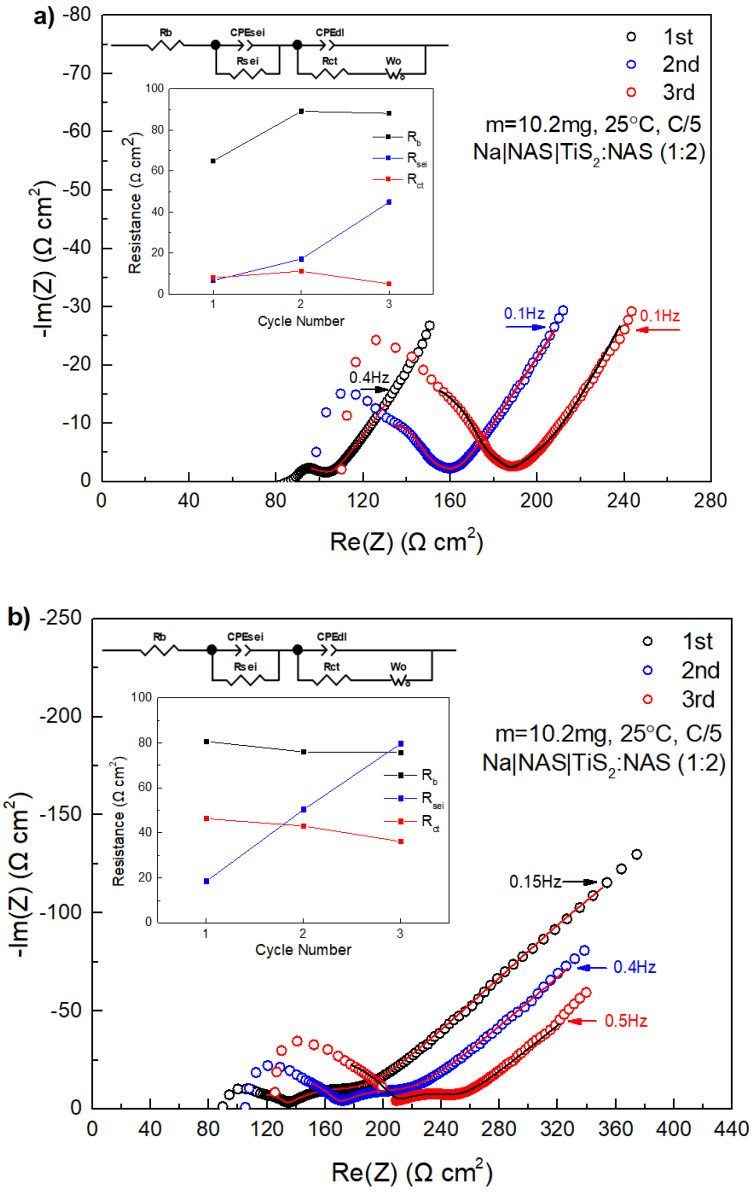

Figure 2.7. Full cell *in situ* impedance measurements for a) 1st-3rd discharge and b) 1st-3rd charge. Insets: fitted resistance components versus cycle number.

To predict the compounds at the Na|NAS interface, computation of the phase equilibria at the Na|NAS interface was conducted. Figure 2.8 shows the Na grand potential phase stability plot of the NAS solid electrolyte as a function of Na chemical potential. We find that at the Na|NAS interface, NAS decomposes into Na_3Sb and Na_2S, a known metallic alloy and an insulator at room temperature, respectively[80,81]. To confirm this, the electronic band gaps were calculated to be

0.68 eV and 3.22 eV for Na_3Sb and Na_2S, respectively (see Figure 2.9). In order to experimentally investigate the compositions of the Na|NAS interface, XPS was conducted on the pristine electrolyte, the Na|NAS interface from a cycled cell, and the Na|NAS interface from a symmetric cell. Figure 2.10a shows the S 2p region scan for these samples plus the scan for the Na_2S precursor. An example fit of the S region scan for the cycled anode interface sample shown in Figure 2.11. In addition, the peak positions and parameters for every component in our XPS fittings are detailed in Tables 2.1 and 2.2. Compared to the pristine electrolyte, all samples that contacted Na have an additional peak at 159.4 eV consistent with the binding energy of Na_2S[82], thus confirming Na_2S as a decomposition product at the Na|NAS interface.

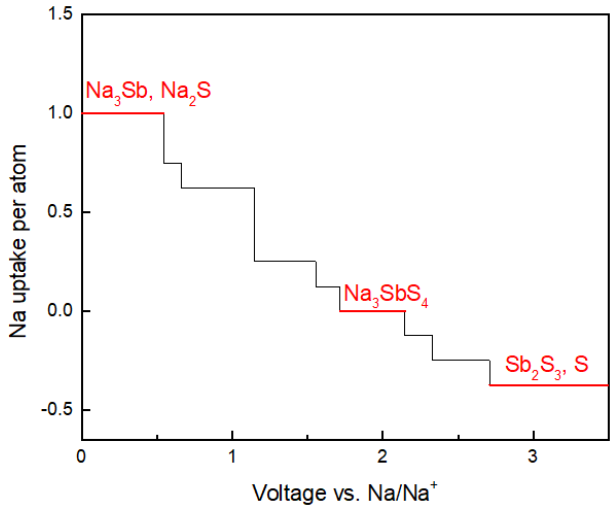

Figure 2.8. Na grand potential phase stability plots for Na_3SbS_4. In the anodic or low voltage region, Na_3SbS_4 undergoes a reduction process and uptakes Na whereas in the cathodic or high voltage region, it undergoes oxidation and loses Na. Compounds listed the plot are predicted phase equilibria at corresponding regions.

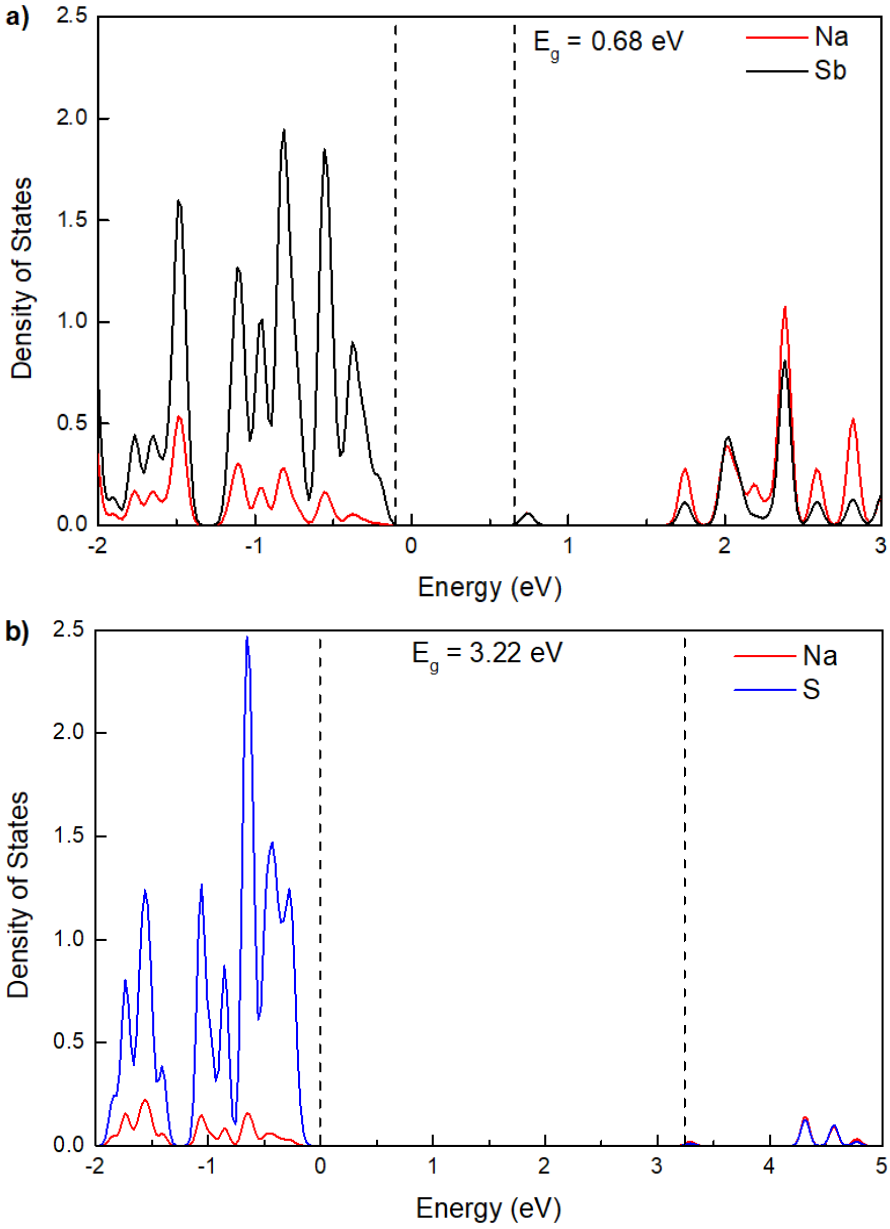

Figure 2.9. Density of States calculation for a) Na_3Sb and b) Na_2S, showing a bandgap of 0.68eV and 3.22 eV for the respective compounds.

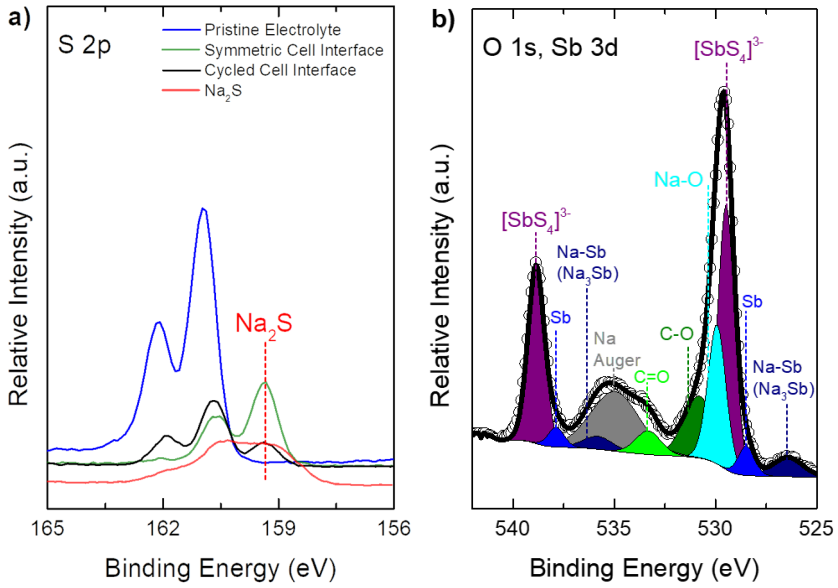

Figure 2.10. a) S 2p region scan of the pristine NAS, anode interface of the cell cycled to completion, the symmetric cell, and the Na_2S precursor, overlaid on top of each other. b) O 1s/Sb 3d region scan of the Na|NAS SSEI from the cell cycled to completion.

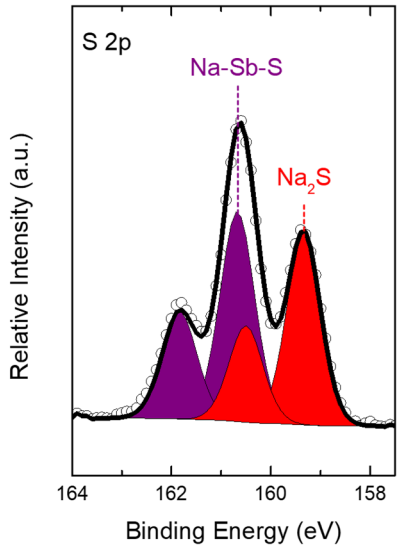

Figure 2.11 S 2p region scan of the anode interface of the cycled cell, illustrating the onset of the Na_2S peak (red).

Table 2.1. XPS binding energies for NAS and NPS components. Bold denotes experimental values, non-bold are literature values.

NAS

Surface Component	S $2p_{3/2}$	Sb $3d_{5/2}$	O 1s
SbS_4^{3-}	**160.7-160.9** 161.6[1] 161.4[2]	**529.5** 529.6[1] 529.2[3]	
Na_2S	**159.3** 159.4[4] 158.7[5]		
Sb		**528.5-528.7** 528.3[3] 528.5[6]	
Na_3Sb		**526.5-526.7**	
Na-O			**529.9-530.3** 529.7[3] 529.6[7]
Na Auger			**534.0-536.0** 535-537[8]
C-O			**530.5-532.0** 531.6[8]
C=O			**533.3** 533[8]

NPS

Surface Component	S $2p_{3/2}$	P 2p	Cl 2p
P-S-Na	**160.7** 160.9[4] 160.0[5]		
P=S	**161.8** 161.0[5]		
Na_2S	**159.4** 159.4[4] 158.7[5]		
PS_4^{3-}		**131.3** 131.4[4] 131.0[5]	
S-P-Cl		**132.2**	**198.5**
Na_3P		**124.4** 125.0[5]	
Reduced P		**126.8** 126.5[5]	
NaCl			**198.1** 198.2[9] 198.3[10]

Table 2.2. XPS fit parameters of NAS, Na_3Sb, and Na_2S using a Shirley background and GL(30) Gaussian Lorentzian line shape.

		S 2p$_{3/2}$ SbS_4^{3-}	**S 2p$_{3/2}$ Na_2S**	**Sb 3d$_{5/2}$ SbS_4^{3-}**	**Sb 3d$_{5/2}$ Na_3Sb**	**Sb 3d$_{5/2}$ Sb**	**O 1s Na-O**	**Na Auger**	**O 1s C-O**
Na_2S	Area		3779.2						
	FWHM (eV)		1.5						
	Binding Energy (eV)		159.3						
Na_3Sb	Area				3672.3		11095.2	5498.6	1520.3
	FWHM (eV)				1.4		1.6	2.7	1.7
	Binding Energy (eV)				526.7		530.3	536.0	532.0
Pristine NAS	Area	14229.1		52472.3		4330.4		7506.3	3143.9
	FWHM (eV)	0.8		1.0		1.0		1.4	1.4
	Binding Energy (eV)	160.9		529.7		528.7		534.0	531.2
Cycled NAS	Area	3232.4	2864.6	10210.3	1357.0	1109.0	5897.9	6761.8	6775.0
	FWHM (eV)	0.8	0.8	1.0	1.7	1.0	1.0	2.8	1.8
	Binding Energy (eV)	160.7	159.3	529.6	526.5	528.5	529.9	535.0	530.5

As for Na_3Sb, there were no reports containing a XRD or XPS measurement for this compound to the best of our knowledge. Before the Sb 3d region of the SSEI could be analyzed, Na_3Sb had to be synthesized to serve as a measurement standard. The XRD pattern and the O 1s/Sb 3d XPS region scan of the as-synthesized Na_3Sb is shown in Figure 2.12; phase-pure Na_3Sb was confirmed from the XRD measurement. In addition, the O 1s/Sb 3d XPS region scan of pristine NAS is shown in Figure 2.13. With these spectra, the O 1s/Sb 3d spectrum of the cycled anode-electrolyte interface, shown in Figure 2.10b, can be deconvoluted. Sb XPS peaks have a characteristic separation of 9.39 eV of the 3d orbitals and a symmetric peak shape[83]. Comparing with Figure 2.13, it can be deduced that two doublets (the Sb $3d_{5/2}$ peaks at 529.5eV and 528.5eV and the respective Sb $3d_{3/2}$ peaks at 538.9 and 537.9 eV) come from NAS. Using Figure 2.12, the Sb $3d_{5/2}$ peak at 526.4 eV and the Sb $3d_{3/2}$ peak at 535.8 eV can be attributed to Na_3Sb. This is reasonable as a less positive oxidation state corresponds to a shift towards lower binding energy[84]. The sodium oxide signal likely comes from species such as Na_2SO_3 and $Na_2S_2O_3$, common impurities found in Na_2S. Ultimately, from the deconvolutions of the O1s/Sb 3d region and S 2p region scans of the SSEI, both Na_3Sb and Na_2S are confirmed to form at the Na|NAS interface. These findings are in excellent agreement with our computational results. The low band gap of

Na_3Sb clearly indicates an electronically-conductive component of the SSEI which facilitates the continuous formation and growth of the SSEI until proceeding to completion, resulting in the increase of the overall cell impedance over time. In turn, this results in the continuous increase in polarization with cycling, negatively impacting the battery performance and cycle life until cell failure.

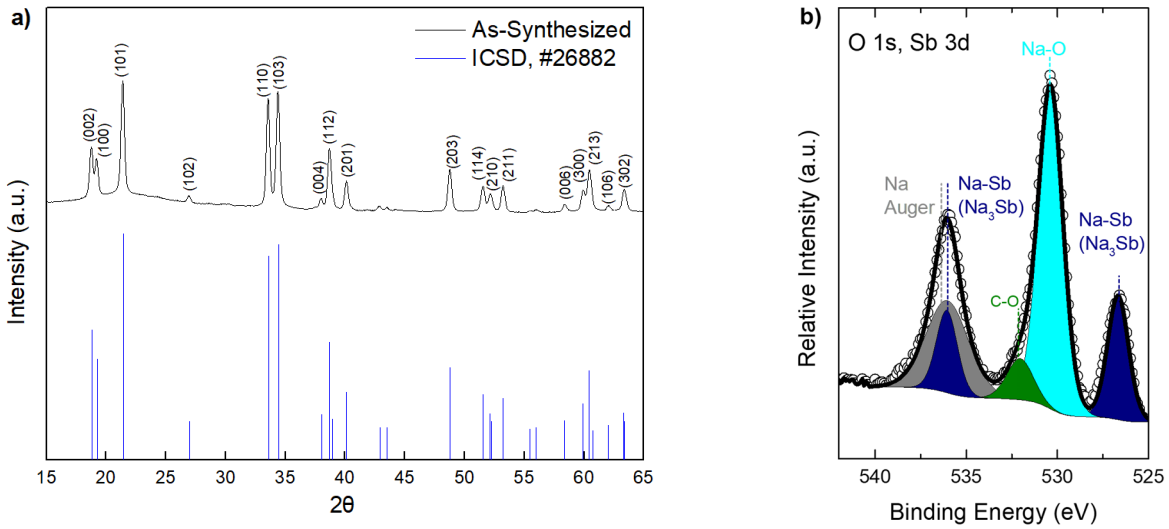

Figure 2.12. a) XRD pattern of the as-synthesized Na_3Sb[85]. b) XPS O 1s/Sb 3d region scan for the as-synthesized Na_3Sb.

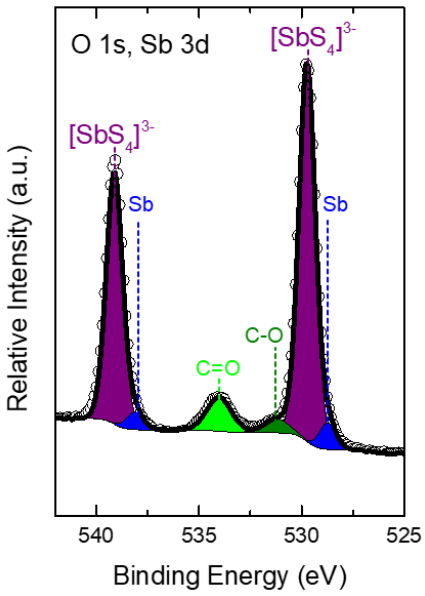

Figure 2.13. XPS O 1s/Sb 3d region scan for the pristine Na_3SbS_4 electrolyte.

The previous results suggest that bare NAS coupled with Na is unsuitable for a long-term ASSB due to the chemical instability which contributes to cell failure. We believe that modification of existing electrolytes or finding a suitable anode to improve the compatibility with Na metal are strategies to prolong the cycle life of ASSBs. One such modification applied in our previous work is Cl-doping of NPS, which was found to increase the room temperature ionic conductivity to over 1 mS cm^{-1} [55]. To investigate the effect of Cl-doping on the Na|NPS interfacial stability, symmetric cells using Na metal were assembled. A galvanic square-wave was pulsed through symmetric cells with NPS and NPSC and the voltage was measured. The data is shown in Figure 2.14 To quantify the effect of the Cl-doping on the interface stability, the area-specific resistance (ASR) was then calculated following Ohm's law and using the area of the pellet, 1.317 cm^2. For the NPS, NPSC (6.25%), and NPSC (12.5%) samples, the calculated ASR grew from 1986 Ω cm^2 to 3740 Ω cm^2, 992 Ω cm^2 to 2139 Ω cm^2, and 6372 Ω cm^2 to 7163 Ω cm^2, respectively, corresponding to percent increases of 88.3%, 115.6%, and a 12.4%. A comparison of the ASR values is also shown in Figure 2.14d. Although the ASR of the 12.5% NPSC was more stable over time, it had a much larger initial ASR. This suggests that there is an optimal Cl-doping concentration at which the highest conductivity for NPSC is achieved. These ASR values suggest that while further increasing the Cl content can improve interfacial stability, it will also lead to diminished conductivities by destabilizing the framework which could inhibit ionically-conducting percolation pathways. This is supported by our previous computational results as increasing the concentration of Cl-doping from 6.25% to 12.5% increased the dopant formation energy from 0.96 eV to 1.77 eV[55]. This suggests that increased Cl-doping, which increases the concentration of Na vacancies, introduced more disorder in the structure. Taking the product of the ASR and the current density, the expected voltaic loss across the NPS interphase starts at approximately 100 mV and increases to almost 200 mV. In the 6.25% NPSC case, the over-potential increases from just under 50 mV to about 100 mV. The 12.5% NPSC cell had a voltaic loss of about 300 mV, most

detrimental to the cyclability of the cell. This indicates that while increasing the Cl^- content in the electrolyte can improve the stability of the interphase, there appears to be a compromise between stability and conductivity. The NPSC 6.25% cell, with the overall lower ASR, strikes the better balance between the two properties.

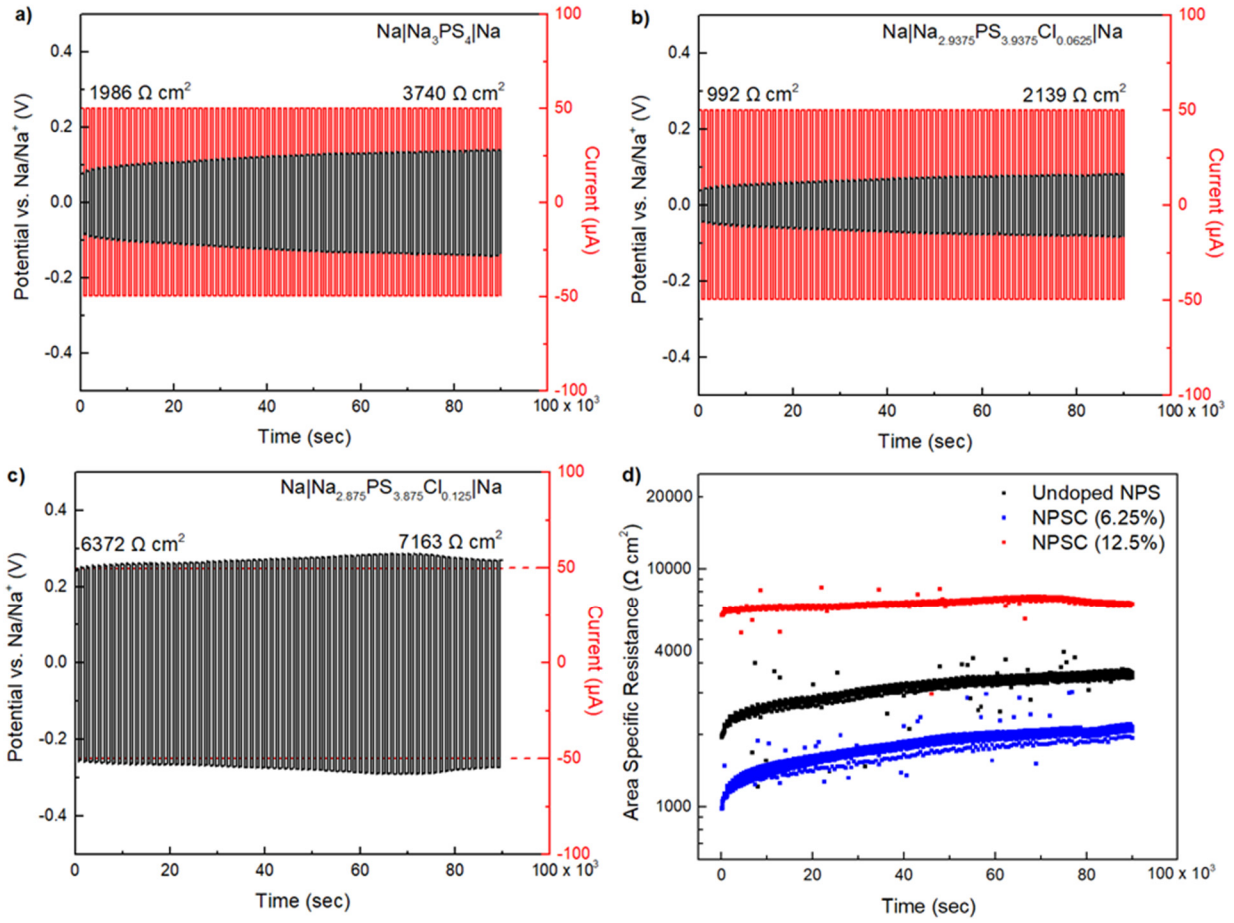

Figure 2.14. Galvanic square-wave cycling of a) Na|NPS|Na symmetric cell and b) Na|NPSC|Na (x = 6.25%) symmetric cell and c) Na|NPSC|Na (x = 12.5%) symmetric cell. The area-specific resistance (ASR) was calculated following Ohm's law. d) Comparison of ASR versus time for the aforementioned symmetric cells.

Full cells comprising of NPS and 6.25% NPSC were constructed, and the charge-discharge profile of the NPS and NPSC full-cells are shown in Figure 2.15a and 2.15b, respectively. The capacity and Coulombic efficiency are plotted in Figure 2.15c. After 10 cycles, the specific capacities of the NPS and NPSC cells were ~70 mAh g^{-1} and 110 mAh g^{-1},

respectively. Both cells show capacity fade but it is important to note that the NPSC cell exhibited better capacity retention than the undoped NPS cell. Also, compared to our previous work, where the NPSC cell had a specific capacity of 80 mAh g^{-1} after 10 cycles, the observed 110 mAh g^{-1} for this NPSC cell is owed to better preparation and mixing of the composite cathode[55]. Ultimately, the better capacity retention suggest that Cl-doping improved the interfacial stability in a full cell; thus, doping the electrolyte could also be a promising strategy to improve the stability of NAS.

To investigate the products at the SSEI for the NPS and NPSC samples, the XPS spectra are shown in Figure 2.16. In NPS, we observe two spin-orbit doublets in the S 2p envelope that are characteristic of the P-S-Na (160.7 eV) and P=S (161.8 eV) bonding states. In the P 2p region, there is a single doublet associated with the tetrahedrally-coordinated P in $[PS_4]^{3-}$ at 131.3 eV. Upon cycling, there is the onset of a new spin-orbital doublet in the S 2p region; as with NAS, this peak is observed around 159.4 eV and attributed to Na_2S[82]. In addition, two more spin-orbital doublets appear in the P 2p region after cycling; Na_3P is found at 124.8 eV and a reduced phosphorus phase is at 126.8 eV. These findings are consistent with those reported in previous literature[64]. For the doped samples (NPSC), the pristine spectrum is similar to NPS with an additional doublet in the P 2p and Cl 2p regions, ascribed to S-P-Cl bonding, indicating that Cl^- was successfully incorporated in the $[PS_4]^{3-}$ tetrahedra. After cycling, NaCl, a predicted decomposition product, is found at 198 eV[64]. All other decomposition products are similar to those of NPS. We speculate that the decomposition reaction is as follows for NPS and NPSC samples:

$$Na_3PS_4 + 8\ Na \rightarrow 4\ Na_2S + Na_3P \quad (3)$$

$$Na_{47}P_{16}S_{63}Cl + 128\ Na \rightarrow 63\ Na_2S + 16\ Na_3P + NaCl \quad (4)$$

$$Na_{3-x}PS_{4-x}Cl_x + 8\ Na \rightarrow (4-x)\ Na_2S + Na_3P + x\ NaCl \quad (5)$$

In this case, $Na_{47}P_{16}S_{63}Cl$ in Eq. 4 is an analogous stoichiometric ratio to 6.25% (atomic percent) Cl-doped Na_3PS_4. In the final equation, we demonstrate how the electrolyte could be synthetically designed to yield an interphase with a tunable salt content.

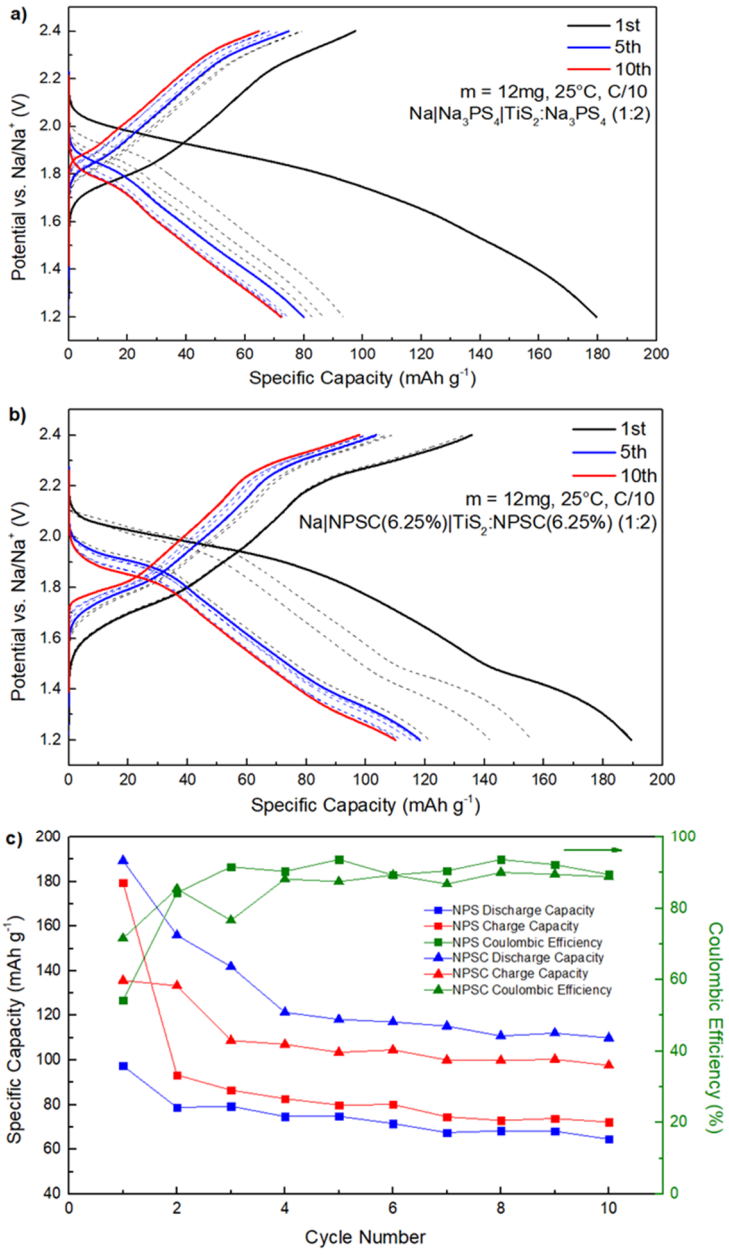

Figure 2.15. Galvanostatic cycling of Na-TiS_2 cell using a) NPS and b) NPSC. Cells were cycled at room temperature from 1.2 V to 2.4 V at a current density of about 50 μA cm^{-2} which corresponds to a C/10 rate. c) Charge capacity, discharge capacity, and Coulombic efficiency versus cycle number for the respective cells.

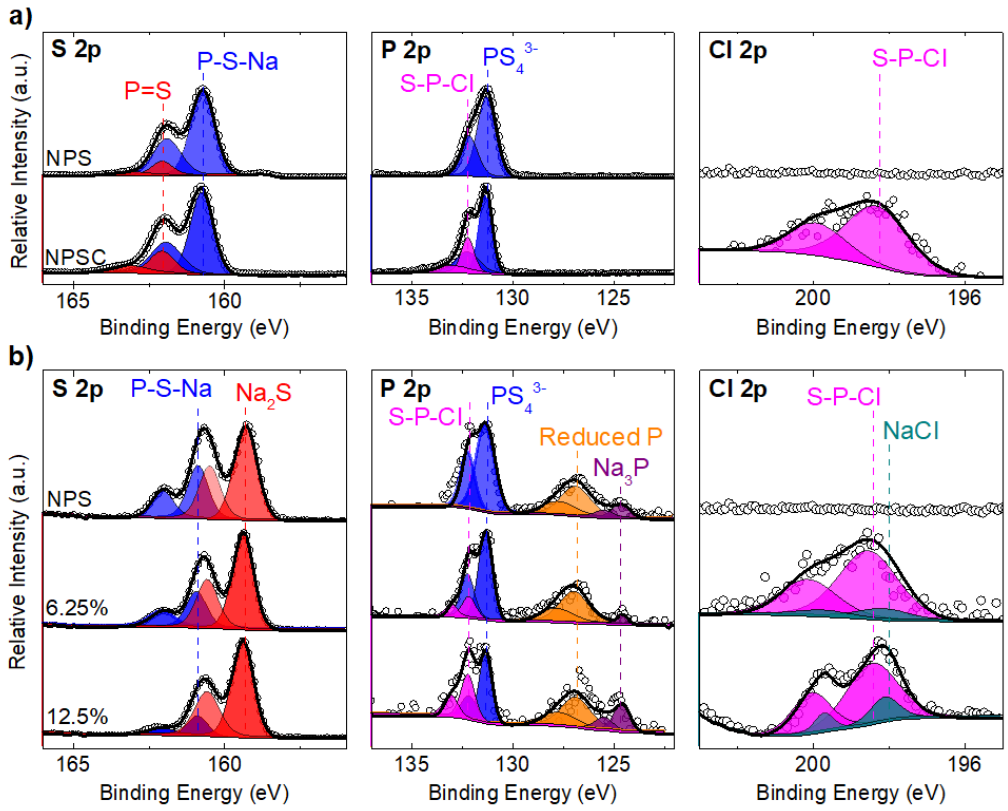

Figure 2.16. S 2p, P 2p, and Cl 2p region scans of (a) pristine NPS and NPSC and (b) SSEI after cycling of NPS, 6.25% doped NPSC, and 12.5% doped NPSC.

We find that NAS, NPS, and NPSC all degrade in the presence of Na metal, and this reaction proceeds gradually until completion to the detriment of electrochemical cell performance. In all three cases, this behavior is characteristic of the formation of an interphase with both ionic and electronic-conducting species. This is reasonable because although we find Na_2S and polysulfides in the interphase, we also find Na_3P for NPS and Na_3Sb for NAS, which are known to have a low bandgap (0.4 eV and 0.68 eV, respectively). For NPSC, we also detect NaCl as a component in the interphase, which is an electronic insulator. NaCl could provide passivating qualities to improve cell performance, or in other words, slow down the kinetics of the degradation. Moreover, in contrast to many other attempts to dope Na_3PS_4 via a metallic cation (M^{4+}, M = Si, Ge, Sn), NaCl advantageously suppresses electronic percolation through the SSE and the interphase[64]. Finally, we implemented the NPSC in an all-solid-state battery. The cell assembled

with $Na_{2.9375}PS_{3.9375}Cl_{0.0625}$ retained more capacity with lower overpotentials over 10 cycles. We demonstrate that considering SSE compatibility with metallic anodes is essential to extend the lifetime of an ASSB.

2.4 Conclusion

The decomposition mechanism for the solid electrolytes Na_3SbS_4 and Na_3PS_4 was investigated as these materials have good ionic conductivity, but also are known to be unstable against Na metal, the latter being a persistent obstacle to wide-scale adoption of ASSBs. It was found that for these SSEs, the SSEI at the anode continuously grows into a thick layer impeding electrochemical performance. In this work, XPS was applied to identify and confirm the compounds at the SSEI that were predicted computationally, which can provide insight on the cycling behavior of the battery. This methodology is a step towards more effective computational screening of SSE materials, as a favorable ionic conductivity of the electrolyte on its own is not sufficient to enable reversible all-solid-state batteries. The stability of a solid electrolyte against anodes and cathodes must be considered and evaluated in order to realize the most promising and practical solid-state battery chemistries. It was shown that electrolyte modification by Cl-doping of NPS is a method to improve cyclability as Cl-doping resulted in cells with better capacity retention compared to undoped NPS, suggesting Cl-doping can passivate or stabilize the interface. Future work such as: evaluating other electrolytes in this manner, designing and optimizing the interfaces via electrolyte modification such as doping and mixing, analyzing different compounds for a suitable anode, or interface engineering with protective coatings for the metal anode or electrolyte, all present worthwhile opportunities to gain a more complete understanding to improve the performance and longevity of Na ASSBs. In conjunction with these experimental evaluations, thermodynamic calculations and first principles computation can help inform and accelerate such studies. Ultimately, the goals of extending the cycle life and increasing the energy density through the use of metallic anodes remain paramount if ASSBs are to be viable.

Chapter 2, in full, is a reprint of the material “New Insights into the Interphase between the Na Metal Anode and Sulfide Solid-State Electrolytes: A Joint Experimental and Computational Study” as it appears in ACS Applied Materials and Interfaces. Wu, E. A.*, Kompella, C. S., Zhu, Z., Lee, J. Z., Lee, S. C., Chu, I.-H., Nguyen, H., Ong, S. P., Banerjee, A., and Meng, Y. S. 2018, 10, 12, 10076-10086. The dissertation author was the first author of this paper. The dissertation author carried out all the experiments and electrochemical testing herein, except for the NPS/NPSC electrochemical testing and XPS, which were carried out by Kompella, C. S., and Lee, J. Z.

Chapter 3. The Halide $Na_{3-x}Y_{1-x}Zr_xCl_6$ for Longer-Lasting Sodium Ion Batteries

Rechargeable solid-state sodium-ion batteries (SSSBs) hold great promise for safer and more energy-dense energy storage. However, the poor electrochemical stability between current sulfide-based solid electrolytes and high-voltage oxide cathodes has limited their long-term cycling performance and practicality. Here, we report the discovery of $Na_{3-x}Y_{1-x}Zr_xCl_6$ (NYZC) as an ion conductor that is both electrochemically stable (up to 3.8 V vs. Na/Na^+) and chemically compatible with oxide cathodes. Its high ionic conductivity of 6.6 x 10^{-5} S cm^{-1} at ambient temperature, several orders of magnitude higher than oxide coatings, is attributed to abundant Na vacancies and cooperative MCl_6 rotation, resulting in an extremely low interfacial impedance. A SSSB comprising a $NaCrO_2$+NYZC composite cathode, Na_3PS_4 electrolyte, and Na-Sn anode exhibits an exceptional first-cycle Coulombic efficiency of 97.1% at room temperature and can cycle over 1000 cycles with 89.3% capacity retention at 40°C. These findings highlight the immense potential of halide ion conductors for SSSB applications.

3.1 Introduction

A solid-state architecture for rechargeable sodium-ion batteries has garnered substantial research interest in recent years.[9,10,12,18,86] By replacing flammable organic liquid electrolytes with solid electrolytes (SEs), solid-state sodium-ion batteries (SSSB) promise not only higher safety, but also potentially enable higher voltage cathodes, metal anodes, and stacking architectures to achieve higher energy densities. In addition, the higher abundance of sodium relative to lithium makes sodium-ion batteries a more cost-effective alternative, especially for large-scale grid storage applications where low operating costs are more strongly emphasized than a high energy density.[87] However, an ideal SE has to meet a stringent set of requirements, namely high ionic conductivity, low electronic conductivity, and electrochemical, chemical, and mechanical compatibility with electrodes. While major breakthroughs have been made in achieving liquid-like

ionic conductivities in sulfide SEs, their poor electrochemical and chemical interfacial stability against common electrodes remains a critical bottleneck for practical applications.

Recently, two lithium halide superionic conductors, Li_3YCl_6 and Li_3YBr_6, have been reported as promising SEs for solid-state lithium-ion batteries.[88] Exhibiting reasonable Li^+ conductivities in the range of 0.5-0.7 mS cm^{-1}, the most interesting feature of these halide SEs is their electrochemical and chemical compatibility with the 4 V $LiCoO_2$ cathode. As a result, more reports have emerged on similar halides (Li_3InCl_6 and Li_xScCl_{3+x}) that also exhibit high Li^+ diffusivity, compatibility with $LiCoO_2$, and facile processability.[89,90,91] Interestingly, unlike the fast Li-ion conducting sulfides or oxides, fast Li-ion conduction in these halide frameworks do not require a bcc anion sublattice, allowing a much wider selection of compositions when designing halide SE chemistries. The Na analogues Na_3YCl_6 and Na_3YBr_6 have been relatively less studied. Previous studies have reported experimental ionic conductivities for these compounds on the order of 10^{-4}-10^{-6} S/cm at 500K. These materials are therefore expected to have much lower room-temperature ionic conductivities than their lithium counterparts and to be impractical for SE applications.[92]

Here, we report the development of $Na_{3-x}Y_{1-x}Zr_xCl_6$ (NYZC*x*) as a new class of sodium SEs exhibiting high ionic conductivities as well as excellent electrochemical and chemical stability up to 3.8V vs Na/Na^+. A SSSB comprising a $NaCrO_2$:NYZC0.75:vapor grown carbon fibers (VGCF) composite cathode with Na_3PS_4 as the SE and a Na-Sn (2:1) anode exhibited an extremely high first cycle Coulombic efficiency (CE) of 97.6% at room temperature. Even when cycled at 40°C and a rate of 1C, the SSSB displayed stable electrochemical performance over 1000 cycles with 89.3% capacity retention.

3.2 Methods

3.2.1 Computational Methods

3.2.1.1 Structural relaxations and energy calculations

The pre-relaxed structures of Na_3YCl_6 (mp-31362) and Na_3YBr_6 (mp-29080) were extracted from the Materials Project (MP) database[93,94]. The corresponding ICSD[95] ids are #59886 and #82355, respectively. Aliovalent substitution on the Y^{3+} sites with charge compensation by Na^+ vacancies were performed to generate $Na_{3-(z-3)x}Y_{1-x}M^{z+}{}_xCl_6$ (M = Ti^{4+}, Zr^{4+}, Hf^{4+}, Ta^{5+}) structures. DFT calculations were performed on all symmetrically distinct orderings of Y/M and Na/vacancies to identify the lowest energy structure. Candidate structures for the hitherto-unreported Na_2ZrCl_6 phase were obtained by performing ionic substitutions of all structures in MP database matching the formula of A_2MX_6. All candidate structures were fully relaxed using DFT prior to calculating their energies. The computed XRD pattern of the lowest energy candidate was successfully matched to the experimental XRD pattern.

Other than the target phases of interest, the pre-computed energies of all other structures in the Na-Y-Zr-Cl phase space were obtained from the Materials Project database and used in the calculation of the energy above hull (E_{hull}), electrochemical stability window, and the interfacial reaction products following the methodologies established in prior publications.[96,97]

3.2.1.2 Ab initio molecular dynamics

Non-spin polarized ab initio molecular dynamics (AIMD) simulations were carried out in the NVT ensemble. A plane-wave energy cutoff of 280 eV, supercells with the minimum dimension larger than 10 Å and a minimal Γ-centered 1×1×1 k-mesh were used. The time step was set to 2 fs. Simulations were carried out at several temperatures between 500 K and 1200 K and the corresponding diffusivities were extracted using the Nernst-Einstein relationship from the slope of the plot of the mean square displacement of Na ions with time.

3.2.2 Experimental Synthesis and Characterization

3.2.2.1 Material Synthesis

All fabrication processes were conducted in an Ar-filled glovebox (mBraun 200B, H_2O ppm <0.5, O_2 ppm < 1), unless otherwise noted.

Stoichiometric amounts of the precursors NaCl (>99%, Sigma Aldrich), YCl_3, (99.9%, Sigma Aldrich) were hand-mixed in a mortar and pestle for 10 minutes and the powder mixture was placed in a 50 mL ZrO_2 ball mill jar (Retsch Emax) with eleven 10 mm-diameter Y-ZrO_2 milling balls. The mixture was milled for 2 hours at 500 rpm. The material was extracted from the jars in the glovebox, pelletized at a pressure of 370 MPa with a 13 mm pellet die (Carver), loaded into a quartz tube, flame sealed, and heated in a box furnace (Lindberg Blue M) at 500 °C for 24 hours. To homogenize the material, the material was ball milled again after heat treatment using 88 5 mm diameter Y-ZrO_2 milling balls for a duration of 4 hours. The material was extracted and stored in the glovebox before further testing.

For the Zr substituted compounds, the same procedure was conducted with the addition of $ZrCl_4$ (99.99%, Sigma Aldrich) as a third precursor, and the reagent ratios adjusted according to stoichiometry.

3.2.2.2 Characterization – XRD

Powder samples were loaded into 0.5 mm-diameter boron-rich capillary tubes (Charles Supper). The tube opening was capped with clay and wrapped in paraffin film before it was brought outside of the glovebox to be flame-sealed with a butane torch. The samples were measured on a Bruker Kappa goniometer equipped with a Bruker Vantec 500 detector. The sample was placed in the Bragg−Brentano θ−θ configuration and the Debye−Scherrer method was used for measurements. XRD data was collected using Cu Kα radiation at 45 kV and 50 mA, over a 2θ range of 5−90° with a step size of 0.01°.

For temperature-dependent capillary XRD, the capillary tubes were heated at a rate of 5°C/min and held at the target temperature for one hour before the XRD measurement was taken.

For Synchrotron XRD, the samples were prepared by loading the powders into polyimide tubes in the glovebox and were subsequently sealed with epoxy. Measurements were carried out at Beamline 28-ID-1 at NSLS-II.

3.2.2.3 Characterization – Electrochemical

The powder was pressed at 370 MPa into a 10 mm polyether ether ketone (PEEK die) using two titanium plungers. On both sides of the pellet, acetylene black (AB) was added for better contact with the current collectors; once added, the AB was pressed at 370 MPa using the titanium plungers. The cell configuration was secured into a cell holder and connected to a Solartron 1260 impedance analyzer. Impedance measurements were taken with an applied AC potential of 30 mV over a frequency range of 1 MHz to 1 Hz. Temperature-dependent EIS measurements were also conducted within the glovebox; the sample was heated from 20 °C to 100 °C and EIS measurements were recorded at every 20 °C increment. Measurements were taken only after the sample was held at the target temperature for over an hour to allow for equilibration. The heating rate was 2 °C/min. The activation energy (E_a) was calculated from the slope of the resulting Arrhenius plot.

DC polarization was also conducted by the Solartron 1260 impedance analyzer. The cell setup was similar as before; the powder was pressed at 370 MPa into a 10 mm PEEK die using two titanium plungers and subsequently secured into a cell holder. The applied DC potential was 50 mV and the current response was measured over time.

The model SSSB is composed of $NaCrO_2$ as the positive electrode, Na-Sn (2:1) as the negative electrode, and Na_3PS_4 as the electrolyte. The positive electrode is mixed into a composite with a weight ratio of 11:16:1 of $NaCrO_2$:Na_3PS_4:VGCF. The battery is fabricated through mechanical pressing; 75 mg of Na_3PS_4 powder is pressed first at 370 MPa, then about

12 mg of the composite $NaCrO_2$ powder is placed on one side of the Na_3PS_4 pellet and pressed at the same pressure, and finally on the opposite side of the Na_3PS_4, an excess of Na-Sn 2:1 alloy (35 mg) is pressed at the same pressure. After securing the cell in a cell holder, the electrical leads were connected to an electrochemical cycler (Landhe). For a rate of C/10, the current density used was 64 μA cm^{-2}.

To incorporate $Na_{2.25}Y_{0.25}Zr_{0.75}Cl_6$ (NYZC0.75) into the model SSSB, NYZC0.75 replaced Na_3PS_4 in the composite cathode (still hand-mixed with the same 11:16:1 ratio). For cells cycled at 40°C, the cell assemblies were placed into a compact box furnace (MTI KSI-1100X) within the Ar-filled glovebox. Current densities ranged from 64 μA cm^{-2} (C/10) to 640 μA cm^{-2} (1C).
After cycling, the cell was disassembled to characterize any material changes.

3.2.2.4 Characterization – X-ray Photoelectron Spectroscopy (XPS)

The powders were adhered onto a small metallic sample stub (Shimadzu) with carbon tape. The metallic stub was secured into a metallic canister and sealed inside the glovebox with clamps.

The metallic canister was placed into a N_2 glovebox that is attached to the XPS tool (Kratos Axis Supra), where the sample can be transferred into the analysis chamber without any exposure to ambient air. All measurements were taken using 15 kV Al Kα radiation at a chamber pressure less than 5 x 10^{-8} torr. For the wide survey scans, a pass energy of 160 eV and a dwell time of 100 ms was used, but for specific element regions, a pass energy of 20 eV, a dwell time of 300 ms, and a step size of 0.05 eV was used. The charge neutralizer was enabled during all the measurements. Data calibration and analysis were conducted using the CasaXPS software, and all region spectra were calibrated using the C 1s peak.

3.3 Results and Discussion

NYZC*x* compounds were experimentally synthesized using stoichiometric amounts of NaCl, YCl_3, and $ZrCl_4$ (see Methods). The parent compound NYC was first synthesized and its XRD pattern and corresponding Rietveld Refinement results are shown in Figure 3.1 and Table 3.1. These results are consistent with previous reports.[98] The room temperature ionic conductivity of NYC was determined to be 9.5 x 10^{-8} S cm^{-1} via electrochemical impedance spectroscopy (EIS) measurements (Figure 3.1b).

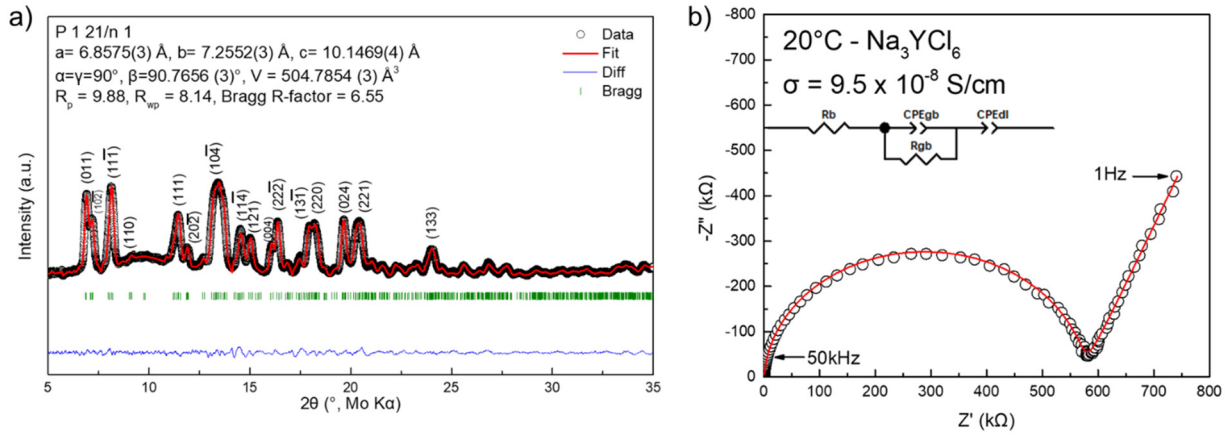

Figure 3.1 a) Rietveld refinement result of the capillary XRD pattern of the as-synthesized Na_3YCl_6. The cell parameters and fitting parameters are in the insets. b) Room temperature Nyquist plot of Na_3YCl_6 and the equivalent circuit used for fitting.

Table 3.1. Rietveld Refinement Parameters; the Atomic Position, B_{iso}, and Occupancy values for Na_3YCl_6.

Na_3YCl_6					
Atom	**x**	**y**	**z**	**B_{iso}**	**SOF**
Y	0	0.5	0	2.05611 (5)	1
Cl1	0.13231(3)	0.56262 (3)	0.24054 (3)	2.30421 (10)	1
Cl2	0.17178 (4)	0.80165 (3)	-0.06645 (3)	1.72623 (12)	1
Cl3	0.32102 (4)	0.32613(4)	-0.07337 (3)	5.06134 (16)	1
Na0	0.5	0	0	2.49819 (16)	1
Na1	0.51056 (5)	0.42455 (3)	0.24624 (5)	3.57594 (14)	1

Since the ionic conductivity of NYC is too low to be practically used in a SSSB, a series of ions (Ti^{4+}, Zr^{4+}, Hf^{4+}, and Ta^{5+}) were evaluated as potential aliovalent dopants for Y^{3+} to increase the concentration of defects and thus, the ionic conductivity of $Na_{3-(z-3)x}Y^{3+}{}_{1-x}M^{z+}{}_xCl_6$.[10,12,99–101] The effect of ionic substitution on the phase stability of NYC is shown in Figure 3.2. Zr^{4+} is predicted to exhibit the lowest dopant formation energies.

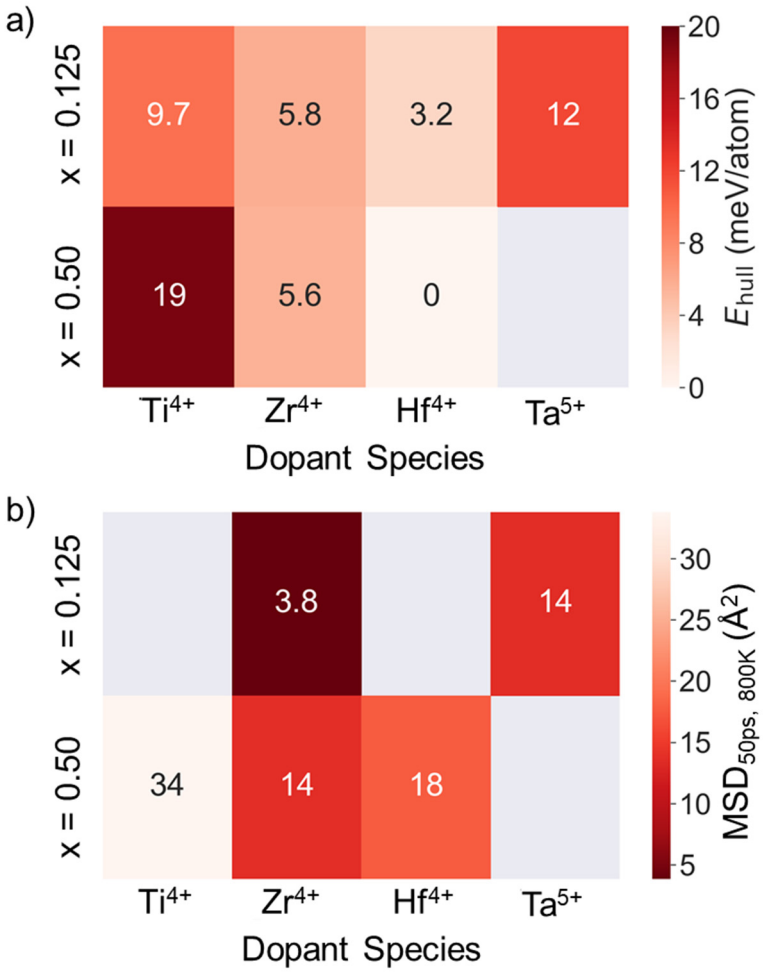

Figure 3.2. a) Calculated energy above hull (E_{hull}) of $Na_{3-(z-3)x}Y_{1-x}M^{z+}{}_xCl_6$ (Where M^{z+} = Ti^{4+}, Zr^{4+}, Hf^{4+} , x = 0.125, 0.50; M^{z+} = Ta^{5+}, x = 0.125). **b**, Mean squared displacement of Na^+ for a 50 ps time scale at 800 K ($MSD_{50ps,800K}$) of $Na_{3-(z-3)x}Y_{1-x}M^{z+}{}_xCl_6$ (where M^{z+} = Zr^{4+}, Ta^{5+}, x = 0.125; M^{z+} = Ti^{4+}, Zr^{4+}, Hf^{4+}, x = 0.50). Gray regions indicate either an unstable compound (due to significant Na^+ loss for Ta^{5+} at x = 0.50) or in the case of MSD screening, preferentially conducted for the higher dopant concentrations for Ti^{4+} and Hf^{4+} (stable at x = 0.50).

With Zr doping, the $P2_1/n$ space group of the parent compound NYC is largely retained (Figure 3.3a) up to x = 0.875, suggesting a solid solution in this compositional range. For $x \geq$ 0.875, additional peaks emerge in the XRD patterns at 2θ = 9.6° and 10.5°, indicating the presence of a second phase. This phase was determined to be crystalline NZC, which has not been reported previously. Rietveld refinement was carried out on NZC after heat treatment and the results are shown in Figure 3.4 and Table 3.2. Furthermore, XPS measurements, shown in

Figure 3.5, indicate the presence of both Zr-Cl and Y-Cl bonds (as seen in the Cl 2p region) and thus the presence of both structural units in the as-prepared NYZC0.5.

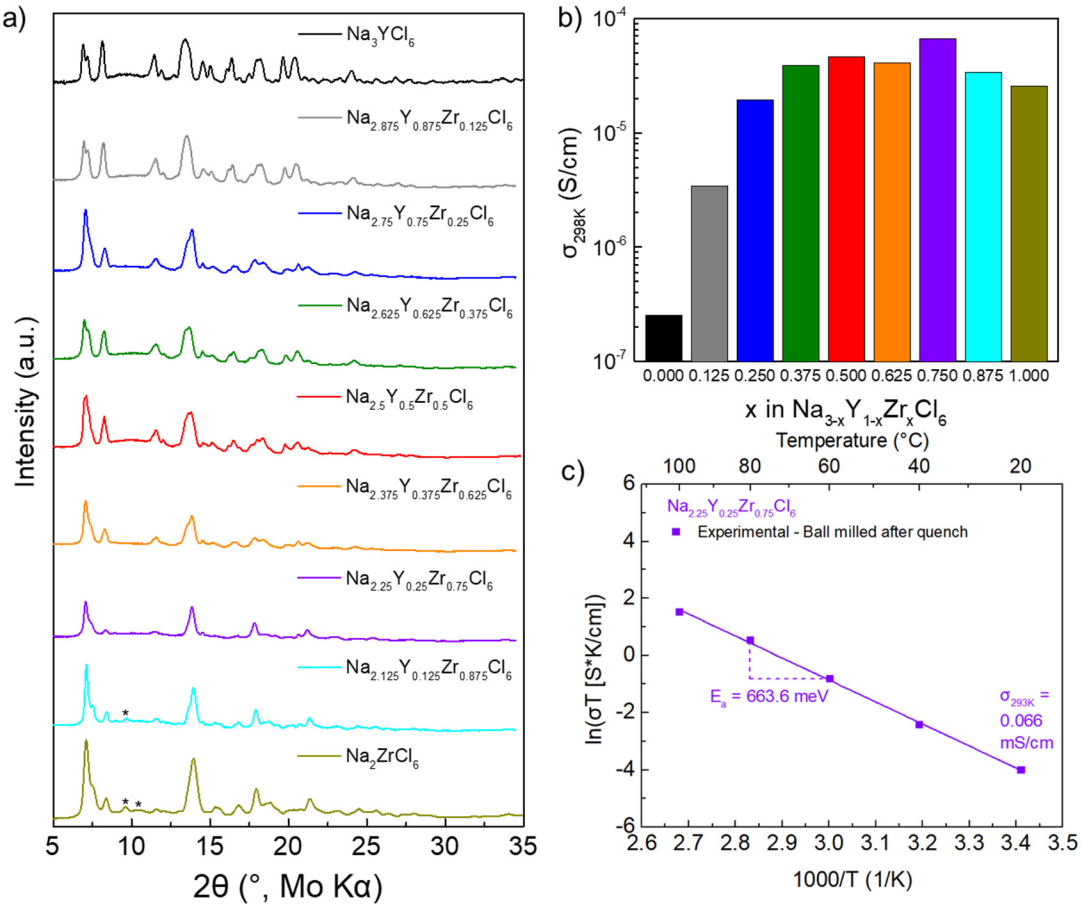

Figure 3.3. a) XRD of the $Na_{3-x}Y_{1-x}Zr_xCl_6$ compositions, obtained in x = 0.125 increments. b) Room temperature conductivity values. c) Arrhenius plot of $Na_{2.25}Y_{0.25}Zr_{0.75}Cl_6$ from experimental measurements.

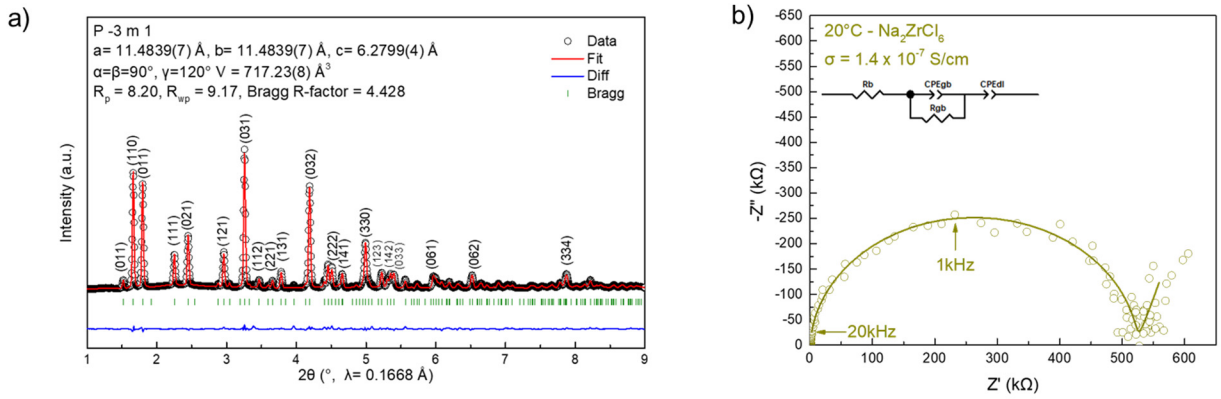

Figure 3.4. a) Rietveld refinement result of the synchrotron XRD data of the post heat-treated Na_2ZrCl_6, in good agreement with the structural relaxation result. The cell parameters and fitting parameters are in the inset. b) Room temperature Nyquist plot and equivalent circuit fit for Na_2ZrCl_6.

Table 3.2. Rietveld Refinement Parameters; the Atomic Position, B_{iso}, and Occupancy values for Na_2ZrCl_6.

Na_2ZrCl_6					
Atom	**x**	**y**	**z**	**B_{iso}**	**SOF**
Zr1	0	0	0	0.04104 (11)	1
Zr2	0.3333	0.6667	0.49422 (1)	3.22545 (12)	1
Na1	0.35545 (4)	0	0	4.64322 (2)	1
Cl1	0.10358 (3)	0.89642 (3)	0.20814 (6)	3.00080 (3)	1
Cl2	0.23114 (5)	0.42455 (5)	0.73893 (6)	3.88311 (5)	1
Cl3	0.43053 (5)	0.56947 (5)	0.24081 (6)	5.19274 (5)	1

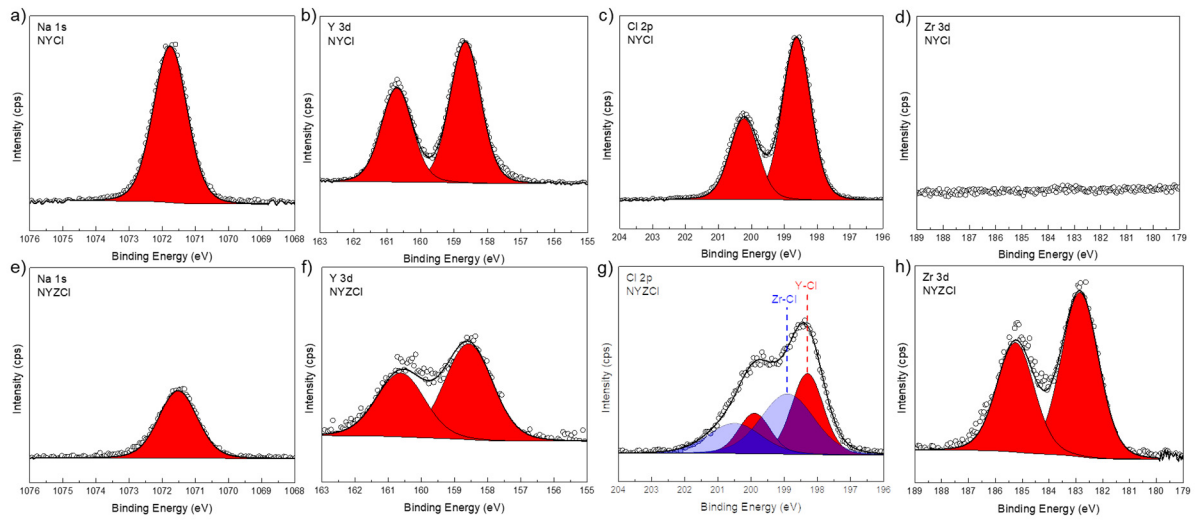

Figure 3.5. XPS of the Na 1s, Y 3d, Cl 2p, and Zr 3d binding energy regions. for **a-d**, Na_3YCl_6 and **e-h**, $Na_{2.5}Y_{0.5}Zr_{0.5}Cl_6$, respectively. For Na_3YCl_6, the Cl 2p binding energy region shows the Y-Cl bond energy signature and thus YCl_6 in the structure. For $Na_{2.5}Y_{0.5}Zr_{0.5}Cl_6$, there is an additional signature from the Zr-

Cl bond as seen in the Cl 2p and Zr 3d binding energy regions, confirming the coexistence of both YCl_6 and $ZrCl_6$ units.[102]

Figure 3.3 b shows the extracted conductivity values (from the respective Nyquist plots in Figure 3.6a), over the entire NYZC*x* compositional range at x = 0.125 increments. The ionic conductivity for $0.375 \leq x < 1$ is in the range of 2.6-6.6 x 10^{-5} S cm^{-1}, with NYZC0.75 exhibiting the highest conductivity of 6.6 x 10^{-5} S cm^{-1} (the corresponding equivalent circuit fitting for NYZC0.75 is shown in Figure 3.6b). Crystalline NZC was found to have a much lower room temperature conductivity of 1.4 x 10^{-7} S/cm (Figure 3.4b), and its presence in the $x \geq 0.875$ compositions explains the observed reduced conductivity. Since NYZC0.75 exhibited the highest conductivity among the compositions, the activation energy was measured (Figure 3.4c) and found to be 663.6 meV. In addition, the electronic conductivity of NYZC0.75 was determined to be 8.89 x 10^{-9} S cm^{-1} via DC polarization (Figure 3.7), i.e., NYZC0.75 is an ionic conductor and an electronic insulator.

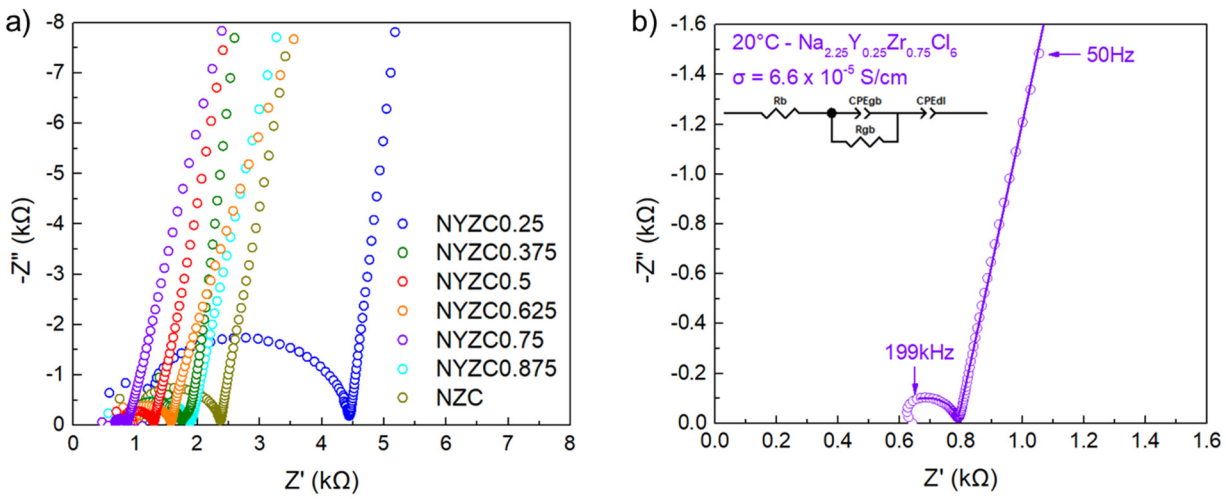

Figure 3.6. a) The Nyquist plots from x = 0.25 to x = 1 are shown for scale. b) Equivalent circuit fit for x = 0.75, the composition with the highest measured ionic conductivity.

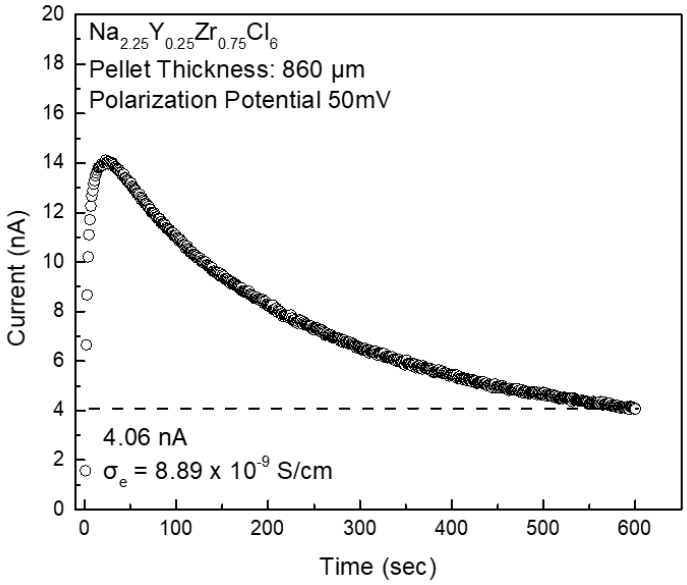

Figure 3.7. DC polarization was conducted on a pellet of $Na_{2.25}Y_{0.25}Zr_{0.75}Cl_6$ to determine its electronic conductivity (8.89 x 10^{-9} S/cm, making it an electronic insulator). The applied potential was 50mV.

Given the high cathodic stability and conductivity of NYZC0.75, cells comprising NYZC0.75 in a composite with the $NaCrO_2$ cathode and Na_3PS_4 as the SE were constructed; a schematic is shown in Figure 3.8a. For comparison, a control cell using Na_3PS_4 alone, without NYZC0.75, was also constructed (Figure 3.9a). At 20°C at a rate of C/10 (Figure 3.8b-c for NYZC0.75 and Figure 3.9b-c for NPS) it is evident that the first cycle Coulombic efficiency (CE) drastically increased in the NYZC0.75 cell (from 71.9% to 97.6%). This observed first cycle CE for the NYZC0.75 cell is the highest among those reported for Na ASSBs that use $NaCrO_2$ as the cathode.[18,57,103,104] We believe that the high cathodic limit of NYZC0.75 protects the Na_3PS_4 SE from oxidation by $NaCrO_2$, and in turn the Na_3PS_4 SE forms a stable passivating interface with the Na-Sn anode.[88] This is consistent with results from symmetric cell experiments carried out using either NYZC*x* or NPS with Na-Sn alloys (Figure 3.10).

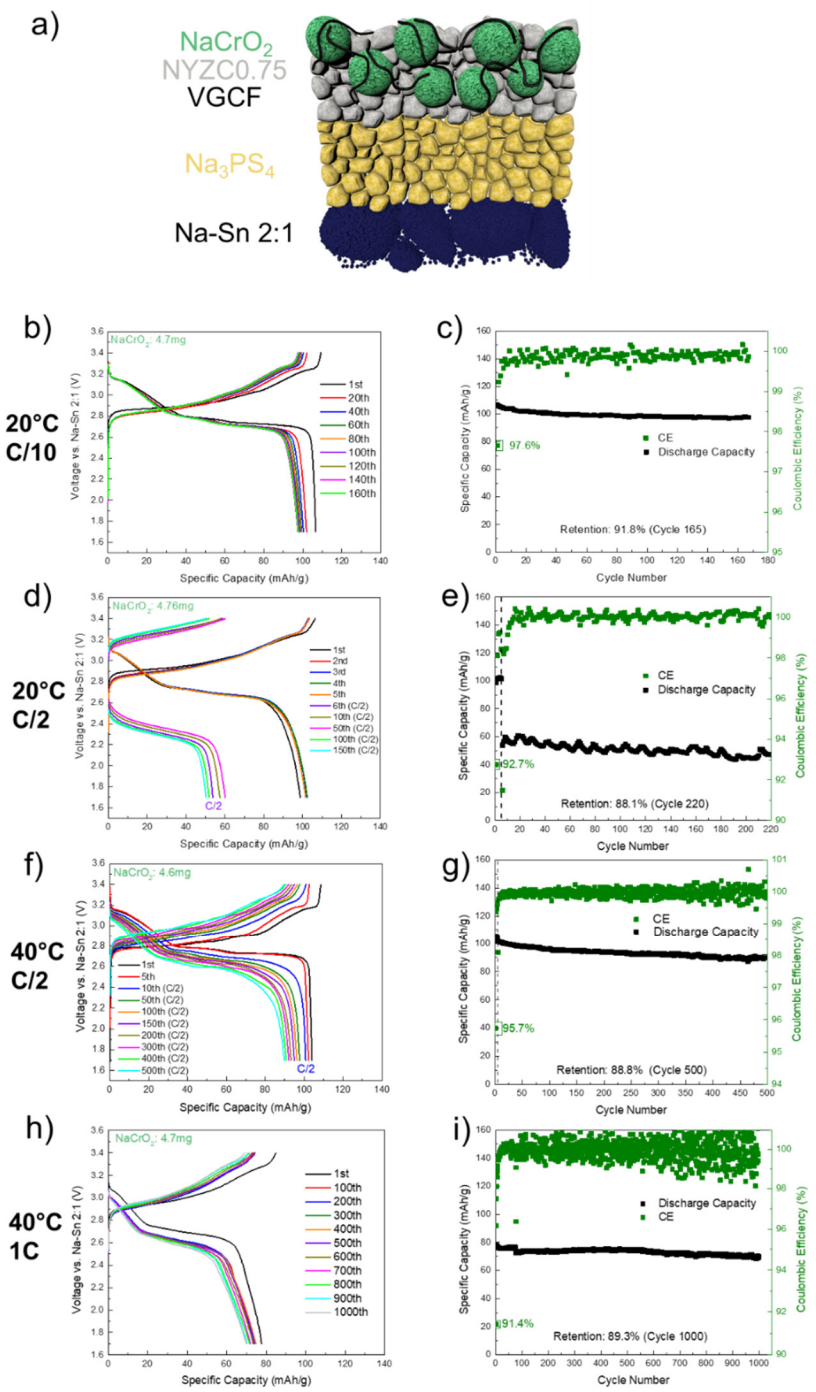

Figure 3.8. a) Cell schematic. Voltage profile and specific capacity as a function of cycle number of this cell configuration, respectively, running at: b-c) 20°C and C/10, d-e) 20°C and C/10 for the first 5 cycles and subsequent cycling at C/2, f-g) 40°C and C/10 for the first 5 cycles and subsequent cycling at C/2, and h-i) 40°C and 1C. In each case, the NYZC0.75 cells exhibit long-term cycling stability, with 89.3% capacity retention at 1000 cycles for the 40°C 1C cell.

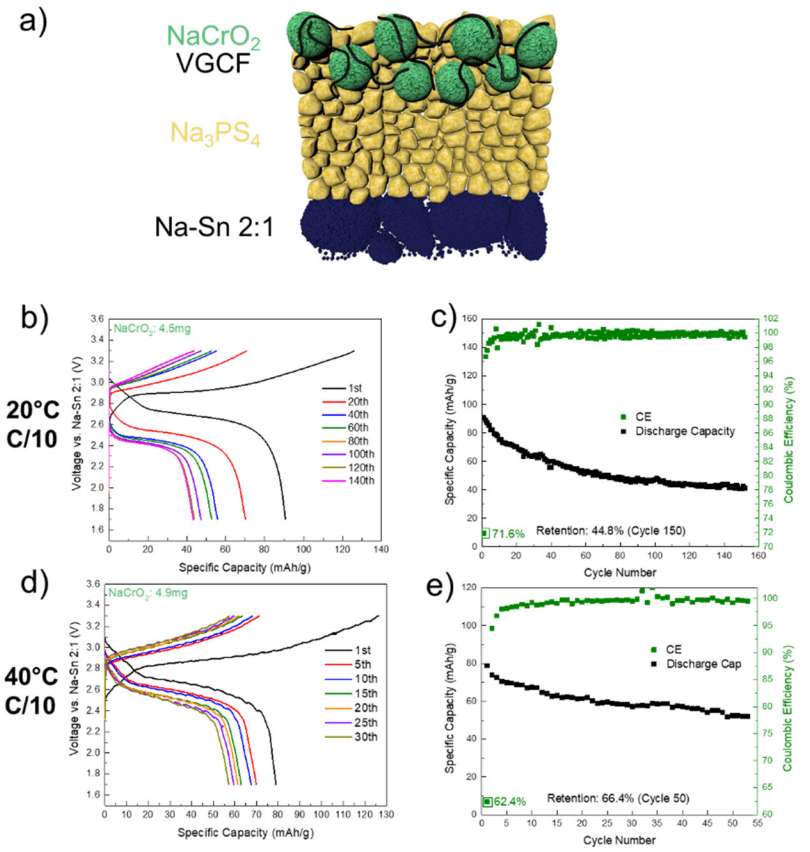

Figure 3.9. a) Cell schematic. Voltage profile and specific capacity as a function of cycle number of this cell configuration, respectively, running at b-c, 20°C and C/10, and d-e, 40°C and C/10. Gradual capacity fade is observed as the capacity retention is 44.8% after 150 cycles (20°C) and 66.4% after 50 cycles (40°C), revealing the instability of NPS when paired with $NaCrO_2$.

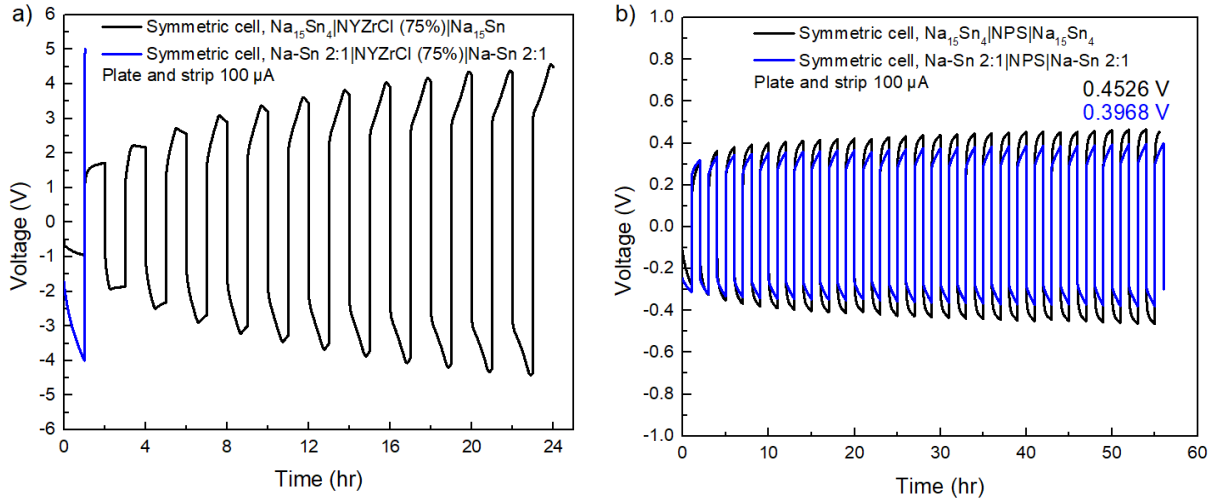

Figure 3.10. a) Symmetric cell plating and stripping of $Na_{2.25}Y_{0.25}Zr_{0.75}Cl_6$ with $Na_{15}Sn_4$ and Na-Sn 2:1 electrodes. b) Symmetric cell plating and stripping of Na_3PS_4 with $Na_{15}Sn_4$ and Na-Sn 2:1 electrodes. High impedance or steady impedance growth is shown for $Na_{2.25}Y_{0.25}Zr_{0.75}Cl_6$ with Na-Sn anodes as opposed to Na_3PS_4; Na_3PS_4 is more stable when paired with Na-Sn, consistent with the EC window calculations.

To study the rate capability of the NYZC0.75 cell configuration, additional cells were constructed and tested at C/2 (after the first 5 cycles at C/10) at both 20°C and 40°C (Figures. 3.8d-e and 3.8f-g, respectively). At 20°C, there is a noticeable drop in capacity (from 101 to 53.7 mAh/g) after switching to a rate of C/2. This is due to several reasons: one, the NPS layer is relatively thick (~800 μm) and the conductivity of NYZC0.75 is in the order of 10^{-5} S/cm. It is important to note that the cyclical behavior in Figure 3.8e is due to temperature variations in the glovebox, as the cell was not inside a temperature-controlled chamber. At 40°C, where the conductivity of NYZC0.75 is in the range of 1-2 x 10^{-4} S/cm, the drop in capacity is negligible (from 104 to 101 mAh/g) when switching to a rate of C/2. For this particular SSSB, the average CE is 99.96%, which yields a capacity retention of 88% after 500 cycles. Furthermore, another NYZC0.75 SSSB was constructed and cycled at 40°C and at a rate of 1C (Figures 3.8h-i). This cell can cycle over 1000 cycles with a capacity retention of 89.3%, further highlighting the superior stability of NYZC0.75 when paired with $NaCrO_2$. To date, this is the highest capacity retention obtained for a SSSB, and Figure 3.11 compares cycling performance metrics (gravimetric energy density per active mass, cycle life, capacity retention, rate, and cathode type) across various SSSB reports.

In addition, another NPS control cell was also cycled 40°C and C/10 (Figure 3.9d-e); the first cycle CE decreased from 71.9% (at 20°C) to 62.4%, showing that NPS oxidation is exacerbated at 40°C. This result contrasts with the demonstrated superior electrochemical stability of NYZC0.75 at 40°C and high rates.

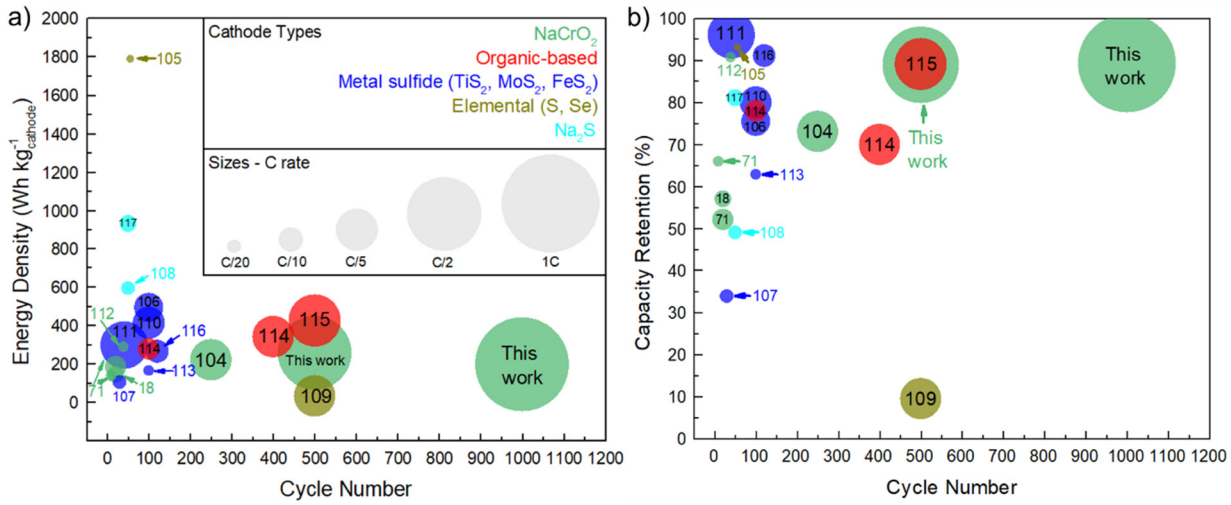

Figure 3.11. a) Gravimetric energy density (per mass of active material) plotted as a function of cycle number.[18,71,104–117] b) Capacity retention as a function of cycle number.[18,71,104–117]. The cycling performance comparison highlights the compatibility and stability of the $NaCrO_2$ + $Na_{2.25}Y_{0.25}Zr_{0.75}Cl_6$ + VGCF composite cathode.

To characterize the chemical environments in NPS and NYZC0.75 components after cycling, the SSSBs were disassembled to recover the composite cathodes and XPS measurements were conducted. Figure 3.12 compares the S 2p and P 2p binding energy regions of pristine NPS and the cycled NPS-containing composite cathode. Consistent with previous reports, when paired with an oxide cathode, NPS oxidizes to form elemental sulfur, other P_2S_x compounds, and possibly compounds containing P-O bonds.[96,118,119] Figure 3.13 shows the Zr 3d and Y 3d bonds of pristine versus cycled NYZC0.75. Even with cells cycled at elevated temperatures or high rates, the Zr-Cl and Y-Cl bonds are retained in the composite cathode, confirming the electrochemical stability of NYZC0.75 when used with $NaCrO_2$.

To evaluate the chemical stability, temperature-dependent XRD patterns were collected for 1:1 mixtures of NPS:$NaCrO_2$ and NYZC0.75:$NaCrO_2$ (Figure 3.14). In both the cases, no new additional peaks appeared, indicating no chemical reaction, even at temperatures as high as 220°C. This is in accordance with Table 3.3, where the reaction energy with $NaCrO_2$ is low for both NPS (-0.18 eV/atom) and NYZC0.75 (-0.14 eV/atom). Thus, the observed superior cycling stability of NYZC0.75 arises from its intrinsic chemical stability in combination with its wide

electrochemical window, whereas NPS is electrochemically unstable in presence of high voltage oxide cathode and undergoes oxidative decomposition during charging.

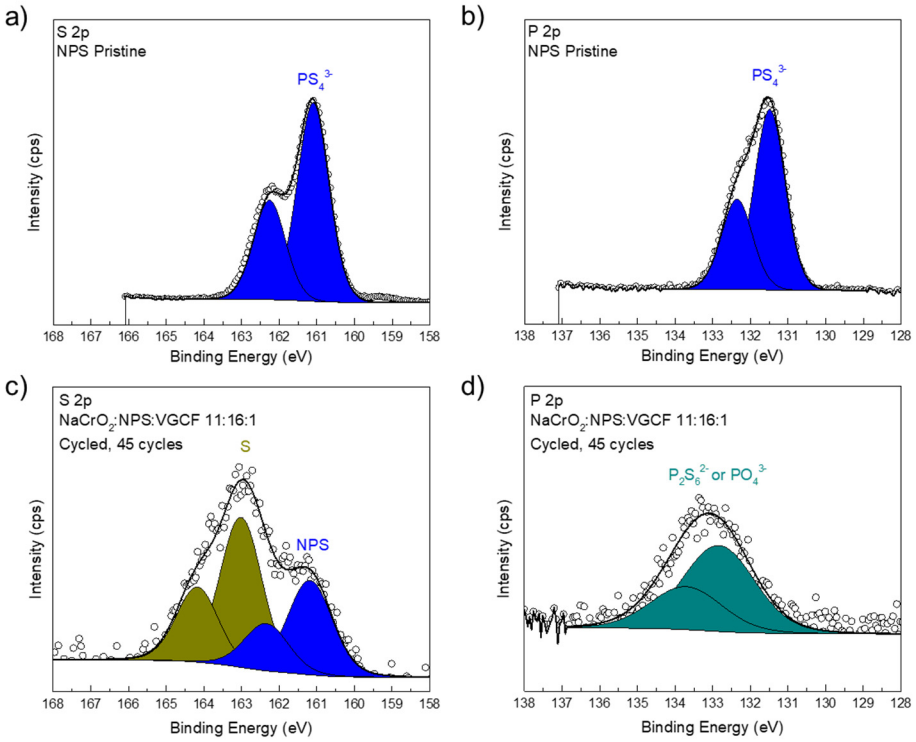

Figure 3.12. a) S 2p and b) P 2p binding energy regions of pristine Na_3PS_4. c) S 2p and d) P 2p binding energy regions of the composite cathode of the cycled room temperature NPS-only cell.

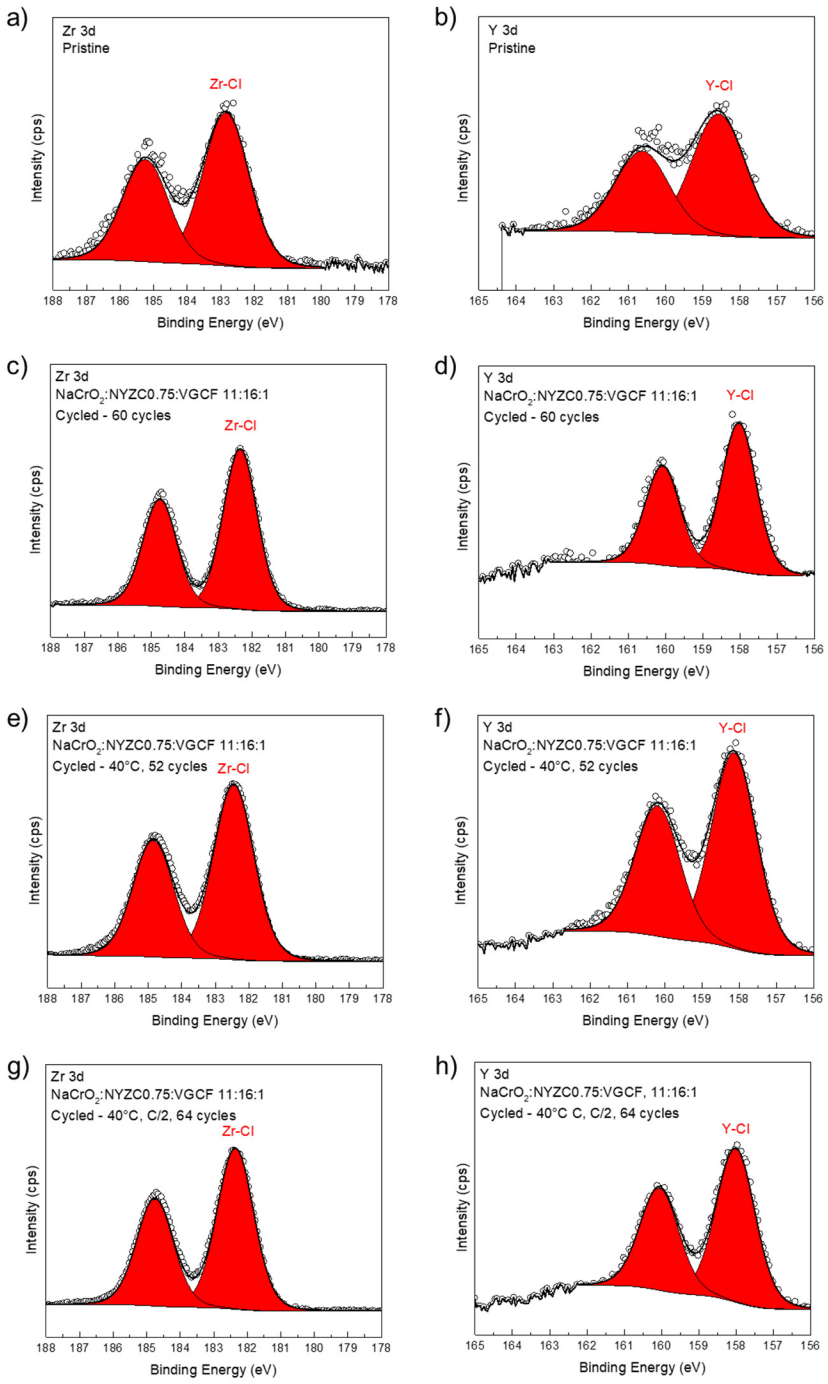

Figure 3.13. XPS Zr 3d and Y 3d binding energy regions, respectively, for a-b) Pristine $Na_{2.25}Y_{0.25}Zr_{0.75}Cl_6$, and the $NaCrO_2$:$Na_{2.25}Y_{0.25}Zr_{0.75}Cl_6$:VGCF composite cathode taken from cells cycled at: c-d) Room temperature, e-f) 40°C, and g-h) 40°C at a rate of C/2. No extra peaks or significant shifts in the Zr 3d or Y 3d peaks are observed so the Zr-Cl and Y-Cl bonds are maintained throughout cycling.

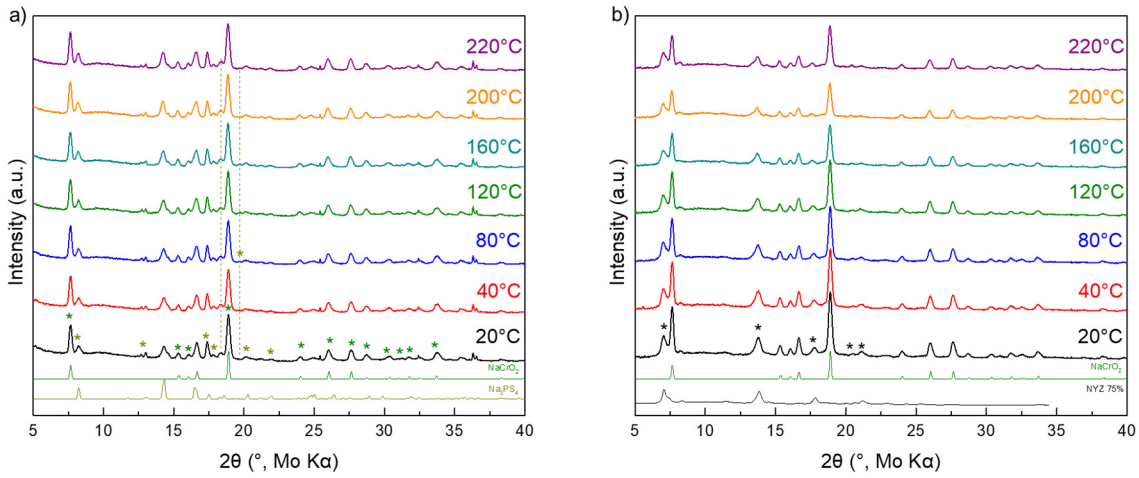

Figure 3.14. Temperature-dependent XRD of a) 1:1 NPS:$NaCrO_2$ mixture and b) 1:1 NYZC0.75:$NaCrO_2$ mixture. No extra peaks were seen in either case, consistent with the low reaction energy from computational results. The low initial CE and the capacity fade of the Na_3PS_4-only cell thus comes from the electrochemical oxidation of Na_3PS_4 at high voltages.

Table 3.3. Computed reaction Energies (with $NaCrO_2$ and Na metal) and the electrochemical windows of NYC, $Na_{2.25}Y_{0.25}Zr_{0.75}Cl_6$, and Na_3PS_4.

System	Reaction energy w/ $NaCrO_2$ (eV/atom)	Reaction energy w/Na (eV/atom)	EC window (V)
Na_3YCl_6	-0.11	-0.13	0.6-3.8
$Na_{2.25}Y_{0.25}Zr_{0.75}Cl_6$	-0.14	-0.34	1.5-3.8
Ref: c-Na_3PS_4	-0.18	-0.46	1.2-2.5

3.4 Conclusion

In this work, we reported on aliovalent substitution in the halide-based ionic crystal Na_3YCl_6, which leads to phases with enhanced Na^+ conduction due to the presence of an interconnected network of Na^+ diffusion channels (specifically, substituting Y^{3+} in Na_3YCl_6 with Zr^{4+} to form $Na_{3-x}Y_{1-x}Zr_xCl_6$). Zr^{4+} substitution was found to increase the volume of the unit cell, which in turn enables polyanion rotation. The synergy between polyanionic rotation and increase in the effective mobile carrier concentration leads to a significant increase in the Na^+ diffusivity upon Zr incorporation, which is absent in the parent Na_3YCl_6 compound. This was confirmed experimentally by an increase in the ionic conductivity by two orders of magnitude upon Zr

substitution. Furthermore, the wide oxidative electrochemical window (up to 3.8 V) was retained after substitution, which proved to be beneficial when paired with a $NaCrO_2$ cathode in a model SSSB. In this configuration, no electrochemical decomposition was observed, in contrast with a cell comprising Na_3PS_4 in the cathode composite, as revealed by XPS. At 40°C and a rate of 1C, the cell containing $Na_{2.25}Y_{0.25}Zr_{0.75}Cl_6$ was able to cycle over 1000 cycles with a capacity retention of 89.3%, the highest cycle life for a SSSB to date. Thus, further exploration of halide-based materials, especially in SSSBs, is a worthy area of continued investigation. This methodology of coupling computational and experimental evaluation, verification, and testing of material properties is an effective and necessary strategy toward finding compatible, long-lasting, and high-performing SSSB chemistries.

Chapter 3, in part, has been submitted for publication as “A Stable Cathode-Solid Electrolyte Composite for Long-Cycle-Life, High Voltage Solid-State Sodium-ion Batteries” in Nature Energy. Wu, E. A.*, Banerjee, S.*, Tang, H.*, Richardson, P. M., Doux, J.-M., Qi, J., Zhu, Z., Grenier, A., Li, Y., Zhao, E., Deysher, G., Nguyen, H., Stephens, R., Verbist, G., Chapman, K. W., Clément, R. J., Banerjee, A., Meng, Y. S., and Ong, S. P. The dissertation author was one of the three co-first authors for this study. The dissertation author carried out all the experiments and electrochemical testing herein.

Chapter 4. A Facile, Dry-Processed Lithium Borate-Based Cathode Coating for Improved All-Solid-State Battery Performance

Sulfide-based solid electrolytes are known to have narrow electrochemical windows which limit their practical use in all-solid-state batteries (ASSBs). Specifically, when paired with a high-voltage transition metal oxide (TMO) cathode, the electrolyte will typically undergo unwanted degradation via chemical reactions or electrochemical oxidation, especially upon charging to voltages beyond the electrochemical stability window of the electrolyte. To mitigate these undesired reactions, thin (< 10 nm), conformal, ionically-conducting, and electronically-insulating oxide-based protective coating layers have been applied on the cathode, typically via a solution process. In this work, a lithium borate-based (LBO) coating, prepared instead with a dry coating process, was shown to have the same beneficial properties. As evidenced by electrochemical characterization, the developed LBO coating shows good cycling performance and even performs better than the $LiNbO_3$ coating commonly used in the literature. This new solvent-free coating method can thus be used to fabricate longer-lasting ASSBs.

4.1 Introduction

All-solid-state batteries (ASSBs) have gained much research interest due to their potential for higher energy density, the possibility of using metallic anodes, and improved safety since the solid-state electrolyte (SSE) is non-flammable and non-corrosive.[120–122] However, many of the recently well-studied SSEs are sulfide-based; while sulfide SSEs have an advantage over oxides in terms of ionic conductivity and ease of processability[123–125], one main drawback is higher chemical reactivity and lower electrochemical stability, especially when used in conjunction with oxide cathode materials, as sulfides will inherently electrochemically oxidize once subjected to higher voltages during charging.[86,126]

One common strategy to mitigate unwanted reactions between the SSE and the oxide cathode is the implementation of a chemically inert, Li-ion conducting, and electronically-

insulating coating on the cathode particles. Such a coating needs to have a much lower reactivity with the SSE (compared to the cathode) and must also be thin enough (~5 nm) to not drastically raise the overall impedance of the ASSB. For this purpose, cathode coatings such as $LiNbO_3$ (LNO), $LiAlO_2$, $LiTaO_3$, $Li_4Ti_5O_{12}$ (LTO), lithium borate (LBO), and others have been explored.[16,30,86,127–130] However, it is important to note that many of these cathode coatings are prepared via a solvent-based solution process. In this work, a new dry coating process for LBO was investigated on the cathode $LiNi_{0.8}Co_{0.1}Mn_{0.1}O_2$ (NCM811) The electrochemical performance of ASSBs, prepared using Li_6PS_5Cl (LPSCl) as the electrolyte and LiIn alloy as the anode, showed that the LBO coating improved the first cycle discharge capacity from 40 mAh/g to 126 mAh/g when compared to a similar cell with bare NCM811. Other characterization methods, such as scanning transmission electron microscopy (STEM) with electron energy loss spectroscopy (EELS), revealed a ~1-2 nm-thick conformal LBO coating and X-ray diffraction (XRD) demonstrated that chemical reactions between LPSCl and NCM811 were mitigated by the coating. This dry process opens a new avenue to fabricate protective cathode coatings to enable longer-lasting ASSBs.

4.2 Methods

4.2.1 Materials Preparation

As sulfide-based materials are sensitive to air and moisture (decomposing to form toxic gases such as H_2S), all synthesis and characterization steps were done within an argon-filled glovebox (MBraun MB 200B, H_2O < 0.5 ppm, O_2 < 5.0 ppm) unless otherwise stated.

Commercial LPSCl was obtained from NEI Corporation and used as received. Commercial, bare $LiNi_{0.8}Co_{0.1}Mn_{0.1}O_2$ (NCM811) was obtained from LG Chem. The dry coating process was conducted as follows: Boric acid (>99.5%, Sigma Aldrich) was mixed with the uncoated NCM811 cathode in an agate mortar and pestle for 5 minutes according to the predetermined final boron parts per million (ppm), hereby designated as: LBO B1 (875 ppm), LBO B2 (1800 ppm), and LBO

B3 (3500 ppm). The mixture was subsequently heated at 300°C for 5 hours under ambient conditions to produce the LBO-coated NCM811.

To prepare the solution-process $LiNbO_3$ (LNO) coating, stoichiometric amounts of lithium ethoxide (>95%, Sigma Aldrich) and niobium ethoxide (>99.95%, Sigma Aldrich) were added to NCM811 before dispersing in anhydrous ethanol. The solution was then stirred for 1 hour and dried under vacuum, before heating at 450°C for 1 hour under ambient conditions to produce 2 wt% LNO-coated NCM811 powders.

To prepare the composite cathodes, LPSCl was mixed with the LBO/LNO-coated NCM811 in an agate mortar and pestle (using either a 60:40 weight ratio of LPSCl:cathode without carbon, or a 66:33:1 weight ratio of LPSCl:cathode:carbon) for 5 minutes. To prepare the $Li_{0.5}In$ anode, stoichiometric amounts of stabilized lithium metal powder (FMC Lithium) and indium powder (>99.99%, Sigma Aldrich) were mixed in a glass vial using a vortex mixer for about 5 minutes.

4.2.2 Cell Fabrication and Electrochemical Characterization

To prepare the cells, LPSCl powder was pressed at 370 MPa in a 10 mm polyether ether ketone (PEEK) die using two titanium plungers. Subsequently, 10 mg of the as-prepared cathode composite was added on one side of the LPSCl pellet and pressed at 370 MPa, followed by the application of 40 mg of LiIn on the other side of the electrolyte pellet and pressing at 120 MPa. The cell configuration was secured into a cell holder and connected to a Landhe CT2001 Battery cycler and analyzed with the Land v7.3 software. All cells were cycled at room temperature, inside the Ar glovebox, at 2.5-4.3 V vs. Li/Li^+. For the rate studies, the first charge was done at 0.1C, while the subsequent charging steps were done at 0.5C. All the specific capacities mentioned in this work were calculated based on the electrode active material amount. Electrochemical impedance spectroscopy (EIS) was performed with a Solartron 1260 impedance analyzer for assembled half cells. An applied AC potential of 30 mV over a frequency range from 1 MHz to 0.1 Hz was used for the EIS measurement.

4.2.3 Characterization

STEM-EELS was performed on a JEOL JEM-ARM300CF at 300 kV, equipped with double correctors. EELS spectra were acquired from a square area of ~2 x 2 nm near the surface layer with an acquisition time of 0.01 s. To minimize possible electron beam irradiation effects, EELS spectra presented in this work were acquired from areas without pre-beam irradiation.

XRD was carried out by loading the powder sample into a 0.5mm Boron-rich glass capillary tube (Charles Supper). The sample was flame-sealed to ensure no ambient air contamination. The samples were measured on a Bruker Kappa goniometer equipped with a Bruker Vantec 500 detector. The sample was placed in the Bragg−Brentano θ−θ configuration and the measurement was carried out using Mo Kα radiation.

4.3 Results and Discussion

The schematic of the dry coating process is shown in Figure 4.1. As detailed in the experimental part, the boron concentrations used in this study were LBO B1 (875 ppm), LBO B2 (1800 ppm), and LBO B3 (3500 ppm). To show that the surface impurities were removed by the dry coating process via reacting with boric acid, STEM imaging and EELS were performed on both the bare and LBO-coated NCM811 and the data are shown in Figure 4.2.

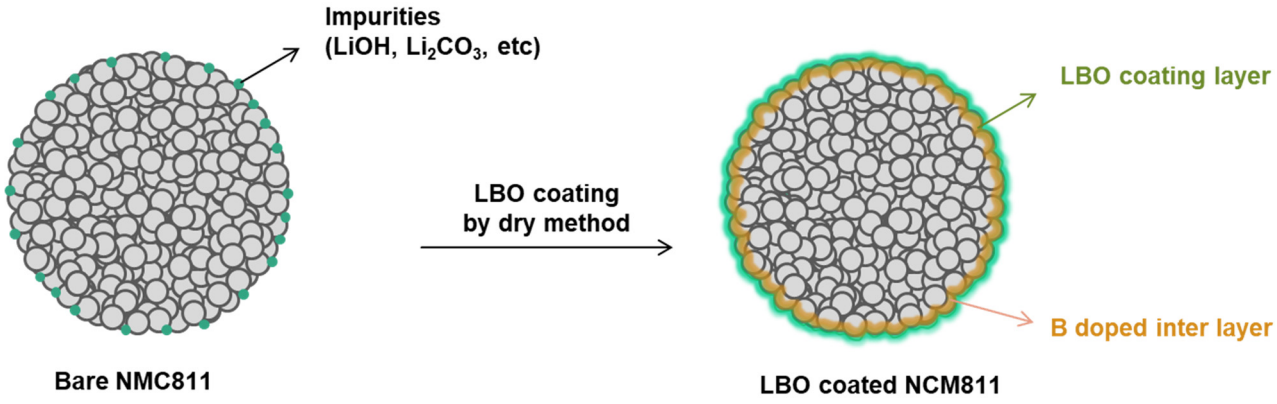

Figure 4.1. Schematic of the LBO coating process on NCM811 cathode particles through the simple dry coating method. Li-containing surface impurities are consumed during the coating process.

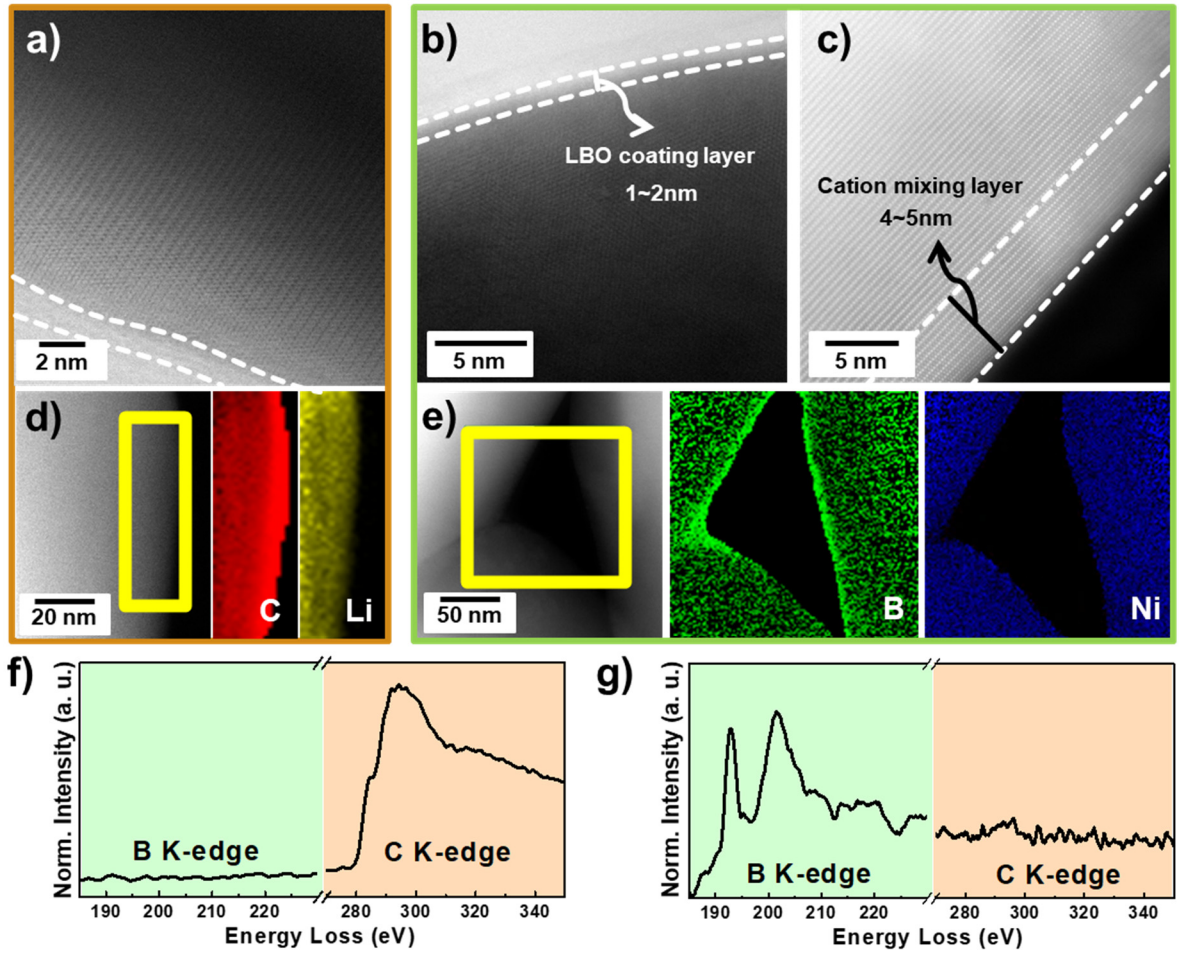

Figure 4.2. HAADF-STEM images of a) Bare NCM811, (b) LBO B2-coated NCM, and (c) Boron-doped interlayer. STEM-EELS elemental mapping of: (d) bare NCM at C K-edges and Li K-edges, (e) LBO B2-NCM for B K-edges and Ni L-edges. EELS spectra at the surface regions of: (f) bare NCM and (g) LBO B2-NCM.

From the STEM images and STEM-EELS mapping of the bare NCM811 (Figures 4.2d and 4.2f), there is a layer of carbon on the surface of the NCM811 particles that comes from surface species such as Li_2CO_3. The LBO-coated NCM EELS spectrum (Figure 4.2g) does not exhibit a signal from C, but only signal from B. This is an indication that Li_2CO_3 is consumed during the coating process to ultimately form the LBO coating on the cathode material. Similar results were obtained with the LBO B3 coating and the results are shown in Figure 4.3. STEM images and intensity plots along the surface of the coated NCM particle (Figure 4.4, for both LBO B2 and LBO B3) show the presence of cation mixing, i.e. TM diffusing beyond the LBO coating. This cation mixing layer is 4-5 nm in thickness for LBO B2 (Figure 4.2c) but 10-12 nm for LBO B3;

such an increased thickness could be potentially detrimental to cell performance as the resistance would increase. For this reason, further increases in the boron content were not considered.

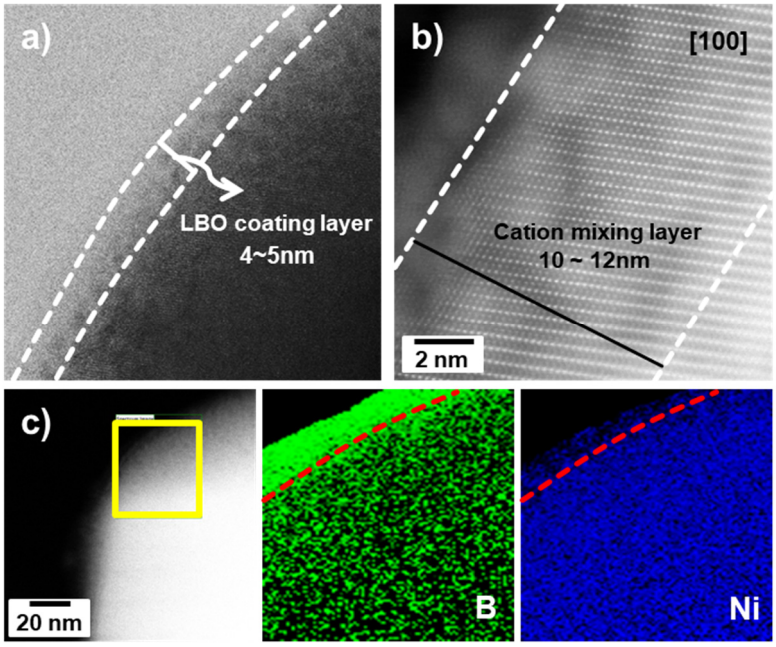

Figure 4.3. HAADF-STEM images of a) LBO B3-coated NCM811, b) The boron-doped interlayer within the LBO B3-coated NCM811 surface. c) STEM-EELS elemental mapping of the LBO B3-coated NCM811 for the B K-edge (green) and the Ni L-edge (blue).

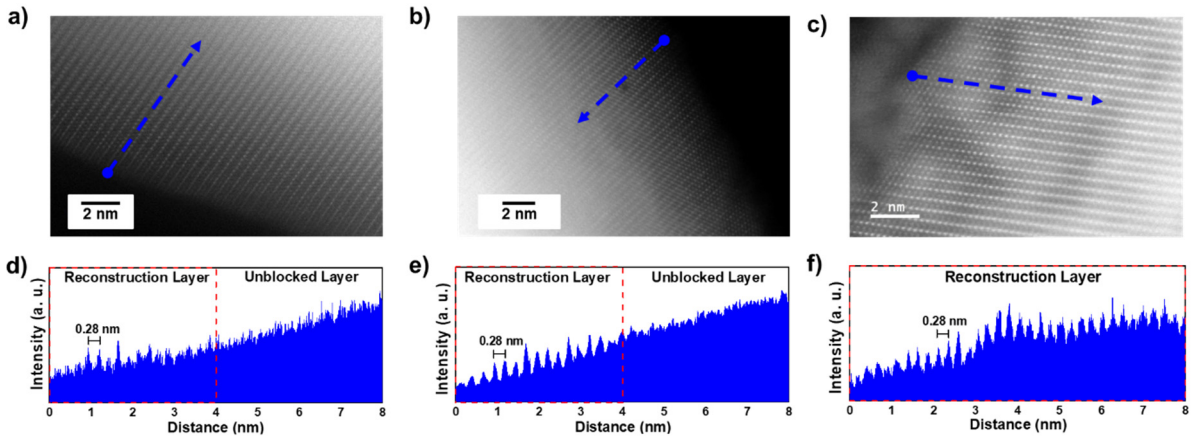

Figure 4.4. HAADF-STEM images of a) Bare NCM, b) LBO B2-coated NCM, and c) LBO B3-coated NCM. Intensity plots (along the blue dashed line) for d) bare NCM, e) LBO B2-coated NCM, and f) LBO B3-coated NCM.

As there is a wide variety of lithium borate compounds, EELS spectra were taken to deduce which specific borate species was synthesized via the coating process (Figure 4.5). LBO B2 most closely matches with the spectra from $Li_2B_4O_7$ and $LiBO_2$, while for LBO B3, a peak shift

is observed (due to the increasing B content during the coating process). Nevertheless, since boron is a light element and many LBO compounds yield similar spectra, it is challenging to narrow down the exact species present.

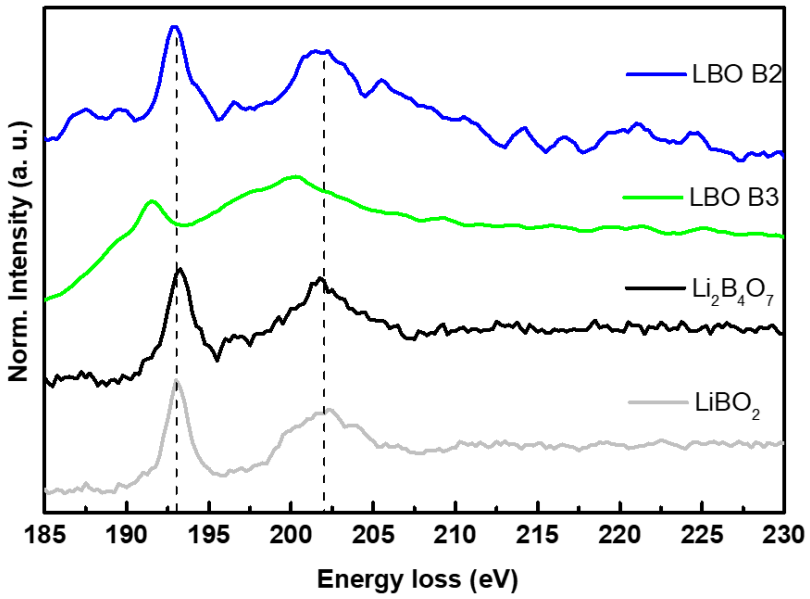

Figure 4.5. EELS spectra for LBO B2-coated NCM, LBO B3-coated NCM, $LiBO_2$, and $Li_2B_4O_7$ (latter two displayed for reference).

To test its electrochemical performance, LBO-coated NCM811 was used in an ASSB configuration that contains LiIn as the anode and LPSCl as the SSE. Figure 4.6 shows the first cycle charge-discharge voltage profile, rate capability, capacity retention, and EIS of the full cells. From the data, the LBO-coated NCM811 outperformed bare NCM811 in all instances, and LBO B2 was shown to have the highest capacity among the three concentrations tested, regardless of the C rate (Figures 4.6b and 4.7). The lower capacity of LBO B1 can be attributed to a coating that is too thin, increasing the chances of incomplete coverage, so not all unwanted reactions are mitigated. As for LBO B3, the lower capacity compared to LBO B2 can be attributed to the significantly thicker coating layer, which would increase charge transfer resistance in the cell. EIS of the bare and LBO B2-coated cells are shown in Figure 4.6d; significant impedance growth after 20 cycles is observed for the bare NCM811 cell, indicative of unwanted chemical reactions that result in resistive CEI products unfavorable for cell performance. There is still impedance growth

in the LBO B2 cell (due to unavoidable LPSCl oxidation)[118] but it is comparatively mitigated. To verify that the performance degradation of the bare NCM811 and LPSCl is from a chemical reaction, air-sensitive capillary XRD was conducted and the data are shown in Figure 4.8. It is clear that LPSCl has degraded when mixed with the bare cathode but remained intact when mixed with LBO B2. Thus, unwanted chemical reactions are prevented by the coating.

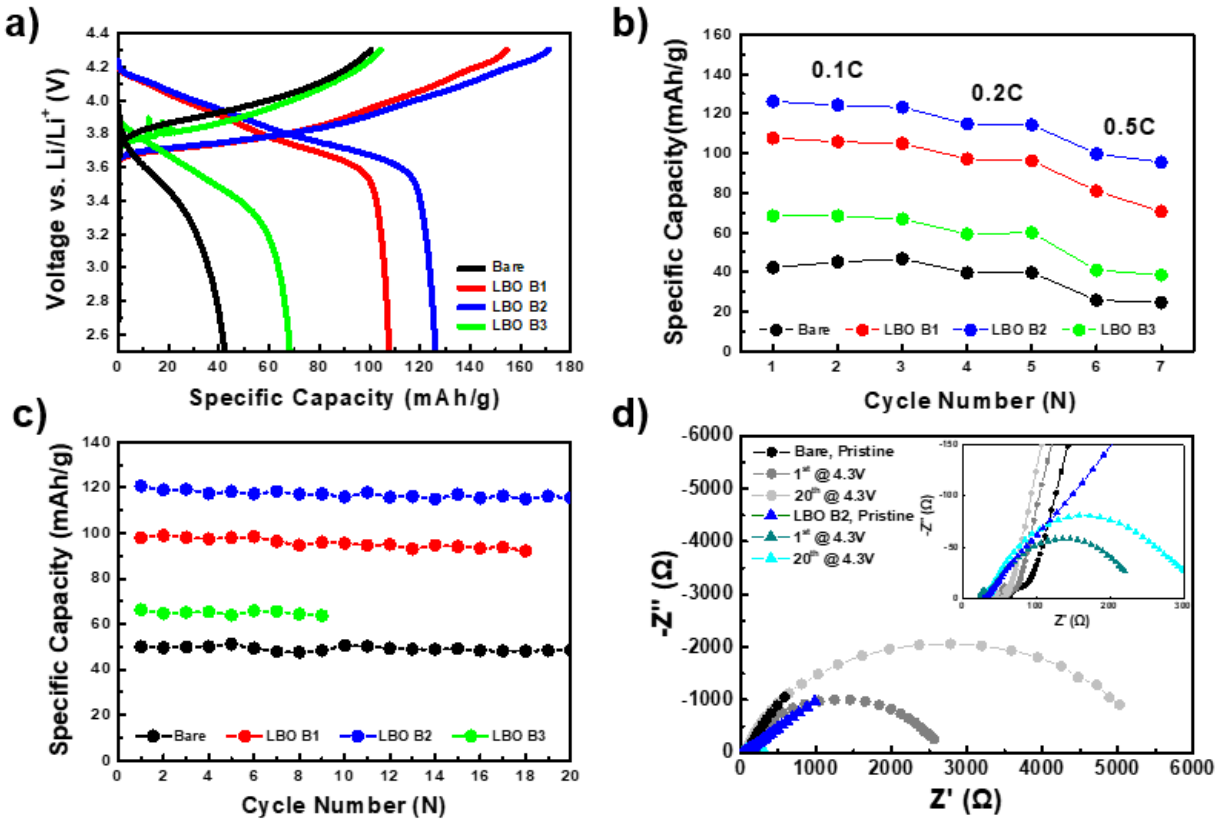

Figure 4.6 (a) Charge-discharge voltage profiles, (b) Rate capability, and (c) Cycle performance at 0.1C of bare and LBO-coated NCM811. (d) Nyquist plots of bare and LBO B2-coated NCM811 before and after 1 and 20th cycles. The cathode composites were prepared with a 60:40 weight ratio of NCM:SSE.

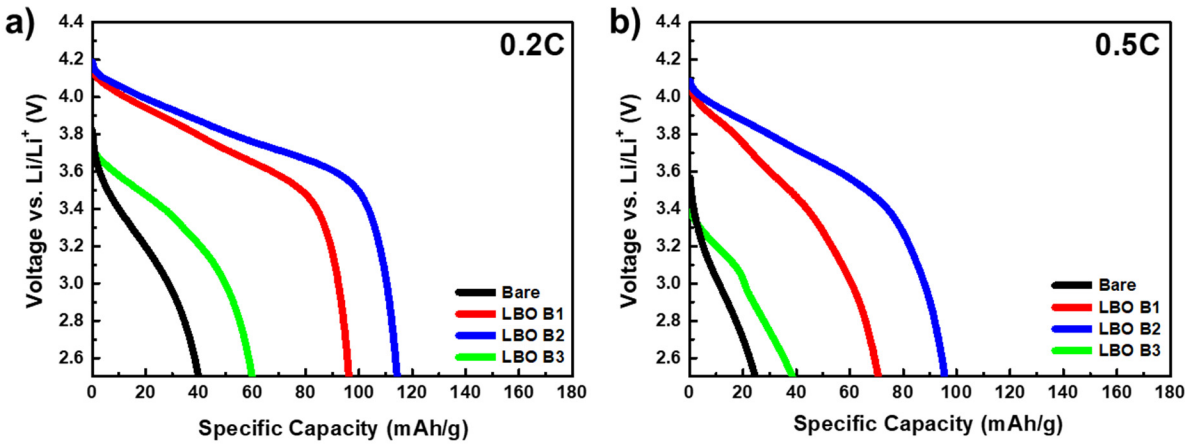

Figure 4.7. First cycle discharge voltage profiles of bare and LBO-coated NCM with different boron compositions at a) 0.2C and b) 0.5C.

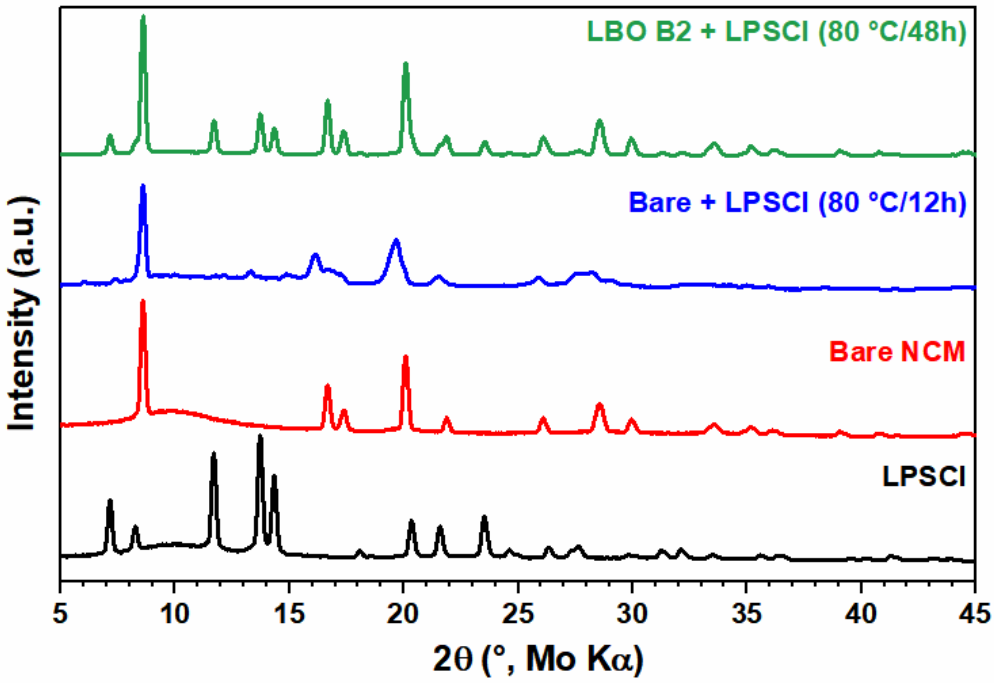

Figure 4.8. X-ray diffraction pattern of LPSCl, bare NCM, Bare NCM + LPSCl mixture (after 12 hours at 80°C) and LBO B2-coated NCM + LPSCl (after 48h at 80°C).

It is important to note that by using more active material and adding conductive additive (66:33:1 NCM:LPSCl:C weight ratio), the initial discharge capacity further increased from 124 to 160 mAh/g (Figure 4.9). These initial results are promising and suggest that continued optimization of the cell setup would be even more beneficial for cycling performance.

Furthermore, a comparison between the commonly used, solution-processed LNO coating and the dry-coated LBO B2 NCM811 was conducted and shown in Figure 4.10, with longer-term cycling in Figure 4.11, which shows the superior cycling performance of LBO B2 compared with LNO. The dry-processed LBO thus shows great promise as a coating material for long-lasting Li ASSBs.

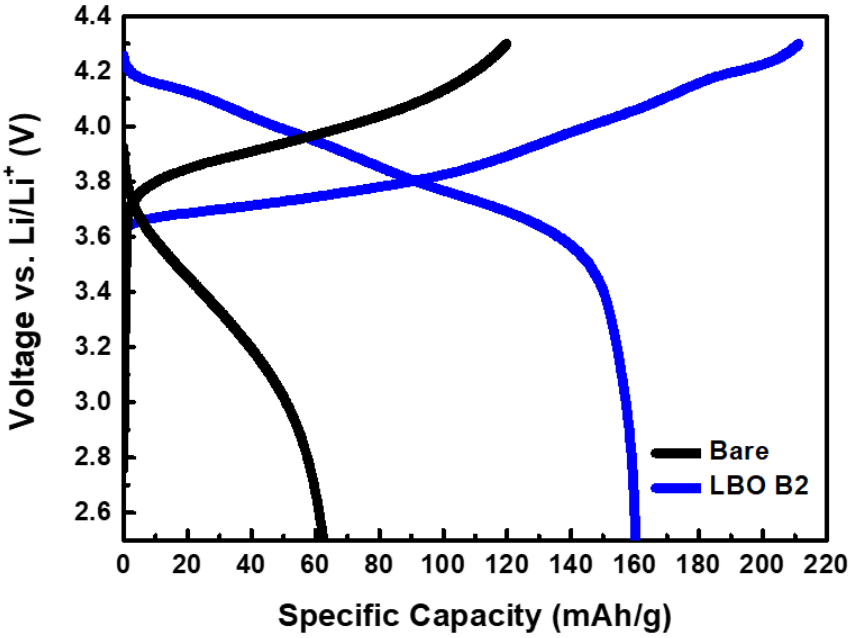

Figure 4.9. First cycle charge-discharge voltage profiles for bare and LBO B2-coated NCM811. The cathode composite is composed of NCM:LPSCl:carbon in a 66:33:1 ratio.

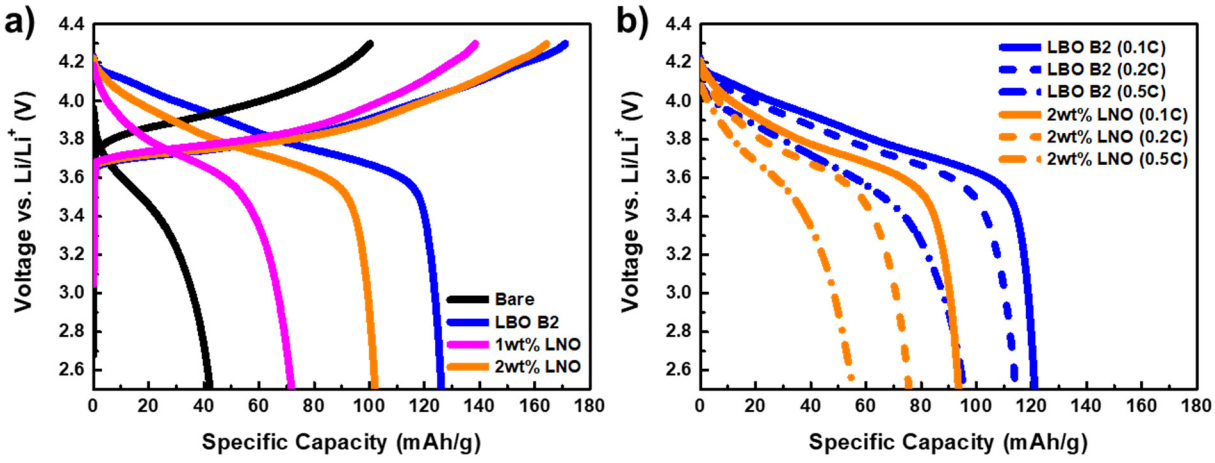

Figure 4.10. Comparison between bare, LBO B2 and LNO coating at 1 wt% and 2 wt%: a) Charge-discharge voltage profiles. b) Discharge voltage profile at various C rates.

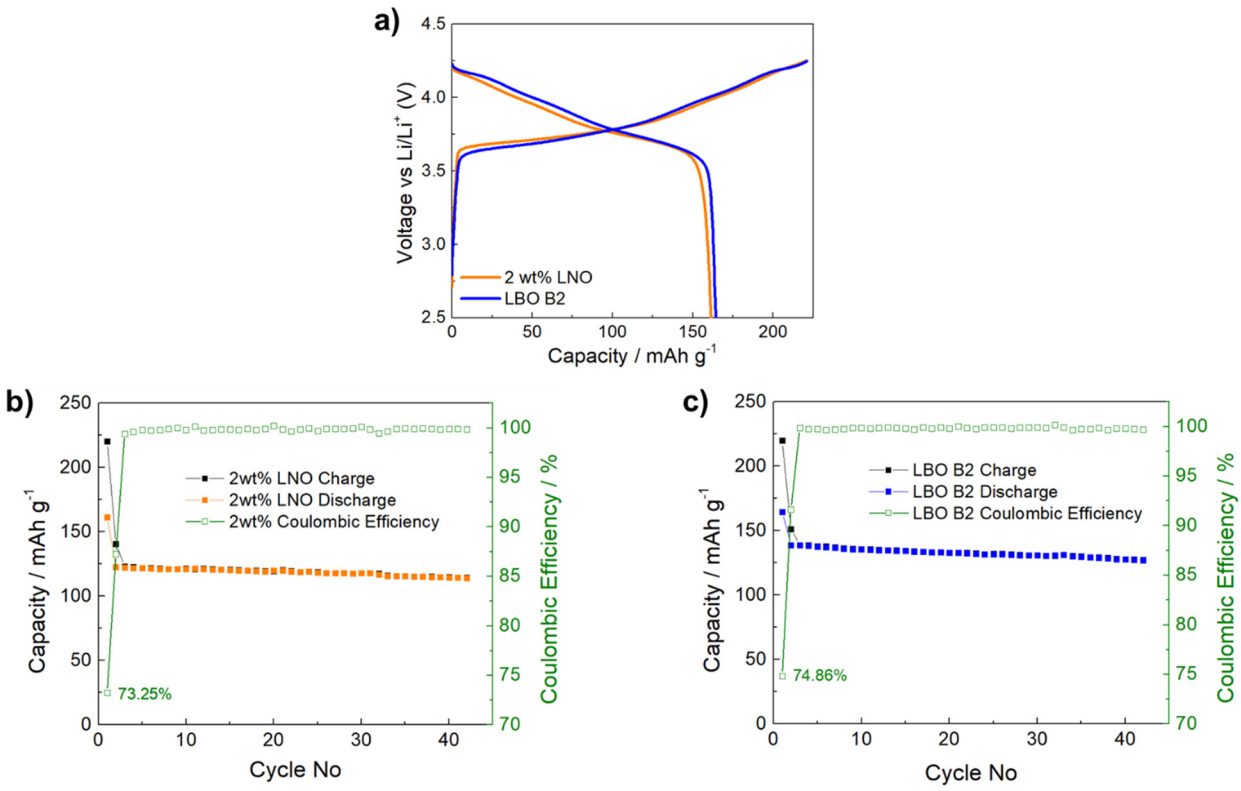

Figure 4.11. Extended cycling comparison between LBO B2 and LNO-coated NCM811. a) first cycle comparison, b) extended cycling for LBO B2, and (c), extended cycling for LNO.

4.4 Conclusion

In sulfide-based all-solid-state batteries (ASSBs) that use an oxide cathode, thin, conformal, and chemically inert oxide-based cathode coatings have been demonstrated to be beneficial for cycling performance as they mitigate unwanted chemical reactions between the SSE and the oxide cathode. Many such coatings have been explored and applied to the cathode in the literature, usually via a solvent-based solution process. In this work, a dry-processed, lithium borate-based coating on NCM811 was shown to have the same desirable properties and even showed a higher first cycle capacity compared to the $LiNbO_3$-based solution-processed coatings. The LBO coating was synthesized by the solid-state reaction of boric acid with Li-containing impurities (such as Li_2CO_3) on the surface of NCM811, without the need for any washing or

subsequent solvent removal. These results demonstrate the promise of both the facile dry-coating process and the LBO coating toward longer-lasting and better-performing ASSBs.

Chapter 4, in full, has been submitted for publication as “A Facile, Dry-Processed Lithium Borate-Based Cathode Coating for Improved All-Solid-State Battery Performance” in the Journal of the Electrochemical Society. Wu, E. A.*, Jo, C.*, Tan, D. H. S., Zhang, M., Doux, J.-M., Chen, Y.-T., Deysher, G., and Meng, Y. S. The dissertation author was the one of the two co-first authors for this study; Wu, E. A. wrote the paper while Jo, C. did most of the experiments. All authors had input on the paper.

Chapter 5. An All-Sputtered, Nanofibrous Ceramic Cathode for Thin-Film Solid Oxide Fuel Cells

Thin film solid oxide fuel cells (TF-SOFCs) are attracting attention due to their ability to operate at comparatively lower temperatures (400°-650°C) that are unattainable for conventional anode-supported SOFCs (650°-800°C). However, limited cathode performance and cell scalability remain persistent issues. Here, we report a new approach of fabricating yttria-stabilized zirconia (YSZ)-based TF-SOFCs via a scalable magnetron sputtering process. Notable is the development and deposition of a porous $La_{0.6}Sr_{0.4}Co_{0.2}Fe_{0.8}O_3$ (LSCF)-based cathode with a unique fibrous nanostructure. This all-sputtered cell shows an open-circuit voltage of ~1.0V and peak power densities of ~1.7 W/cm^2 and ~2.5 W/cm^2 at 600°C and 650°C, respectively, under hydrogen fuel and air, along with showing stable performance in short-term testing. The power densities obtained in this work are the highest among YSZ-based SOFCs at these low temperatures, which demonstrates the feasibility of fabricating exceptionally high-performance TF-SOFC cells with distinctive dense or porous nanostructures for each layer, as desired, by a sputtering process. This work illustrates a new, potentially low-cost, and scalable platform for the fabrication of next-generation TF-SOFCs with excellent power output and stability.

5.1 Introduction

Solid oxide fuel cells (SOFCs) have been developed for a broad spectrum of power generation applications, ranging from watt-sized devices to multi-megawatt power plants.[131] Recently, the introduction of nanotechnology has facilitated the development of thin-film SOFCs (TF-SOFCs) and has shown dramatically improved cell performance, also allowing for operation for the cell at lower temperatures (e.g., 400°-650°C versus the conventional 650°-800°C).[132] Various deposition processes have been used to fabricate cell components for TF-SOFCs, for example, chemical vapor deposition processes such as atomic layer deposition (ALD) have been shown to be capable of depositing high-quality films.[31,133–135] However, it is difficult to fabricate

porous films required for the anode and cathode using ALD; the structure must be porous for efficient gas supply. To this end, pulsed laser deposition (PLD) has also been used and ceramic-based TF-SOFCs fabricated via PLD showed high performance and stability.[136,137] However, since it is difficult to use PLD for large area deposition in addition to high maintenance costs, it is preferable to develop a scalable and cost-effective deposition technique such as sputtering for fabricating TF-SOFCs.

Among various physical vapor deposition processes, sputtering is a versatile technique commonly used in mass production as it can create either porous or dense films just by changing the deposition conditions. Several studies have used sputtering to fabricate TF-SOFCs and showed high performance at relatively low operating temperatures[33]. However, most of these sputtered TF-SOFCs utilized platinum (Pt) as an electrode. Although Pt exhibits high catalytic activity at low temperatures and a porous Pt structure can be made by sputtering[138], Pt can easily agglomerate at elevated temperatures and thus is not suitable for use at typical SOFC operating temperatures of 650°-800°C.[139] Several approaches have been considered to mitigate this such as co-sputtering with ceramics or applying a coating on the Pt surface,[140–142] but the preferable solution is to construct the electrode with a material that is more thermally stable. For this purpose, ceramic-based materials have desirable thermal properties.[143–145] However, it is difficult to make ceramic materials into porous films via sputtering. The most common approach is to sputter using a high pressure of sputtering gas to increase the number of collisions and decrease the kinetic energy of the deposited atoms. This results in low surface mobility of the deposited atoms and the increasing effects of self-shadowing. As the deposition evolves, grains are formed with well-defined and often porous grain boundaries known as zone 1 growth in thin-film deposition.[146] In addition, atoms in the gas can form particle clusters prior to deposition aiding in the formation of porous films. If a porous ceramic electrode can be deposited through sputtering then the entire

cell can be fabricated using a single process and a single piece of equipment, which is more cost-effective and beneficial for future mass production of devices.

To illustrate our approach to fabricate a complete SOFC cell by sputtering, yttria stabilized zirconia (YSZ), Ni-YSZ and lanthanum strontium cobalt ferrite $La_{0.6}Sr_{0.4}Co_{0.2}Fe_{0.8}O_{2.95}$-YSZ (LSCF-YSZ) are the materials chosen for our electrolyte, anode and cathode, respectively, as they are materials which have been shown to have good performance in SOFC applications. Apart from that, a high activation energy owing to the oxygen reduction reaction (ORR) at the interface of cathode and electrolyte is a persistent problem in most SOFC devices. To reduce the activation energy of ORR, using a gadolinia-doped ceria (GDC) cathode functional interlayer sandwiched between the cathode and electrolyte (that can be fabricated by magnetron sputtering)[147,148] is one of the simplest approaches that can be applied in our process.

For TF-SOFCs, the substrate plays a very important role. If the substrate pore size is small and uniform, a thin cell without cracks and defects can be produced on the substrate with sufficient fuel mass transport. From this point of view, anodized aluminum oxide (AAO) substrates are a suitable support upon which thin films, especially thin-film electrolytes, can be deposited.[149,150] AAO is made by anodizing an aluminum sheet where pores of several tens of nanometers are formed and uniformly distributed. Depending on the anodic oxidation conditions, the size of the pore and thus the porosity of the film can be easily manipulated. The tortuosity of AAO can be very low due to the straight and aligned pore structure through the substrate. This ultimately enables fuel to be sufficiently supplied to the cell even with a pore size as small as several tens of nanometers.

In this work, we describe a new method of the development of a porous ceramic nanostructure for SOFC electrodes and incorporate it into a full cell by sputtering at room temperature in a single sputtering process. Characterization of the cells shows fully dense layers for the electrolyte and cathode functional interlayer and well-defined and distinctive

nanostructures for the electrodes. These cells exhibit exceptional power densities, to the best of our knowledge, the highest recorded performance for a YSZ-based SOFC, and this sputtering method can be applied to all kinds of different combinations of materials for porous electrodes, especially the cathode, in TF-SOFCs.

5.2 Results and Discussion

5.2.1 The porous LSCF-YSZ cathode

To fabricate a porous LSCF-based electrode, co-sputtering of Y/Zr metal alloy and LSCF targets was performed. Since Y/Zr can be easily formed into a porous film at high Ar pressures, the co-sputtering of LSCF and Y/Zr could yield a porous film of LSCF-YSZ using similar conditions. The resulting co-sputtered LSCF-YSZ film has a porous, columnar nanostructure as shown in the SEM images in Figure 5.1. According to the images, this columnar structure has a diameter of tens of nanometers, thus creating a very large active surface area.

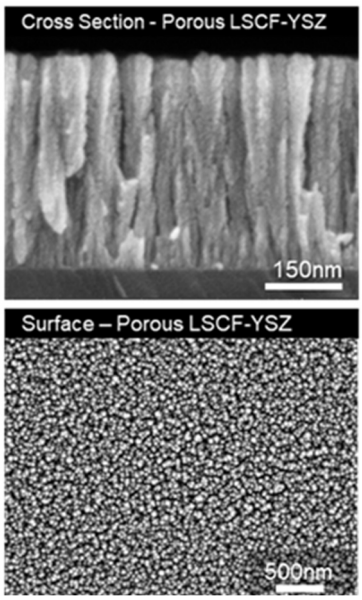

Figure 5.1. SEM images of the co-sputtered LSCF-YSZ. Top: Cross-sectional image and bottom: surface SEM image. 200W was applied to the LSCF ceramic target and 50W was applied to the Y/Zr target.

5.2.2 Full cell fabrication and characterization

The anode, electrolyte, interlayer, and cathode were sequentially sputtered onto the porous AAO and shown schematically in Figure 5.2 with the corresponding STEM micrograph in Figure 5.2a. Figures 5.2b-d show the cross-sectional STEM images and Figures 5e-g show the corresponding SEM images of the surface morphology of each component. With this configuration, no etching or patterning steps were required between sputtering of the different films. One clear benefit was that the samples were kept under vacuum during the fabrication process, especially for complete cells, and thus ambient contamination was minimized since sputtering was done sequentially in the same chamber.

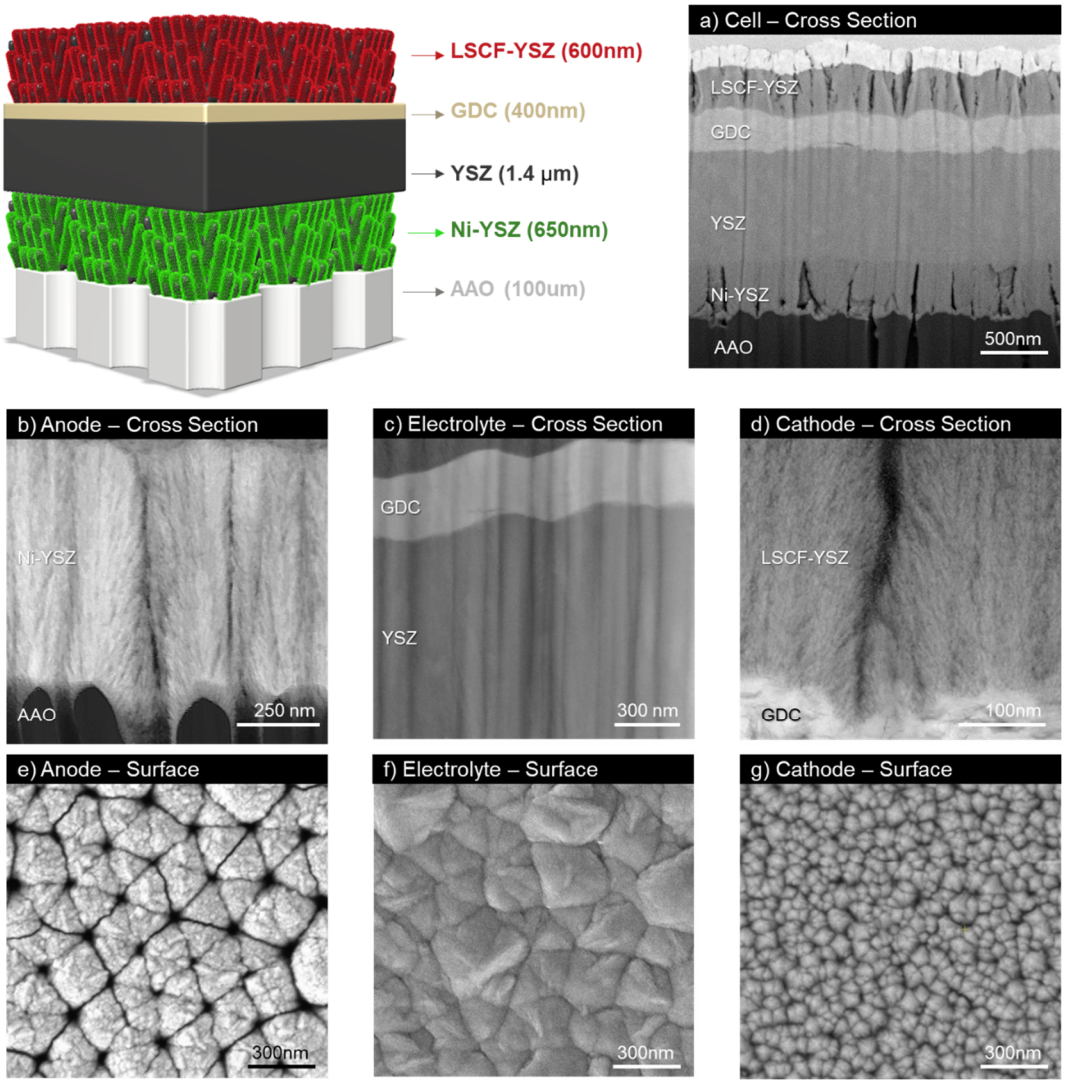

Figure 5.2. Schematic of the cell architecture. (a) Cross section FE-SEM image of the cell architecture. STEM view of the (b) anode, (c) electrolyte with interlayer, and (d) cathode, respectively. Respective FE-SEM surface images of (e) Ni-YSZ layer on AAO, (f) GDC layer, and (g) LSCF-YSZ layer.

A 700 nm Ni-YSZ porous anode layer was deposited onto the AAO. As shown in Figures 5.2a and 5.2b, the Ni-YSZ electrode is formed as a collection of larger columns with a diameter of about 200 nm with smaller columns of less than 10 nm in diameter on top of the 200 nm columns. The surface morphology of Ni-YSZ (Figure 5.2e) showing hexagonally arranged columns that do not completely block the pores of the AAO. This microstructure provides a very high active surface area for the anode, thus significantly improving electrode performance. Figure 5.3a shows the

distribution of the elements through STEM-EDX analysis of the Ni-YSZ electrode. The YSZ electrolyte and the GDC interlayer were deposited on top of the Ni–YSZ anode. As seen in Figure 5.2(a), the YSZ electrolyte has a thickness of about 1.4 μm, relatively thick considering a previous report of 150-nm YSZ electrolytes applied to AAO-based SOFCs[135]. While thin electrolytes can increase performance, the trade-off is that structural defects in fabrication leading to cell failure during operation is more likely to occur. Since structural defects occur in proportion to the cell area, this issue is significantly exacerbated when applying an ultra-thin electrolyte to a large-active-area cell. With these considerations, a relatively thick electrolyte was applied in this study. Even with a high electrolyte thickness, the cells are still capable of achieving exceptional power densities.

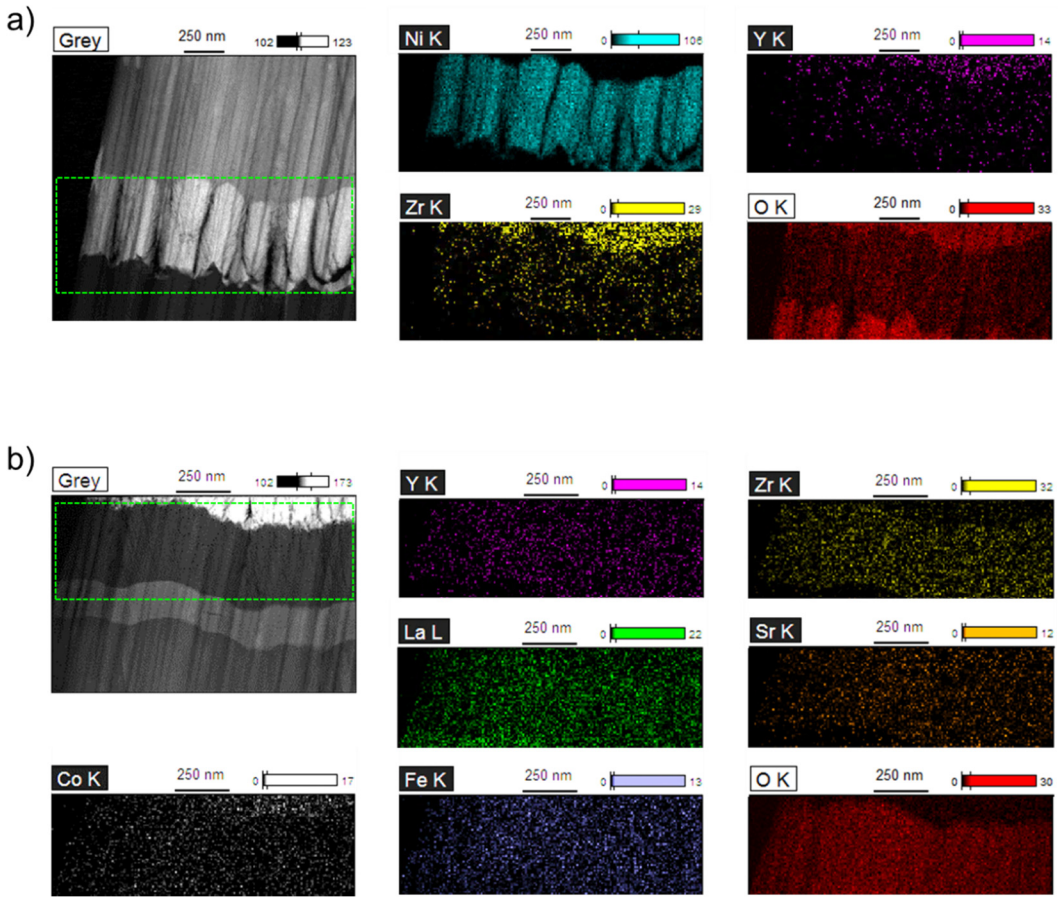

Figure 5.3. STEM-EDX of (a) the Ni-YSZ anode structure and (b) the LSCF-YSZ cathode structure.

A GDC interlayer was deposited between the electrolyte and the cathode. By tuning the power and substrate location in the chamber, dense and uniform GDC layers resulted, as illustrated in Figures 5.2a and 5.2c.

The LSCF-YSZ cathode was then deposited on the top of the GDC interlayer (Figures 5.2d and 5.2g. The LSCF-YSZ shows an extremely fine nano-fibrous structure with a diameter of less than 10nm and relatively large openings between the columns, which ensures high mass transport of oxygen to the whole cathode as well as a large active surface area. STEM-EDX of LSCF-YSZ in Figure 5.3b shows that the signals from La and Fe are more intense than those of Sr and Co; however, further work involves examining the exact stoichiometry of the sputtered LSCF films. In the end, each component of the TF-SOFC, with distinct nanostructures, have been successfully deposited via magnetron sputtering.

5.2.3 Cell performance

Electrochemical analysis of the TF-SOFC is shown in Figure 5.4 The cell has active area of $1mm^2$ (1mm x 1mm) and was tested under pure hydrogen at a flow rate of 50 sccm and exposed to air for the oxygen source. Our tested cells show an open-circuit voltage (OCV) of ~0.95 V and a peak power density of ~ 1.7 W/cm^2 and ~2.5 W/cm^2 at 600°C and 650°C, respectively (Figure 5.4a), the highest recorded power density for YSZ-based SOFC devices. According to the EIS measurement shown in Figure 5.4b, relatively low polarization losses were observed at both 600°C and 650°C. Since the co-sputtered Ni-YSZ electrode and the LSCF-YSZ electrodes consist of nano-fibers of less than 10 nm in diameter, the number of reaction sites in the electrodes were significantly increased. Since the relatively larger vertical pores are formed in the electrodes at every 100-200 nm, the fine microstructure among these larger pores ultimately results in more effective gas delivery.

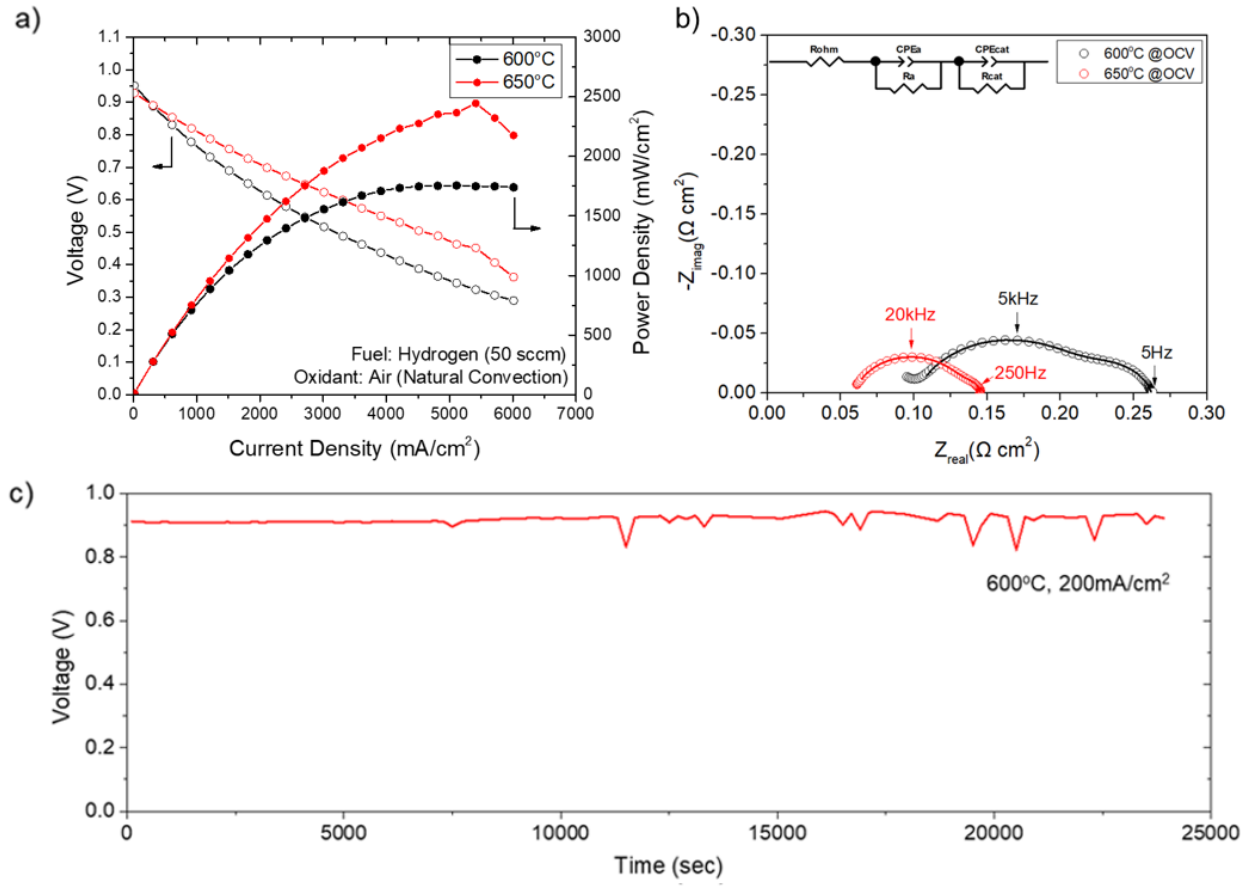

Figure 5.4. a) Current-voltage (I-V) and current-power (I-P) curves and b) EIS measurement of the TF-SOFC with hydrogen fuel and air at 600°C and 650°C, respectively. The lines on the Nyquist plot correspond to the respective fits from the equivalent circuit in the inset. c) Short-term stability test; the cell voltage was measured over time while applying a constant current of 200mA/cm^2.

In terms of materials, a mixture of LSCF and YSZ will increase the triple phase boundary compared to pure LSCF electrodes. Since YSZ has low electrical conductivity, it is required to analyze the effect of the YSZ mixture in LSCF in terms of electrical conductivity and polarization losses. According to the comparison in Figure 5.5, the peak power density for the TF-SOFC with pure LSCF as the cathode was about 550 mW/cm^2 at 600°C, about a third of that compared to the LSCF-YSZ composite at the same temperature. According to the EIS fitting results in Table 5.1, although pure LSCF has a lower ohmic resistance by about 0.05 Ω cm^2, its overall polarization resistance (R_{cat} + R_{pol}) is much greater (by over 1 Ω cm^2). In other words, even though co-sputtering of YSZ with LSCF slightly increases the ohmic resistance, it drastically

reduces the polarization loss, which is consistent with the increased cell performance and peak power density measurements.

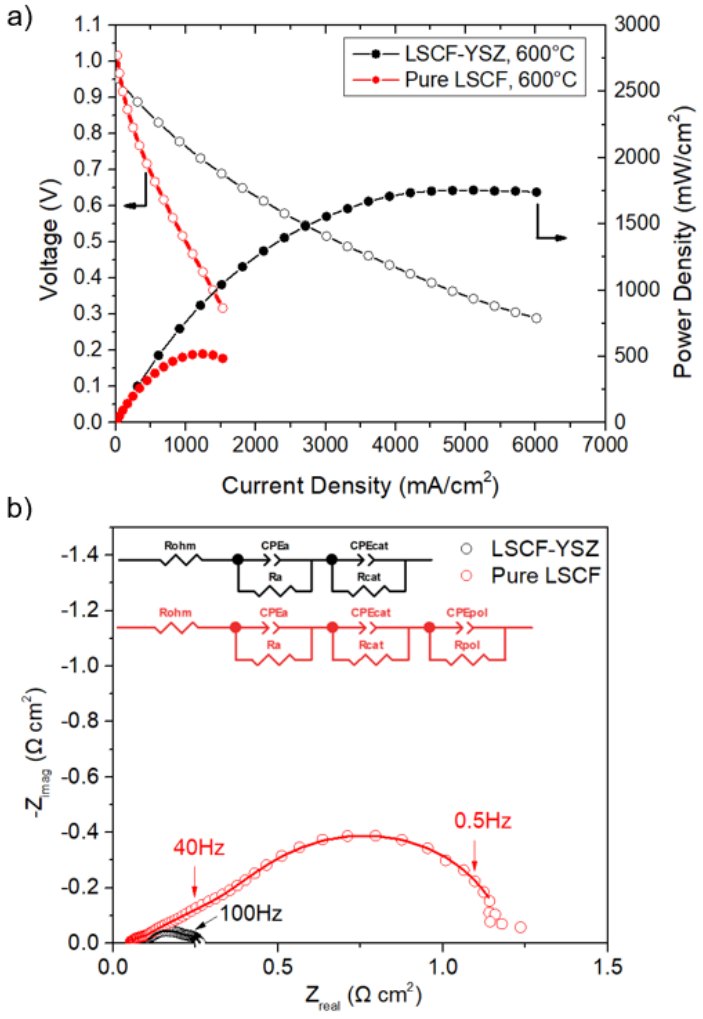

Figure 5.5. a) Current-voltage (I-V) and current-power (I-P) curves and b) EIS measurement of the TF-SOFC using pure LSCF and LSCF-YSZ cathode with hydrogen fuel and air at 600°C. The lines in the Nyquist plot correspond to the respective fits from the equivalent circuits in the inset.

Table 5.1. Impedance contributions from the EIS fitting at 600°C for Pure LSCF and LSCF-YSZ with their corresponding frequency ranges.

Component	LSCF (Ω cm²)	LSCF-YSZ (Ω cm²)
R_{ohm}	0.0515	0.1015
R_a	0.0242 (100kHz-10kHz)	0.0439 (100kHz-10kHz)
R_{cat}	0.5204 (10kHz-3Hz)	0.1167 (10kHz-5Hz)
R_{pol}	0.6254 (3Hz-0.3Hz)	n/a

In order to investigate the cell durability or the cell performance over time, the voltage was measured at a constant current of 200 mA/cm^2 at 600°C and the results are shown in Figure 5.4c. This short-term stability test was performed for about 7 hours where the cell showed a constant voltage without significant degradation. It should be noted that if the cell was operated at the peak power density for extended periods of time without air cooling, the cells tended to fail because of the large amount of heat generated from the high current density.

Lastly, it is important to note that previously, AAO-based TF-SOFCs used Pt electrodes; thus the operating temperature was restricted to 400°-500°C to avoid Pt nanoparticle agglomeration [25,26,31,33,132–135,139–141,149–152]. In this study, by using Ni-YSZ and LSCF-YSZ as the anode and cathode respectively, the cells were able to be tested at 600°-650°C without significant performance degradation. A comparison of our cell performance with other reports on AAO-based TF-SOFCs that use a Ni-based anode and a YSZ-based electrolyte can be found in Figure 5.6.

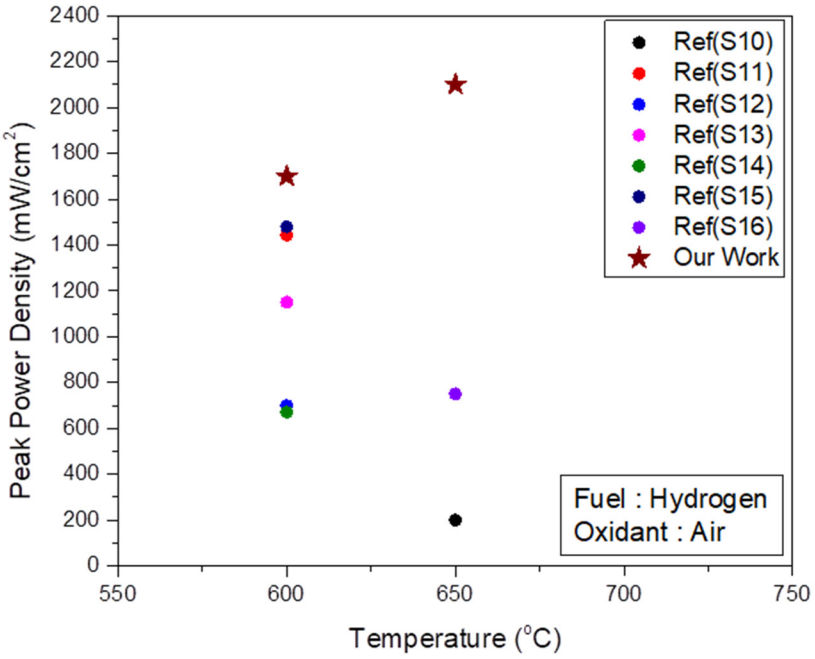

Figure 5.6. Performance comparison with other works that use an Ni-based anode support and YSZ electrolyte[153–159].

5.3 Conclusion

In summary, TF-SOFCs (~3 μm thick) on AAO substrates were fabricated via a sputtering process for all of the cell components, which comprised of conventional materials (YSZ for the electrolyte, GDC for the electrolyte/cathode interlayer, Ni-YSZ for the anode, and LSCF-YSZ for the cathode). Fully dense YSZ and GDC films, along with porous Ni-YSZ and LSCF-YSZ films with columnar nanostructures (that yield a high active surface area) were successfully developed and fabricated. Electrochemical evaluations of the cell showed an OCV of ~1.0 V and exceptional peak power densities of ~1.7 W/cm^2 and ~2.5 W/cm^2 with hydrogen fuel and air at 600°C and 650°C, respectively. Further work is ongoing to refine the cell architecture, optimize and scale up the fabrication process, evaluate long-term performance stability, and investigate cell operation with different hydrocarbon fuels.

Chapter 5, in part, is a reprint of the material “All-Sputtered, Superior Power Density Thin-Film Solid Oxide Fuel Cells with a Novel Nanofibrous Ceramic Cathode” as it appears in Nano

Letters. Lee, Y. H.*, Ren, H.*, Wu, E. A.*, Fullertron, E. E., Meng, Y. S., and Minh, N. Q. 20, 5, 2943–2949. The dissertation author was one of the three co-first authors for this study. The dissertation author performed FIB/SEM characterization as well as EIS analysis.

Chapter 6. Summary and Outlook

As the global energy consumption continues to rise, to drastically lower CO_2 emissions and mitigate the effects of climate change, the continued and rapid adoption of renewable energy sources is paramount and should be a top priority not just relegated to scientists and research labs, but for policymakers all around the world. Associated with this direction, there must also be the reduction in the use of burning fossil fuels which is a key contributor in exacerbating climate change. The development of the materials and storage/conversion technologies in this thesis presents insights for devices that will be undoubtedly necessary to be commercialized and implemented to keep pace with growing energy demands; with the increased adoption of renewable energy generation, there must also be a transformation in grid infrastructure. Without the ability to effectively store the energy generated from renewable sources, a larger strain will be placed on the grid to ramp up demand during surges in electricity use, which can lead to service outages and unreliable delivery. Thus, developing safe and effective energy storage is necessary to accommodate the variation in electricity demand throughout the day and modernize the grid in order to ensure that clean energy can continue to expand and also be efficiently delivered.

Solid-state batteries have been highly desired for grid-storage applications as the promise of a non-flammable, non-toxic electrolyte would mitigate any fears about catastrophic battery fires. While much research has been conducted on increasing the ionic conductivity of the solid electrolytes, the focus is now shifting to understand the multitude of phenomena that occur at the solid-solid interfaces present in the ASSB; these interfaces have been described in detail and all are important to characterize and analyze. Much of the difficulty in understanding these interfaces is their buried nature and the current lack of effective characterization techniques that can target these specific areas; thus, further development of characterization techniques will be necessary in order to further study and understand the ASSBs toward making more effective and longer-lasting battery chemistries.

This dissertation focused on the interfaces in the solid-state battery in context of chemical or electrochemical reactions: the reaction between the sodium solid-state electrolyte Na_3SbS_4 and Na metal, the synthesis and evaluation of the new halide chemistry $Na_{3-x}Y_{1-x}Zr_xCl_6$ with the oxide cathode $NaCrO_2$, and the evaluation of the dry-processed lithium borate protective coating on the oxide cathode NCM811. For the anode study, a combination of electrochemical methods, computational methods, and XPS were used to explore the interfacial products to ultimately explain the battery failure mechanism, which was a result of a direct and spontaneous chemical reaction between Na and Na_3SbS_4 to form the products Na_3Sb and Na_2S. The cell utilized the cathode TiS_2 in order to isolate and study the anode reactivity, and thus the cell voltage was limited to 2.4 V.

Since sulfides typically electrochemically decompose above 2.5 V, in order to enable higher-voltage and thus higher energy density Na ASSBs, the halide chemistry $Na_{3-x}Y_{1-x}Zr_xCl_6$ (NYZC) was developed as its electrochemical window is much wider; it has an oxidation limit of 3.8 V. After investigating aliovalent doping to increase the ionic conductivity via computational and experimental methods and studying the mechanism behind the conductivity increase, NYZC was implemented in a cell utilizing $NaCrO_2$ (operating voltage 2-3.6 V)[160]; compared with NPS, the cell with NYZC displayed a much higher first cycle CE (from 71 to 97%) and also the capacity fade was minimal in comparison due to a lack of electrochemical oxidation nor any chemical reaction between NYZC and $NaCrO_2$. This study demonstrated a proof-of-concept where a new compound, when incorporated into the composite cathode, dramatically extended the cyclability and longevity. There are many different directions to take to further the understanding of NYZC, such as: using other dopants to further increase the conductivity, investigate its structural properties, such as which Na sites undergo exchange, the degree of amorphization upon ball milling, why amorphization increases the conductivity (as it does in the Li counterpart)[88], to experimentally observe the anion rotation mechanism, and even doping with other elements to try to extend the oxidation limit beyond 3.8 V. This result with NYZC does not mean that halides

will supplant sulfides in ASSBs; it means that halides are a relatively new chemical space that are very promising for ASSB applications due to their superior electrochemical stability.

On the Li side, the electrolyte Li_6PS_5Cl is commonly used as it forms a passivating CEI after oxidation, which enables prolonged, reversible cycling after the first cycle. This being the case, one common strategy to extend the cycle life of the ASSB is the implementation of a chemically inert coating, or a coating with a lower reaction energy (both between the LPSCl/coating and coating/cathode) compared to the reaction energy between the LPSCl/cathode itself. A dry-processed, lithium borate coating was applied on the NCM811 cathode and it was characterized via STEM and STEM-EELS and with electrochemical methods. The dry-processed coating, found to eliminate cathode surface impurities, provided comparable performance compared to the solution-processed LNO coating. Further optimization of the lithium borate coating and the application of the dry process to other coating materials would be a future direction to simplify the coating process in general to potentially avoid the use of any solvents in the synthesis process of the battery materials.

It has been shown that it is necessary to find compatible electrolytes and electrodes to make an effective ASSB, especially in the context of mitigating unwanted electrochemical and chemical reactions. However, with regards to Figure 1.4, the other interfaces that were not investigated in this dissertation still nevertheless need to be well-understood and further studied, such as the conductive additive/electrolyte interface as well as the mechanical considerations such as cathode cracking, loss of contact between the current collector/cathode, cathode/electrolyte, or anode/electrolyte, volume changes that can induce such losses of contact, and the prevention of dendritic growth (which is coupled with the density, porosity, and crystallinity of the electrolyte). Characterization tools to probe the mechanical properties or phenomena (e.g. nano-identation in inert atmospheres, x-ray computed tomography or electron microscopy techniques to probe volume changes), battery materials selection with consideration of these mechanical properties (e.g. strain minimization between components), and the optimization of

stack pressure for ASSB cycling, are all necessary in order to develop a more complete understanding to enable longer-lasting ASSBs.

Furthermore, with regards to the pellet cell battery configuration, while the Na-Sn 2:1 alloy was used in conjunction with NPS, the various Na-Sn alloys will also need to be studied; using less Na in the Na-Sn alloy will ultimately decrease the weight of the anode and potentially increase the gravimetric energy density of the battery. Furthermore, the amount of Na-Sn 2:1 alloy used on the anode side during cell construction corresponds to a negative/positive electrode ratio (N/P ratio) of about 28, far surpassing that of typical full cells that have N/P ratios an order of magnitude lower. In essence, the studies in this dissertation were performed on “half cells”, or cells with a large amount of excess anode. Lowering the N/P ratio toward practical values and studying the cycling behavior is thus one direction for further study. Furthermore, reducing the amount of all inactive materials, not just the anode, are required if the ASSBs are to be viable. The pellet cells used in this study, which are electrolyte-supported, have a thickness on the order of 1 mm, far too thick for any practical ASSB format. As a thought experiment, assuming certain values for mass loading for a pouch cell configuration (Table 6.1)[161], just by varying the thickness of the separator/electrolyte alone, it is clear that a 1 mm-thick electrolyte/separator is very detrimental to battery energy density, decreasing it by a factor of 4 (Figure 6.1). It is important to note that the other components pellet cell configuration are also far away from the more-optimized pouch cell values, so the energy density will be even further decreased compared to the values presented in Figure 6.1. Ultimately, the thickness of the SSE must be reduced by around two orders of magnitude to have an energy density competitive with conventional Li-ion batteries. In order to achieve this, instead of the pellet configuration, cast films of the ASSB materials have to be developed and optimized for every component, so finding compatible solvents, binders, and compositions for each layer to enable solution processing will be paramount to enable practical and manufacturable ASSBs. Lastly, coupled with this material optimization will also be increasing the active mass of the composite cathode; for instance, the composite containing $NaCrO_2$, NYZC,

and VGCF only has ~39 wt% $NaCrO_2$, as can be seen in Table 6.1, practical mass loadings will need to be in the range of 90 wt% or greater.

Table 6.1 Cell Parameters of a Real Li|NMC622 Pouch Cell[161].

Cell Component	Cell Parameters	
NMC622 Cathode	1st discharge capacity (mAh/g)	180
	Active material loading	96%
	Total coating weight (mg/cm^2 each side)	20.2
	Areal capacity (mAh/cm^2	3.5
	Electrode press density (g/cm^3)	3.00
	Electrode length (mm)	54
	Electrode width (mm)	36
	Electrode thickness (single side, μm)	67
	Al foil thickness (μm)	15
	Layers	8
Li anode	Cell balance (N/P ratio)	2.86
	Electrode thickness (single side, μm)	50
	Cu foil thickness (μm)	8
Electrolyte	Electrolyte/capacity (g/Ah)	3
	Weight (g)	3.3
Separator	Thickness (μm)	20
Packaging foil	Thickness (μm)	115
Cell	Voltage (V)	3.73
	Capacity (Ah)	1.09

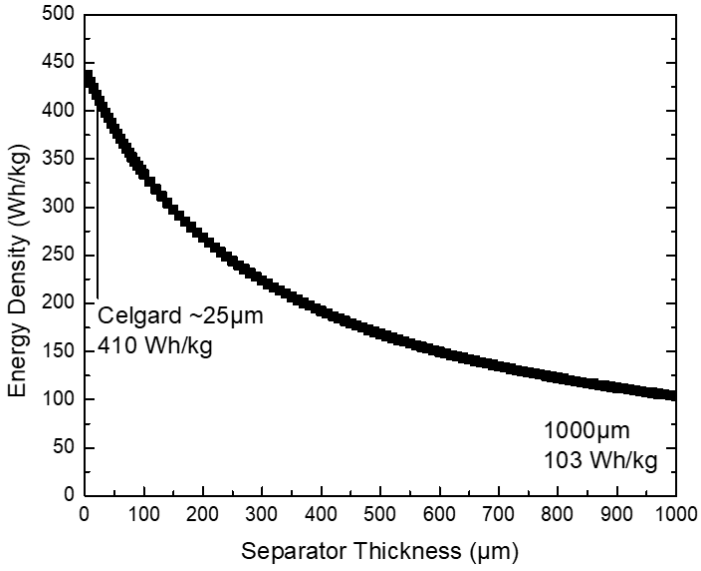

Figure 6.1. The energy density of the cell, assuming the values from Table 6.1, as a function of the separator thickness.

This dissertation also investigated the fabrication of TF-SOFCs; the main benefits of which are the lowered operating temperature, lowered material costs, and the potential to have a wider materials selection. As just stated with the ASSBs, it is also applicable in SOFCs that drastically reducing the material thickness will increase the performance and efficiency of the device. The sputtering method was investigated for thin film deposition and by changing the sputtering conditions (RF/DC power source, O_2 pressure, Ar pressure, substrate location), all layers of the TF-SOFC device (porous anode, dense electrolyte and interlayer, and porous cathode) were able to be fabricated using a single process. Remarkably, the peak power density of up to 2.5 W/cm^2 at 650°C was achieved when applying the co-sputtered LSCF-YSZ cathode.

Future and ongoing work will be to continue to develop these TF-SOFCs using other materials to push the power density further, but also to analyze their performance when using other fuels such as alcohol-based fuels (if fuel reforming is internal rather than external) One problem that can arise to using organic fuels will be carbon deposition or coking at the anode,

which will reduce the cell's efficiency and lifetime. Coking-resistant anodes will thus need to be evaluated as studies expand to other fuel sources.

Secondly, similar to the all-solid-state battery, the form factor of the TF-SOFC will have to be improved in order to demonstrate practical devices. Currently, there are ongoing efforts to scale up the active area of the all-sputtered cell from 1mm^2 to the order of cm^2, but the film quality and uniformity will have to be carefully studied as the active area is gradually increased. It is not as simple as sputtering over a larger area, as defects (such as pinholes) can manifest. Lastly, although the results are promising for the cell development, the SOFC device will be an array or stack of the all-sputtered TF-SOFCs; development of the associated cell interconnects is also ongoing and will be the next step toward a practical and vastly more efficient, high-power energy conversion device.

In this dissertation, many fundamental studies such as characterization of anode interfacial reactions, the evaluation of a halide and also the LBO coating in solid-state pellet cells, and cathode engineering via sputtering for TF-SOFCs were carried out in order to demonstrate proof-of-concepts for understanding cell degradation, increasing cell longevity, increasing the cell cyclability, and increasing TF-SOFC performance while simplifying its fabrication. Such fundamental studies have laid the foundation upon which many future studies and improvements can branch out from. Thorough understanding of materials compatibility in energy storage and conversion devices will serve as an essential guide toward practicality and manufacturability; realizing the energy devices described herein will enable a shift in the global landscape to a cleaner, more sustainable future.

References

(1) Global Temperature Report for 2019. *Berkeley Earth*.

(2) Boden, T.; Marland, G.; Andres, R. J. (1999): Global, Regional, and National Fossil-Fuel CO2 Emissions (1751 - 2014) (V. 2017). Carbon Dioxide Information Analysis Center (CDIAC), Oak Ridge National Laboratory (ORNL), Oak Ridge, TN (United States). doi:10.3334/CDIAC/00001_V2017.

(3) *BP Statistical Review of World Energy. London: British Petroleum Co, 2020. Print.*

(4) Denholm, P.; O'Connell, M.; Brinkman, G.; Jorgenson, J. *Overgeneration from Solar Energy in California. A Field Guide to the Duck Chart*; NREL/TP-6A20-65023; National Renewable Energy Lab. (NREL), Golden, CO (United States), 2015. https://doi.org/10.2172/1226167.

(5) Gao, Z.; Sun, H.; Fu, L.; Ye, F.; Zhang, Y.; Luo, W.; Huang, Y. Promises, Challenges, and Recent Progress of Inorganic Solid-State Electrolytes for All-Solid-State Lithium Batteries. *Advanced Materials* **2018**, *30* (17), 1705702. https://doi.org/10.1002/adma.201705702.

(6) Manthiram, A.; Yu, X.; Wang, S. Lithium Battery Chemistries Enabled by Solid-State Electrolytes. *Nature Reviews Materials* **2017**, *2* (4), 1–16. https://doi.org/10.1038/natrevmats.2016.103.

(7) Wang, Y.; Richards, W. D.; Ong, S. P.; Miara, L. J.; Kim, J. C.; Mo, Y.; Ceder, G. Design Principles for Solid-State Lithium Superionic Conductors. *Nature Materials* **2015**, *14* (10), 1026–1031. https://doi.org/10.1038/nmat4369.

(8) Mizuno, F.; Hayashi, A.; Tadanaga, K.; Tatsumisago, M. New, Highly Ion-Conductive Crystals Precipitated from Li_2S–P_2S_5 Glasses. *Advanced Materials* **2005**, *17* (7), 918–921. https://doi.org/10.1002/adma.200401286.

(9) Kamaya, N.; Homma, K.; Yamakawa, Y.; Hirayama, M.; Kanno, R.; Yonemura, M.; Kamiyama, T.; Kato, Y.; Hama, S.; Kawamoto, K.; Mitsui, A. A Lithium Superionic Conductor. *Nature Mater* **2011**, *10* (9), 682–686. https://doi.org/10.1038/nmat3066.

(10) Kato, Y.; Hori, S.; Saito, T.; Suzuki, K.; Hirayama, M.; Mitsui, A.; Yonemura, M.; Iba, H.; Kanno, R. High-Power All-Solid-State Batteries Using Sulfide Superionic Conductors. *Nature Energy* **2016**, *1* (4), 1–7. https://doi.org/10.1038/nenergy.2016.30.

(11) Bachman, J. C.; Muy, S.; Grimaud, A.; Chang, H.-H.; Pour, N.; Lux, S. F.; Paschos, O.; Maglia, F.; Lupart, S.; Lamp, P.; Giordano, L.; Shao-Horn, Y. Inorganic Solid-State Electrolytes for Lithium Batteries: Mechanisms and Properties Governing Ion Conduction. *Chem. Rev.* **2016**, *116* (1), 140–162. https://doi.org/10.1021/acs.chemrev.5b00563.

(12) Hayashi, A.; Masuzawa, N.; Yubuchi, S.; Tsuji, F.; Hotehama, C.; Sakuda, A.; Tatsumisago, M. A Sodium-Ion Sulfide Solid Electrolyte with Unprecedented Conductivity at Room Temperature. *Nat Commun* **2019**, *10* (1), 1–6. https://doi.org/10.1038/s41467-019-13178-2.

(13) *Mineral Commodity Summaries 2020*; Mineral Commodity Summaries; USGS Unnumbered Series; U.S. Geological Survey: Reston, VA, 2020; p 204. https://doi.org/10.3133/mcs2020.

(14) Roberts, S.; Kendrick, E. The Re-Emergence of Sodium Ion Batteries: Testing, Processing, and Manufacturability. *Nanotechnol Sci Appl* **2018**, *11*, 23–33. https://doi.org/10.2147/NSA.S146365.

(15) Han, F.; Zhu, Y.; He, X.; Mo, Y.; Wang, C. Electrochemical Stability of $Li_{10}GeP_2S_{12}$ and $Li_7La_3Zr_2O_{12}$ Solid Electrolytes. *Advanced Energy Materials* **2016**, *6* (8), 1501590. https://doi.org/10.1002/aenm.201501590.

(16) Takada, K.; Ohta, N.; Zhang, L.; Fukuda, K.; Sakaguchi, I.; Ma, R.; Osada, M.; Sasaki, T. Interfacial Modification for High-Power Solid-State Lithium Batteries. *Solid State Ionics* **2008**, *179* (27), 1333–1337. https://doi.org/10.1016/j.ssi.2008.02.017.

(17) Sakuda, A.; Hayashi, A.; Tatsumisago, M. Interfacial Observation between $LiCoO_2$ Electrode and Li2S−P2S5 Solid Electrolytes of All-Solid-State Lithium Secondary Batteries Using Transmission Electron Microscopy. *Chem. Mater.* **2010**, *22* (3), 949–956. https://doi.org/10.1021/cm901819c.

(18) Banerjee, A.; Park, K. H.; Heo, J. W.; Nam, Y. J.; Moon, C. K.; Oh, S. M.; Hong, S.-T.; Jung, Y. S. Na_3SbS_4: A Solution Processable Sodium Superionic Conductor for All-Solid-State Sodium-Ion Batteries. *Angewandte Chemie International Edition* **2016**, *55* (33), 9634–9638. https://doi.org/10.1002/anie.201604158.

(19) Zhang, L.; Zhang, D.; Yang, K.; Yan, X.; Wang, L.; Mi, J.; Xu, B.; Li, Y. Vacancy-Contained Tetragonal Na_3SbS4 Superionic Conductor. *Advanced Science* **2016**, *3* (10), 1600089. https://doi.org/10.1002/advs.201600089.

(20) Liang, F.-Y.; Ryvak, M.; Sayeed, S.; Zhao, N. The Role of Natural Gas as a Primary Fuel in the near Future, Including Comparisons of Acquisition, Transmission and Waste Handling Costs of as with Competitive Alternatives. *Chem Cent J* **2012**, *6* (Suppl 1), S4. https://doi.org/10.1186/1752-153X-6-S1-S4.

(21) Gür, T. M. Comprehensive Review of Methane Conversion in Solid Oxide Fuel Cells: Prospects for Efficient Electricity Generation from Natural Gas. *Progress in Energy and Combustion Science* **2016**, *54*, 1–64. https://doi.org/10.1016/j.pecs.2015.10.004.

(22) Ignatiev, A.; Ebrahim, R.; Yeleuov, M.; Fisher, D.; Chen, X.; Wu, N.; Tokmoldin, S. Nanostructured Thin Film Solid Oxide Fuel Cells. In *Advanced Nano Deposition Methods*; John Wiley & Sons, Ltd, 2016; pp 223–238. https://doi.org/10.1002/9783527696406.ch12.

(23) Balat, M. Possible Methods for Hydrogen Production. *Energy Sources, Part A: Recovery, Utilization, and Environmental Effects* **2008**, *31* (1), 39–50. https://doi.org/10.1080/15567030701468068.

(24) Irshad, M.; Siraj, K.; Raza, R.; Ali, A.; Tiwari, P.; Zhu, B.; Rafique, A.; Ali, A.; Kaleem Ullah, M.; Usman, A. A Brief Description of High Temperature Solid Oxide Fuel Cell's

Operation, Materials, Design, Fabrication Technologies and Performance. *Applied Sciences* **2016**, *6* (3), 75. https://doi.org/10.3390/app6030075.

(25) Lee, Y. H.; Chang, I.; Cho, G. Y.; Park, J.; Yu, W.; Tanveer, W. H.; Cha, S. W. Thin Film Solid Oxide Fuel Cells Operating Below 600°C: A Review. *Interantional Journal of Precision Engineering and Manufacturing-Green Technology* **2018**, *5* (3), 441–453.

(26) Cho, G. Y.; Lee, Y. H.; Cha, S. W. Multi-Component Nano-Composite Electrode for SOFCS via Thin Film Technique. *Renewable Energy* **2014**, *65*, 130–136. https://doi.org/10.1016/j.renene.2013.07.044.

(27) Wachsman, E. D.; Lee, K. T. Lowering the Temperature of Solid Oxide Fuel Cells. *Science* **2011**, *334* (6058), 935–939. https://doi.org/10.1126/science.1204090.

(28) Beckel, D.; Bieberle-Hütter, A.; Harvey, A.; Infortuna, A.; Muecke, U. P.; Prestat, M.; Rupp, J. L. M.; Gauckler, L. J. Thin Films for Micro Solid Oxide Fuel Cells. *Journal of Power Sources* **2007**, *173* (1), 325–345. https://doi.org/10.1016/j.jpowsour.2007.04.070.

(29) Gómez, S. Y.; Hotza, D. Current Developments in Reversible Solid Oxide Fuel Cells. *Renewable and Sustainable Energy Reviews* **2016**, *61*, 155–174. https://doi.org/10.1016/j.rser.2016.03.005.

(30) Li, X.; Liu, J.; Banis, M. N.; Lushington, A.; Li, R.; Cai, M.; Sun, X. Atomic Layer Deposition of Solid-State Electrolyte Coated Cathode Materials with Superior High-Voltage Cycling Behavior for Lithium Ion Battery Application. *Energy Environ. Sci.* **2014**, *7* (2), 768–778. https://doi.org/10.1039/C3EE42704H.

(31) Shim, J. H.; Park, J. S.; An, J.; Gür, T. M.; Kang, S.; Prinz, F. B. Intermediate-Temperature Ceramic Fuel Cells with Thin Film Yttrium-Doped Barium Zirconate Electrolytes. *Chemistry of Materials* **2009**, *21* (14), 3290–3296. https://doi.org/10.1021/cm900820p.

(32) Xie, Y.; Neagu, R.; Hsu, C.-S.; Zhang, X.; Decès-Petit, C.; Qu, W.; Hui, R.; Yick, S.; Robertson, M.; Maric, R.; Ghosh, D. Thin Film Solid Oxide Fuel Cells Deposited by Spray Pyrolysis. *J. Fuel Cell Sci. Technol* **2010**, *7* (2). https://doi.org/10.1115/1.3176401.

(33) Tsuchiya, M.; Lai, B. K.; Ramanathan, S. Scalable Nanostructured Membranes for Solid-Oxide Fuel Cells. *Nature Nanotechnology* **2011**, *6* (5), 282–286. https://doi.org/10.1038/nnano.2011.43.

(34) Noh, H.-S.; Hong, J.; Kim, H.; Yoon, K. J.; Kim, B.-K.; Lee, H.-W.; Lee, J.-H.; Son, J.-W. Scale-Up of Thin-Film Deposition-Based Solid Oxide Fuel Cell by Sputtering, a Commercially Viable Thin-Film Technology. *J. Electrochem. Soc.* **2016**, *163* (7), F613. https://doi.org/10.1149/2.0331607jes.

(35) Kiratzis, N. E. Applications of the Technique of Solution Aerosol Thermolysis (SAT) in Solid Oxide Fuel Cell (SOFC) Component Fabrication. *Ionics* **2016**, *22* (6), 751–770. https://doi.org/10.1007/s11581-016-1704-3.

(36) Xu, K. Nonaqueous Liquid Electrolytes for Lithium-Based Rechargeable Batteries. *Chem. Rev.* **2004**, *104* (10), 4303–4418. https://doi.org/10.1021/cr030203g.

(37) Goodenough, J. B.; Kim, Y. Challenges for Rechargeable Li Batteries. *Chem. Mater.* **2010**, *22* (3), 587–603. https://doi.org/10.1021/cm901452z.

(38) Baggetto, L.; Niessen, R. A. H.; Roozeboom, F.; Notten, P. H. L. High Energy Density All-Solid-State Batteries: A Challenging Concept Towards 3D Integration. *Advanced Functional Materials* **2008**, *18* (7), 1057–1066. https://doi.org/10.1002/adfm.200701245.

(39) Wang, L. P.; Yu, L.; Wang, X.; Srinivasan, M.; Xu, Z. J. Recent Developments in Electrode Materials for Sodium-Ion Batteries. *J. Mater. Chem. A* **2015**, *3* (18), 9353–9378. https://doi.org/10.1039/C4TA06467D.

(40) Massé, R. C.; Uchaker, E.; Cao, G. Beyond Li-Ion: Electrode Materials for Sodium- and Magnesium-Ion Batteries. *Sci. China Mater.* **2015**, *58* (9), 715–766. https://doi.org/10.1007/s40843-015-0084-8.

(41) Ellis, B. L.; Nazar, L. F. Sodium and Sodium-Ion Energy Storage Batteries. *Current Opinion in Solid State and Materials Science* **2012**, *16* (4), 168–177. https://doi.org/10.1016/j.cossms.2012.04.002.

(42) Richards, W. D.; Tsujimura, T.; Miara, L. J.; Wang, Y.; Kim, J. C.; Ong, S. P.; Uechi, I.; Suzuki, N.; Ceder, G. Design and Synthesis of the Superionic Conductor $Na_{10}SnP_2S_{12}$. *Nat Commun* **2016**, *7*. https://doi.org/10.1038/ncomms11009.

(43) Kundu, D.; Talaie, E.; Duffort, V.; Nazar, L. F. The Emerging Chemistry of Sodium Ion Batteries for Electrochemical Energy Storage. *Angewandte Chemie International Edition* **2015**, *54* (11), 3431–3448. https://doi.org/10.1002/anie.201410376.

(44) Yabuuchi, N.; Kubota, K.; Dahbi, M.; Komaba, S. Research Development on Sodium-Ion Batteries. *Chem. Rev.* **2014**, *114* (23), 11636–11682. https://doi.org/10.1021/cr500192f.

(45) Song, S.; Duong, H. M.; Korsunsky, A. M.; Hu, N.; Lu, L. A Na + Superionic Conductor for Room-Temperature Sodium Batteries. *Scientific Reports* **2016**, *6* (1), 32330. https://doi.org/10.1038/srep32330.

(46) Deng, Z.; Mo, Y.; Ong, S. P. Computational Studies of Solid-State Alkali Conduction in Rechargeable Alkali-Ion Batteries. *NPG Asia Materials* **2016**, *8* (3), e254–e254. https://doi.org/10.1038/am.2016.7.

(47) Tatsumisago, M.; Hayashi, A. Sulfide Glass-Ceramic Electrolytes for All-Solid-State Lithium and Sodium Batteries. *International Journal of Applied Glass Science* **2014**, *5* (3), 226–235. https://doi.org/10.1111/ijag.12084.

(48) Pan, H.; Hu, Y.-S.; Chen, L. Room-Temperature Stationary Sodium-Ion Batteries for Large-Scale Electric Energy Storage. *Energy Environ. Sci.* **2013**, *6* (8), 2338–2360. https://doi.org/10.1039/C3EE40847G.

(49) Hooper, A.; McGeehin, P.; Hughes, A. E. A Study of the Electrical Properties of Single Crystal and Polycrystalline β-Alumina Using Complex Plane Methods. In *Superionic Conductors*; Mahan, G. D., Roth, W. L., Eds.; Physics of Solids and Liquids; Springer US: Boston, MA, 1976; pp 99–100. https://doi.org/10.1007/978-1-4615-8789-7_8.

(50) Anantharamulu, N.; Koteswara Rao, K.; Rambabu, G.; Vijaya Kumar, B.; Radha, V.; Vithal, M. A Wide-Ranging Review on Nasicon Type Materials. *J Mater Sci* **2011**, *46* (9), 2821–2837. https://doi.org/10.1007/s10853-011-5302-5.

(51) Bo, S.-H.; Wang, Y.; Kim, J. C.; Richards, W. D.; Ceder, G. Computational and Experimental Investigations of Na-Ion Conduction in Cubic Na_3PSe_4. *Chem. Mater.* **2016**, *28* (1), 252–258. https://doi.org/10.1021/acs.chemmater.5b04013.

(52) Chu, I.-H.; Nguyen, H.; Hy, S.; Lin, Y.-C.; Wang, Z.; Xu, Z.; Deng, Z.; Meng, Y. S.; Ong, S. P. Insights into the Performance Limits of the $Li_7P_3S_{11}$ Superionic Conductor: A Combined First-Principles and Experimental Study. *ACS Appl. Mater. Interfaces* **2016**, *8* (12), 7843–7853. https://doi.org/10.1021/acsami.6b00833.

(53) Zhang, L.; Yang, K.; Mi, J.; Lu, L.; Zhao, L.; Wang, L.; Li, Y.; Zeng, H. Na_3PSe_4: A Novel Chalcogenide Solid Electrolyte with High Ionic Conductivity. *Advanced Energy Materials* **2015**, *5* (24), 1501294. https://doi.org/10.1002/aenm.201501294.

(54) Sakuda, A.; Hayashi, A.; Tatsumisago, M. Sulfide Solid Electrolyte with Favorable Mechanical Property for All-Solid-State Lithium Battery. *Scientific Reports* **2013**, *3* (1), 2261. https://doi.org/10.1038/srep02261.

(55) Chu, I.-H.; Kompella, C. S.; Nguyen, H.; Zhu, Z.; Hy, S.; Deng, Z.; Meng, Y. S.; Ong, S. P. Room-Temperature All-Solid-State Rechargeable Sodium-Ion Batteries with a Cl-Doped Na_3PS_4 Superionic Conductor. *Sci Rep* **2016**, *6* (1), 1–10. https://doi.org/10.1038/srep33733.

(56) Yu, C.; Ganapathy, S.; Klerk, N. J. J. de; Eck, E. R. H. van; Wagemaker, M. Na-Ion Dynamics in Tetragonal and Cubic Na_3PS_4, a Na-Ion Conductor for Solid State Na-Ion Batteries. *J. Mater. Chem. A* **2016**, *4* (39), 15095–15105. https://doi.org/10.1039/C6TA05896E.

(57) Hayashi, A.; Noi, K.; Tanibata, N.; Nagao, M.; Tatsumisago, M. High Sodium Ion Conductivity of Glass–Ceramic Electrolytes with Cubic Na_3PS_4. *Journal of Power Sources* **2014**, *258*, 420–423. https://doi.org/10.1016/j.jpowsour.2014.02.054.

(58) Nguyen, H.; Hy, S.; Wu, E.; Deng, Z.; Samiee, M.; Yersak, T.; Luo, J.; Ong, S. P.; Meng, Y. S. Experimental and Computational Evaluation of a Sodium-Rich Anti-Perovskite for Solid State Electrolytes. *J. Electrochem. Soc.* **2016**, *163* (10), A2165–A2171. https://doi.org/10.1149/2.0091610jes.

(59) Wang, Y.; Wang, Q.; Liu, Z.; Zhou, Z.; Li, S.; Zhu, J.; Zou, R.; Wang, Y.; Lin, J.; Zhao, Y. Structural Manipulation Approaches towards Enhanced Sodium Ionic Conductivity in Na-Rich Antiperovskites. *Journal of Power Sources* **2015**, *293*, 735–740. https://doi.org/10.1016/j.jpowsour.2015.06.002.

(60) Jansen, M.; Henseler, U. Synthesis, Structure Determination, and Ionic Conductivity of Sodium Tetrathiophosphate. *Journal of Solid State Chemistry* **1992**, *99* (1), 110–119. https://doi.org/10.1016/0022-4596(92)90295-7.

(61) Hayashi, A.; Noi, K.; Sakuda, A.; Tatsumisago, M. Superionic Glass-Ceramic Electrolytes for Room-Temperature Rechargeable Sodium Batteries. *Nat Commun* **2012**, *3* (1), 856. https://doi.org/10.1038/ncomms1843.

(62) Hibi, Y.; Tanibata, N.; Hayashi, A.; Tatsumisago, M. Preparation of Sodium Ion Conducting Na_3PS_4–NaI Glasses by a Mechanochemical Technique. *Solid State Ionics* **2015**, *270*, 6–9. https://doi.org/10.1016/j.ssi.2014.11.024.

(63) Tanibata, N.; Noi, K.; Hayashi, A.; Tatsumisago, M. Preparation and Characterization of Highly Sodium Ion Conducting Na_3PS_4–Na_4SiS_4 Solid Electrolytes. *RSC Adv.* **2014**, *4* (33), 17120–17123. https://doi.org/10.1039/C4RA00996G.

(64) Wenzel, S.; Leichtweiss, T.; Weber, D. A.; Sann, J.; Zeier, W. G.; Janek, J. Interfacial Reactivity Benchmarking of the Sodium Ion Conductors Na_3PS_4 and Sodium β-Alumina for Protected Sodium Metal Anodes and Sodium All-Solid-State Batteries. *ACS Appl. Mater. Interfaces* **2016**, *8* (41), 28216–28224. https://doi.org/10.1021/acsami.6b10119.

(65) Rodríguez-Carvajal, J.; Rousse, G.; Masquelier, C.; Hervieu, M. Electronic Crystallization in a Lithium Battery Material: Columnar Ordering of Electrons and Holes in the Spinel $LiMn_2O_4$. *Phys. Rev. Lett.* **1998**, *81* (21), 4660–4663. https://doi.org/10.1103/PhysRevLett.81.4660.

(66) Brug, G. J.; van den Eeden, A. L. G.; Sluyters-Rehbach, M.; Sluyters, J. H. The Analysis of Electrode Impedances Complicated by the Presence of a Constant Phase Element. *Journal of Electroanalytical Chemistry and Interfacial Electrochemistry* **1984**, *176* (1), 275–295. https://doi.org/10.1016/S0022-0728(84)80324-1.

(67) Heyd, J.; Scuseria, G. E. Efficient Hybrid Density Functional Calculations in Solids: Assessment of the Heyd–Scuseria–Ernzerhof Screened Coulomb Hybrid Functional. *J. Chem. Phys.* **2004**, *121* (3), 1187–1192. https://doi.org/10.1063/1.1760074.

(68) Heyd, J.; Scuseria, G. E.; Ernzerhof, M. Hybrid Functionals Based on a Screened Coulomb Potential. *J. Chem. Phys.* **2003**, *118* (18), 8207–8215. https://doi.org/10.1063/1.1564060.

(69) Whittingham, M. S. Chemistry of Intercalation Compounds: Metal Guests in Chalcogenide Hosts. *Progress in Solid State Chemistry* **1978**, *12* (1), 41–99. https://doi.org/10.1016/0079-6786(78)90003-1.

(70) Conroy, L. E.; Park, K. C. Electrical Properties of the Group IV Disulfides, Titanium Disulfide, Zirconium Disulfide, Hafnium Disulfide and Tin Disulfide. *Inorg. Chem.* **1968**, *7* (3), 459–463. https://doi.org/10.1021/ic50061a015.

(71) Zhang, D.; Cao, X.; Xu, D.; Wang, N.; Yu, C.; Hu, W.; Yan, X.; Mi, J.; Wen, B.; Wang, L.; Zhang, L. Synthesis of Cubic Na_3SbS_4 Solid Electrolyte with Enhanced Ion Transport for All-Solid-State Sodium-Ion Batteries. *Electrochimica Acta* **2018**, *259*, 100–109. https://doi.org/10.1016/j.electacta.2017.10.173.

(72) Yue, J.; Han, F.; Fan, X.; Zhu, X.; Ma, Z.; Yang, J.; Wang, C. High-Performance All-Inorganic Solid-State Sodium–Sulfur Battery. *ACS Nano* **2017**, *11* (5), 4885–4891. https://doi.org/10.1021/acsnano.7b01445.

(73) Zhang, W.; Leichtweiß, T.; Culver, S. P.; Koerver, R.; Das, D.; Weber, D. A.; Zeier, W. G.; Janek, J. The Detrimental Effects of Carbon Additives in $Li_{10}GeP_2S_{12}$-Based Solid-State Batteries. *ACS Appl. Mater. Interfaces* **2017**, *9* (41), 35888–35896. https://doi.org/10.1021/acsami.7b11530.

(74) Hakari, T.; Sato, Y.; Yoshimi, S.; Hayashi, A.; Tatsumisago, M. Favorable Carbon Conductive Additives in Li_3PS_4 Composite Positive Electrode Prepared by Ball-Milling for All-Solid-State Lithium Batteries. *J. Electrochem. Soc.* **2017**, *164* (12), A2804. https://doi.org/10.1149/2.1831712jes.

(75) Chen, C. H.; Liu, J.; Amine, K. Symmetric Cell Approach and Impedance Spectroscopy of High Power Lithium-Ion Batteries. *Journal of Power Sources* **2001**, *96* (2), 321–328. https://doi.org/10.1016/S0378-7753(00)00666-2.

(76) Nara, H.; Morita, K.; Yokoshima, T.; Mukoyama, D.; Momma, T.; Osaka, T. Electrochemical Impedance Spectroscopy Analysis with a Symmetric Cell for $LiCoO_2$ Cathode Degradation Correlated with Co Dissolution. *AIMS Materials Science* **2016**, *3* (2), 448. https://doi.org/10.3934/matersci.2016.2.448.

(77) Zhang, X.; Zhang, W.; Lei, G. A Review of Li-Ion Battery Equivalent Circuit Models. *Transactions on Electrical and Electronic Materials* **2016**, *17* (6), 311–316. https://doi.org/10.4313/TEEM.2016.17.6.311.

(78) Chang, M.-T.; Lin, Y.-S.; Ling, S.-H.; Liang, S.-H.; Lin, C.-H.; Chen, K.-C. Identification of the Parameters in Equivalent Circuit Model of Lithium-Ion Batteries. *ECS Trans.* **2014**, *61* (27), 125. https://doi.org/10.1149/06127.0125ecst.

(79) Bron, P.; Roling, B.; Dehnen, S. Impedance Characterization Reveals Mixed Conducting Interphases between Sulfidic Superionic Conductors and Lithium Metal Electrodes. *Journal of Power Sources* **2017**, *352*, 127–134. https://doi.org/10.1016/j.jpowsour.2017.03.103.

(80) Ettema, A. R. H. F.; de Groot, R. A. Electronic Structure of Na_3Sb and Na_2KSb. *Phys. Rev. B* **2000**, *61* (15), 10035–10039. https://doi.org/10.1103/PhysRevB.61.10035.

(81) Bertheville, B.; Low, D.; Bill, H.; Kubel, F. Ionic Conductivity of Na_2S Single Crystals between 295 and 1350 K Experimental Setup and First Results. *Journal of Physics and Chemistry of Solids* **1997**, *58* (10), 1569–1577. https://doi.org/10.1016/S0022-3697(97)00101-7.

(82) Tanibata, N.; Deguchi, M.; Hayashi, A.; Tatsumisago, M. All-Solid-State Na/S Batteries with a Na_3PS_4 Electrolyte Operating at Room Temperature. *Chem. Mater.* **2017**, *29* (12), 5232–5238. https://doi.org/10.1021/acs.chemmater.7b01116.

(83) Qi, Z.; Lan, H.; Joshi, T. P.; Liu, R.; Liu, H.; Qu, J. Enhanced Oxidative and Adsorptive Capability towards Antimony by Copper-Doping into Magnetite Magnetic Particles. *RSC Adv.* **2016**, *6* (71), 66990–67001. https://doi.org/10.1039/C6RA13412B.

(84) Dobler, D.; Oswald, S.; Wetzig, K. Calibration of XPS – Energy Scale for Determination of the Oxidation States of Doping Elements in SnO_2 Powders. *Anal Bioanal Chem* **2002**, *374* (4), 646–649. https://doi.org/10.1007/s00216-002-1448-y.

(85) Wang, Q.; Li, J.; Li, J. Enhanced Thermoelectric Performance of Cu_3SbS_4 Flower-like Hierarchical Architectures Composed of Cl Doped Nanoflakes via an in Situ Generated CuS Template. *Phys. Chem. Chem. Phys.* **2018**, *20* (3), 1460–1475. https://doi.org/10.1039/C7CP06465A.

(86) Richards, W. D.; Miara, L. J.; Wang, Y.; Kim, J. C.; Ceder, G. Interface Stability in Solid-State Batteries. *Chem. Mater.* **2016**, *28* (1), 266–273. https://doi.org/10.1021/acs.chemmater.5b04082.

(87) Wang, Y.; Song, S.; Xu, C.; Hu, N.; Molenda, J.; Lu, L. Development of Solid-State Electrolytes for Sodium-Ion Battery–A Short Review. *Nano Materials Science* **2019**, *1* (2), 91–100. https://doi.org/10.1016/j.nanoms.2019.02.007.

(88) Asano, T.; Sakai, A.; Ouchi, S.; Sakaida, M.; Miyazaki, A.; Hasegawa, S. Solid Halide Electrolytes with High Lithium-Ion Conductivity for Application in 4 V Class Bulk-Type All-Solid-State Batteries. *Advanced Materials* **2018**, *30* (44), 1803075. https://doi.org/10.1002/adma.201803075.

(89) Li, X.; Liang, J.; Luo, J.; Banis, M. N.; Wang, C.; Li, W.; Deng, S.; Yu, C.; Zhao, F.; Hu, Y.; Sham, T.-K.; Zhang, L.; Zhao, S.; Lu, S.; Huang, H.; Li, R.; Adair, K. R.; Sun, X. Air-Stable Li_3InCl_6 Electrolyte with High Voltage Compatibility for All-Solid-State Batteries. *Energy Environ. Sci.* **2019**, *12* (9), 2665–2671. https://doi.org/10.1039/C9EE02311A.

(90) Liang, J.; Li, X.; Wang, S.; Adair, K. R.; Li, W.; Zhao, Y.; Wang, C.; Hu, Y.; Zhang, L.; Zhao, S.; Lu, S.; Huang, H.; Li, R.; Mo, Y.; Sun, X. Site-Occupation-Tuned Superionic Li_xScCl_{3+x} Halide Solid Electrolytes for All-Solid-State Batteries. *J. Am. Chem. Soc.* **2020**, *142* (15), 7012–7022. https://doi.org/10.1021/jacs.0c00134.

(91) Wang, S.; Bai, Q.; Nolan, A. M.; Liu, Y.; Gong, S.; Sun, Q.; Mo, Y. Lithium Chlorides and Bromides as Promising Solid-State Chemistries for Fast Ion Conductors with Good Electrochemical Stability. *Angewandte Chemie International Edition* **2019**, *58* (24), 8039–8043. https://doi.org/10.1002/anie.201901938.

(92) Wickleder, M. S.; Meyer, G. Ternäre Halogenide vom Typ A_3MX_6. Synthese, Strukturen und Ionenleitfähigkeit der Halogenide Na_3MX_6 (X = Cl, Br). *Zeitschrift für anorganische und allgemeine Chemie* **1995**, *621* (3), 457–463. https://doi.org/10.1002/zaac.19956210321.

(93) Jain, A.; Ong, S. P.; Hautier, G.; Chen, W.; Richards, W. D.; Dacek, S.; Cholia, S.; Gunter, D.; Skinner, D.; Ceder, G.; Persson, K. A. Commentary: The Materials Project: A Materials Genome Approach to Accelerating Materials Innovation. *APL Materials* **2013**, *1* (1), 011002. https://doi.org/10.1063/1.4812323.

(94) Ong, S. P.; Cholia, S.; Jain, A.; Brafman, M.; Gunter, D.; Ceder, G.; Persson, K. A. The Materials Application Programming Interface (API): A Simple, Flexible and Efficient API for Materials Data Based on REpresentational State Transfer (REST) Principles. *Computational Materials Science* **2015**, *97*, 209–215. https://doi.org/10.1016/j.commatsci.2014.10.037.

(95) Bergerhoff, G.; Hundt, R.; Sievers, R.; Brown, I. D. The Inorganic Crystal Structure Data Base. *J. Chem. Inf. Comput. Sci.* **1983**, *23* (2), 66–69. https://doi.org/10.1021/ci00038a003.

(96) Tang, H.; Deng, Z.; Lin, Z.; Wang, Z.; Chu, I.-H.; Chen, C.; Zhu, Z.; Zheng, C.; Ong, S. P. Probing Solid–Solid Interfacial Reactions in All-Solid-State Sodium-Ion Batteries with First-Principles Calculations. *Chem. Mater.* **2018**, *30* (1), 163–173. https://doi.org/10.1021/acs.chemmater.7b04096.

(97) Ong, S. P.; Wang, L.; Kang, B.; Ceder, G. Li−Fe−P−O_2 Phase Diagram from First Principles Calculations. *Chem. Mater.* **2008**, *20* (5), 1798–1807. https://doi.org/10.1021/cm702327g.

(98) Liao, W.; Dronskowski, R. Trisodium Yttrium(III) Hexachloride. *Acta Cryst E* **2004**, *60* (6), i72–i73. https://doi.org/10.1107/S1600536804011043.

(99) Sun, Y.; Suzuki, K.; Hori, S.; Hirayama, M.; Kanno, R. Superionic Conductors: $Li_{10+\delta}[Sn_ySi_{1-y}]_{1+\delta}P_{2-\delta}S_{12}$ with a $Li_{10}GeP_2S_{12}$-Type Structure in the Li_3PS_4–Li_4SnS_4–Li_4SiS_4 Quasi-Ternary System. *Chem. Mater.* **2017**, *29* (14), 5858–5864. https://doi.org/10.1021/acs.chemmater.7b00886.

(100) Zhao, W.; Yi, J.; He, P.; Zhou, H. Solid-State Electrolytes for Lithium-Ion Batteries: Fundamentals, Challenges and Perspectives. *Electrochem. Energ. Rev.* **2019**, *2* (4), 574–605. https://doi.org/10.1007/s41918-019-00048-0.

(101) Jolley, A. G.; Cohn, G.; Hitz, G. T.; Wachsman, E. D. Improving the Ionic Conductivity of NASICON through Aliovalent Cation Substitution of $Na_3Zr_2Si_2PO_{12}$. *Ionics* **2015**, *21* (11), 3031–3038. https://doi.org/10.1007/s11581-015-1498-8.

(102) Sleigh, C.; Pijpers, A. P.; Jaspers, A.; Coussens, B.; Meier, R. J. On the Determination of Atomic Charge via ESCA Including Application to Organometallics. *Journal of Electron Spectroscopy and Related Phenomena* **1996**, *77* (1), 41–57. https://doi.org/10.1016/0368-2048(95)02392-5.

(103) Duchêne, L.; Kim, D. H.; Song, Y. B.; Jun, S.; Moury, R.; Remhof, A.; Hagemann, H.; Jung, Y. S.; Battaglia, C. Crystallization of Closo-Borate Electrolytes from Solution Enabling Infiltration into Slurry-Casted Porous Electrodes for All-Solid-State Batteries. *Energy Storage Materials* **2020**, *26*, 543–549. https://doi.org/10.1016/j.ensm.2019.11.027.

(104) Duchêne, L.; Kühnel, R.-S.; Stilp, E.; Reyes, E. C.; Remhof, A.; Hagemann, H.; Battaglia, C. A Stable 3 V All-Solid-State Sodium–Ion Battery Based on a Closo-Borate Electrolyte. *Energy Environ. Sci.* **2017**, *10* (12), 2609–2615. https://doi.org/10.1039/C7EE02420G.

(105) Ando, T.; Sakuda, A.; Tatsumisago, M.; Hayashi, A. All-Solid-State Sodium-Sulfur Battery Showing Full Capacity with Activated Carbon MSP20-Sulfur-Na_3SbS_4 Composite. *Electrochemistry Communications* **2020**, *116*, 106741. https://doi.org/10.1016/j.elecom.2020.106741.

(106) Wan, H.; Mwizerwa, J. P.; Qi, X.; Liu, X.; Xu, X.; Li, H.; Hu, Y.-S.; Yao, X. Core–Shell $Fe_{1-X}S$@$Na_{2.9}PS_{3.95}Se_{0.05}$ Nanorods for Room Temperature All-Solid-State Sodium Batteries with High Energy Density. *ACS Nano* **2018**, *12* (3), 2809–2817. https://doi.org/10.1021/acsnano.8b00073.

(107) Zhang, S.; Zhao, Y.; Zhao, F.; Zhang, L.; Wang, C.; Li, X.; Liang, J.; Li, W.; Sun, Q.; Yu, C.; Luo, J.; Doyle-Davis, K.; Li, R.; Sham, T.-K.; Sun, X. Gradiently Sodiated Alucone as an Interfacial Stabilizing Strategy for Solid-State Na Metal Batteries. *Advanced Functional Materials* **2020**, *30* (22), 2001118. https://doi.org/10.1002/adfm.202001118.

(108) Yue, J.; Han, F.; Fan, X.; Zhu, X.; Ma, Z.; Yang, J.; Wang, C. High-Performance All-Inorganic Solid-State Sodium–Sulfur Battery. *ACS Nano* **2017**, *11* (5), 4885–4891. https://doi.org/10.1021/acsnano.7b01445.

(109) Rao, R. P.; Zhang, X.; Phuah, K. C.; Adams, S. Mechanochemical Synthesis of Fast Sodium Ion Conductor $Na_{11}Sn_2PSe_{12}$ Enables First Sodium–Selenium All-Solid-State Battery. *J. Mater. Chem. A* **2019**, *7* (36), 20790–20798. https://doi.org/10.1039/C9TA06279C.

(110) Wan, H.; Mwizerwa, J. P.; Qi, X.; Xu, X.; Li, H.; Zhang, Q.; Cai, L.; Hu, Y.-S.; Yao, X. Nanoscaled Na_3PS_4 Solid Electrolyte for All-Solid-State FeS_2/Na Batteries with Ultrahigh Initial Coulombic Efficiency of 95% and Excellent Cyclic Performances. *ACS Appl. Mater. Interfaces* **2018**, *10* (15), 12300–12304. https://doi.org/10.1021/acsami.8b01805.

(111) Heo, J. W.; Banerjee, A.; Park, K. H.; Jung, Y. S.; Hong, S.-T. New Na-Ion Solid Electrolytes $Na_{4-x}Sn_{1-x}Sb_xS_4$ ($0.02 \leq x \leq 0.33$) for All-Solid-State Na-Ion Batteries. *Advanced Energy Materials* **2018**, *8* (11), 1702716. https://doi.org/10.1002/aenm.201702716.

(112) Murgia, F.; Brighi, M.; Černý, R. Room-Temperature-Operating Na Solid-State Battery with Complex Hydride as Electrolyte. *Electrochemistry Communications* **2019**, *106*, 106534. https://doi.org/10.1016/j.elecom.2019.106534.

(113) Santhosha, A. L.; Medenbach, L.; Palaniselvam, T.; Adelhelm, P. Sodium-Storage Behavior of Exfoliated MoS_2 as an Electrode Material for Solid-State Batteries with Na_3PS_4 as the Solid Electrolyte. *J. Phys. Chem. C* **2020**, *124* (19), 10298–10305. https://doi.org/10.1021/acs.jpcc.0c00387.

(114) Chi, X.; Liang, Y.; Hao, F.; Zhang, Y.; Whiteley, J.; Dong, H.; Hu, P.; Lee, S.; Yao, Y. Tailored Organic Electrode Material Compatible with Sulfide Electrolyte for Stable All-Solid-State Sodium Batteries. *Angewandte Chemie International Edition* **2018**, *57* (10), 2630–2634. https://doi.org/10.1002/anie.201712895.

(115) Hao, F.; Chi, X.; Liang, Y.; Zhang, Y.; Xu, R.; Guo, H.; Terlier, T.; Dong, H.; Zhao, K.; Lou, J.; Yao, Y. Taming Active Material-Solid Electrolyte Interfaces with Organic Cathode for All-Solid-State Batteries. *Joule* **2019**, *3* (5), 1349–1359. https://doi.org/10.1016/j.joule.2019.03.017.

(116) Moon, C. K.; Lee, H.-J.; Park, K. H.; Kwak, H.; Heo, J. W.; Choi, K.; Yang, H.; Kim, M.-S.; Hong, S.-T.; Lee, J. H.; Jung, Y. S. Vacancy-Driven Na+ Superionic Conduction in

New Ca-Doped Na_3PS_4 for All-Solid-State Na-Ion Batteries. *ACS Energy Lett.* **2018**, *3* (10), 2504–2512. https://doi.org/10.1021/acsenergylett.8b01479.

(117) Fan, X.; Yue, J.; Han, F.; Chen, J.; Deng, T.; Zhou, X.; Hou, S.; Wang, C. High-Performance All-Solid-State Na–S Battery Enabled by Casting–Annealing Technology. *ACS Nano* **2018**, *12* (4), 3360–3368. https://doi.org/10.1021/acsnano.7b08856.

(118) Tan, D. H. S.; Wu, E. A.; Nguyen, H.; Chen, Z.; Marple, M. A. T.; Doux, J.-M.; Wang, X.; Yang, H.; Banerjee, A.; Meng, Y. S. Elucidating Reversible Electrochemical Redox of Li_6PS_5Cl Solid Electrolyte. *ACS Energy Lett.* **2019**, *4* (10), 2418–2427. https://doi.org/10.1021/acsenergylett.9b01693.

(119) Tian, Y.; Shi, T.; Richards, W. D.; Li, J.; Kim, J. C.; Bo, S.-H.; Ceder, G. Compatibility Issues between Electrodes and Electrolytes in Solid-State Batteries. *Energy Environ. Sci.* **2017**, *10* (5), 1150–1166. https://doi.org/10.1039/C7EE00534B.

(120) Guo, Y.; Li, H.; Zhai, T. Reviving Lithium-Metal Anodes for Next-Generation High-Energy Batteries. *Advanced Materials* **2017**, *29* (29), 1700007. https://doi.org/10.1002/adma.201700007.

(121) Doux, J.-M.; Nguyen, H.; Tan, D. H. S.; Banerjee, A.; Wang, X.; Wu, E. A.; Jo, C.; Yang, H.; Meng, Y. S. Stack Pressure Considerations for Room-Temperature All-Solid-State Lithium Metal Batteries. *Advanced Energy Materials* **2020**, *10* (1), 1903253. https://doi.org/10.1002/aenm.201903253.

(122) Fan, L.; Wei, S.; Li, S.; Li, Q.; Lu, Y. Recent Progress of the Solid-State Electrolytes for High-Energy Metal-Based Batteries. *Advanced Energy Materials* **2018**, *8* (11), 1702657. https://doi.org/10.1002/aenm.201702657.

(123) Nam, Y. J.; Cho, S.-J.; Oh, D. Y.; Lim, J.-M.; Kim, S. Y.; Song, J. H.; Lee, Y.-G.; Lee, S.-Y.; Jung, Y. S. Bendable and Thin Sulfide Solid Electrolyte Film: A New Electrolyte Opportunity for Free-Standing and Stackable High-Energy All-Solid-State Lithium-Ion Batteries. *Nano Lett.* **2015**, *15* (5), 3317–3323. https://doi.org/10.1021/acs.nanolett.5b00538.

(124) Tan, D. H. S.; Banerjee, A.; Deng, Z.; Wu, E. A.; Nguyen, H.; Doux, J.-M.; Wang, X.; Cheng, J.; Ong, S. P.; Meng, Y. S.; Chen, Z. Enabling Thin and Flexible Solid-State Composite Electrolytes by the Scalable Solution Process. *ACS Appl. Energy Mater.* **2019**, *2* (9), 6542–6550. https://doi.org/10.1021/acsaem.9b01111.

(125) Nguyen, H.; Banerjee, A.; Wang, X.; Tan, D.; Wu, E. A.; Doux, J.-M.; Stephens, R.; Verbist, G.; Meng, Y. S. Single-Step Synthesis of Highly Conductive Na_3PS_4 Solid Electrolyte for Sodium All Solid-State Batteries. *Journal of Power Sources* **2019**, *435*, 126623. https://doi.org/10.1016/j.jpowsour.2019.05.031.

(126) Lau, J.; DeBlock, R. H.; Butts, D. M.; Ashby, D. S.; Choi, C. S.; Dunn, B. S. Sulfide Solid Electrolytes for Lithium Battery Applications. *Advanced Energy Materials* **2018**, *8* (27), 1800933. https://doi.org/10.1002/aenm.201800933.

(127) Ohta, N.; Takada, K.; Sakaguchi, I.; Zhang, L.; Ma, R.; Fukuda, K.; Osada, M.; Sasaki, T. $LiNbO_3$-Coated $LiCoO_2$ as Cathode Material for All Solid-State Lithium Secondary

Batteries. *Electrochemistry Communications* **2007**, *9* (7), 1486–1490. https://doi.org/10.1016/j.elecom.2007.02.008.

(128) Huang, B.; Zhao, Z.; Sun, Y.; Wang, M.; Chen, L.; Gu, Y. Lithium-Ion Conductor $LiAlO_2$ Coated $LiNi_{0.8}Mn_{0.1}Co_{0.1}O_2$ as Cathode Material for Lithium-Ion Batteries. *Solid State Ionics* **2019**, *338*, 31–38. https://doi.org/10.1016/j.ssi.2019.05.005.

(129) Zhu, Y.-R.; Yi, T.-F.; Zhu, R.-S.; Zhou, A.-N. Increased Cycling Stability of $Li_4Ti_5O_{12}$-Coated $LiMn_{1.5}Ni_{0.5}O_4$ as Cathode Material for Lithium-Ion Batteries. *Ceramics International* **2013**, *39* (3), 3087–3094. https://doi.org/10.1016/j.ceramint.2012.09.088.

(130) Chan, H.-W.; Duh, J.-G.; Sheen, S.-R. Electrochemical Performance of LBO-Coated Spinel Lithium Manganese Oxide as Cathode Material for Li-Ion Battery. *Surface and Coatings Technology* **2004**, *188–189*, 116–119. https://doi.org/10.1016/j.surfcoat.2004.08.065.

(131) Kendall, K.; Kendall, M. *High-Temperature Solid Oxide Fuel Cells for the 21st Century*; Academic Press, 2016. https://doi.org/10.1016/c2011-0-09278-5.

(132) Evans, A.; Bieberle-Hütter, A.; Rupp, J. L. M.; Gauckler, L. J. Review on Microfabricated Micro-Solid Oxide Fuel Cell Membranes. *Journal of Power Sources* **2009**, *194* (1), 119–129. https://doi.org/10.1016/j.jpowsour.2009.03.048.

(133) Su, P.-C.; Chao, C.-C.; Shim, J. H.; Fasching, R.; Prinz, F. B. Solid Oxide Fuel Cell with Corrugated Thin Film Electrolyte. *Nano Letters* **2008**, *8* (8), 2289–2292. https://doi.org/10.1021/nl800977z.

(134) An, J.; Kim, Y. B.; Park, J.; Gür, T. M.; Prinz, F. B. Three-Dimensional Nanostructured Bilayer Solid Oxide Fuel Cell with 1.3 W/Cm2 at 450 C. *Nano Letters* **2013**, *13* (9), 4551–4555. https://doi.org/10.1021/nl402661p.

(135) Ji, S.; Cho, G. Y.; Yu, W.; Su, P. C.; Lee, M. H.; Cha, S. W. Plasma-Enhanced Atomic Layer Deposition of Nanoscale Yttria-Stabilized Zirconia Electrolyte for Solid Oxide Fuel Cells with Porous Substrate. *ACS Applied Materials and Interfaces* **2015**, *7* (5), 2998–3002. https://doi.org/10.1021/am508710s.

(136) Ju, Y.-W.; Jun, A.; Inoishi, A.; Ida, S.; Lim, T.; Kim, G.; Ishihara, T. Growth of Thin-Film Layered Perovskite Cathodes by Pulsed Laser Deposition and Their Electrochemical Studies in IT-SOFCs. *Journal of The Electrochemical Society* **2014**, *161* (6), F698–F702. https://doi.org/10.1149/2.020406jes.

(137) Wang, F.; Brito, M. E.; Yamaji, K.; Cho, D. H.; Nishi, M.; Kishimoto, H.; Horita, T.; Yokokawa, H. Effect of Polarization on Sr and Zr Diffusion Behavior in LSCF/GDC/YSZ System. *Solid State Ionics* **2014**, *262*, 454–459. https://doi.org/10.1016/j.ssi.2014.04.002.

(138) Chang, I.; Woo, S.; Lee, M. H.; Shim, J. H.; Piao, Y.; Cha, S. W. Characterization of Porous Pt Films Deposited via Sputtering. *Applied Surface Science* **2013**, *282*, 463–466. https://doi.org/10.1016/j.apsusc.2013.05.153.

(139) Wang, X.; Huang, H.; Holme, T.; Tian, X.; Prinz, F. B. Thermal Stabilities of Nanoporous Metallic Electrodes at Elevated Temperatures. *Journal of Power Sources* **2008**, *175* (1), 75–81. https://doi.org/10.1016/j.jpowsour.2007.09.066.

(140) Chang, I.; Ji, S.; Park, J.; Lee, M. H.; Cha, S. W. Ultrathin YSZ Coating on Pt Cathode for High Thermal Stability and Enhanced Oxygen Reduction Reaction Activity. *Advanced Energy Materials* **2015**, *5* (10), 1402251. https://doi.org/10.1002/aenm.201402251.

(141) Lee, Y. H.; Cho, G. Y.; Chang, I.; Ji, S.; Kim, Y. B.; Cha, S. W. Platinum-Based Nanocomposite Electrodes for Low-Temperature Solid Oxide Fuel Cells with Extended Lifetime. *Journal of Power Sources* **2016**, *307*, 289–296. https://doi.org/10.1016/j.jpowsour.2015.12.089.

(142) Choi, H. J.; Kim, M.; Neoh, K. C.; Jang, D. Y.; Kim, H. J.; Shin, J. M.; Kim, G. T.; Shim, J. H. High-Performance Silver Cathode Surface Treated with Scandia-Stabilized Zirconia Nanoparticles for Intermediate Temperature Solid Oxide Fuel Cells. *Advanced Energy Materials* **2017**, *7* (4), 1601956. https://doi.org/10.1002/aenm.201601956.

(143) Minh, N. Q. Ceramic Fuel Cells. J*ournal of American Ceramic Society* **1993**, *76* (3), 563–588. https://doi.org/10.1016/B978-012654640-8/50028-6.

(144) O'Hayre, R.; Cha, S.-W.; Colella, W.; Prinz, F. B. *Fuel Cell Fundamentals*; John Wiley & Sons New York, 2006.

(145) Noh, H.-S.; Son, J.-W.; Lee, H.; Ji, H.-I.; Lee, J.-H.; Lee, H.-W. Suppression of Ni Agglomeration in PLD Fabricated Ni-YSZ Composite for Surface Modification of SOFC Anode. *Journal of the European Ceramic Society* **2010**, *30* (16), 3415–3423. https://doi.org/10.1016/j.jeurceramsoc.2010.07.035.

(146) Thornton, J. A. The Microstructure of Sputter-deposited Coatings. *Journal of Vacuum Science & Technology A: Vacuum, Surfaces, and Films* **1986**, *4* (6), 3059–3065. https://doi.org/10.1116/1.573628.

(147) Gong, Y.; Ji, W.; Zhang, L.; Li, M.; Xie, B.; Wang, H.; Jiang, Y.; Song, Y. Low Temperature Deposited (Ce,Gd)O 2-x Interlayer for $La_{0.6}Sr_{0.4}Co_{0.2}Fe_{0.8}O_3$ Cathode Based Solid Oxide Fuel Cell. *Journal of Power Sources* **2011**, *196* (5), 2768–2772. https://doi.org/10.1016/j.jpowsour.2010.10.070.

(148) Jung, W.; Kim, J. J.; Tuller, H. L. Investigation of Nanoporous Platinum Thin Films Fabricated by Reactive Sputtering: Application as Micro-SOFC Electrode. *Journal of Power Sources* **2015**, *275*, 860–865. https://doi.org/10.1016/j.jpowsour.2014.11.084.

(149) Kwon, C.-W.; Son, J.-W.; Lee, J.-H.; Kim, H.-M.; Lee, H.-W.; Kim, K.-B. High-Performance Micro-Solid Oxide Fuel Cells Fabricated on Nanoporous Anodic Aluminum Oxide Templates. *Advanced Functional Materials* **2011**, *21* (6), 1154–1159. https://doi.org/10.1002/adfm.201002137.

(150) Park, J.; Lee, Y.; Chang, I.; Lee, W.; Cha, S. W. Engineering of the Electrode Structure of Thin Film Solid Oxide Fuel Cells. *Thin Solid Films* **2015**, *584*, 125–129. https://doi.org/10.1016/j.tsf.2014.11.018.

(151) Hong, S.; Bae, J.; Koo, B.; Kim, Y. B. High-Performance Ultra-Thin Film Solid Oxide Fuel Cell Using Anodized-Aluminum-Oxide Supporting Structure. *Electrochemistry Communications* **2014**, *47*, 1–4. https://doi.org/10.1016/j.elecom.2014.07.008.

(152) Lim, Y.; Hong, S.; Bae, J.; Yang, H.; Kim, Y. B. Influence of Deposition Temperature on the Microstructure of Thin-Film Electrolyte for SOFCs with a Nanoporous AAO Support Structure. *International Journal of Hydrogen Energy* **2017**, *42* (15), 10199–10207. https://doi.org/10.1016/j.ijhydene.2017.03.148.

(153) Cho, S.; Kim, Y.; Kim, J.; Manthiram, A.; Wang, H. High Power Density Thin Film SOFCs with YSZ / GDC Bilayer Electrolyte. *Electrochimica Acta* **2011**, *56* (16), 5472–5477. https://doi.org/10.1016/j.electacta.2011.03.039.

(154) Hoon, J.; Min, S.; Kim, B.; Lee, J.; Joong, K.; Kim, H.; Ji, H.; Son, J. Sintered Powder-Base Cathode over Vacuum-Deposited Thin- Fi Lm Electrolyte of Low-Temperature Solid Oxide Fuel Cell : Performance and Stability. *Electrochimica Acta* **2019**, *296*, 1055–1063. https://doi.org/10.1016/j.electacta.2018.11.018.

(155) Qian, J.; Zhu, Z.; Dang, J.; Jiang, G.; Liu, W. Improved Performance of Solid Oxide Fuel Cell with Pulsed Laser Deposited Thin Film Ceria – Zirconia Bilayer Electrolytes on Modified Anode Substrate. *Electrochimica Acta* **2013**, *92*, 243–247. https://doi.org/10.1016/j.electacta.2013.01.017.

(156) Noh, H.-S.; Lee, H.; Kim, B.-K.; Lee, H.-W.; Lee, J.-H.; Son, J.-W. Microstructural Factors of Electrodes Affecting the Performance of Anode-Supported Thin Film Yttria-Stabilized Zirconia Electrolyte (~1μm) Solid Oxide Fuel Cells. *Journal of Power Sources* **2011**, *196* (17), 7169–7174. https://doi.org/10.1016/j.jpowsour.2010.09.038.

(157) Lu, Z.; Hardy, J.; Templeton, J.; Stevenson, J.; Fisher, D.; Wu, N.; Ignatiev, A. Performance of Anode-Supported Solid Oxide Fuel Cell with Thin Bi-Layer Electrolyte by Pulsed Laser Deposition. *Journal of Power Sources* **2012**, *210*, 292–296. https://doi.org/10.1016/j.jpowsour.2012.03.036.

(158) Noh, H. S.; Yoon, K. J.; Kim, B. K.; Je, H. J.; Lee, H. W.; Lee, J. H.; Son, J. W. The Potential and Challenges of Thin-Film Electrolyte and Nanostructured Electrode for Yttria-Stabilized Zirconia-Base Anode-Supported Solid Oxide Fuel Cells. *Journal of Power Sources* **2014**, *247*, 105–111. https://doi.org/10.1016/j.jpowsour.2013.08.072.

(159) Gao, Z.; Zenou, V. Y.; Kennouche, D.; Marks, L.; Barnett, S. A. Solid Oxide Cells with Zirconia/Ceria Bi-Layer Electrolytes Fabricated by Reduced Temperature Firing. *Journal of Materials Chemistry A* **2015**, *3*, 9955–9964. https://doi.org/10.1039/c5ta01964h.

(160) Yu, C.-Y.; Park, J.-S.; Jung, H.-G.; Chung, K.-Y.; Aurbach, D.; Sun, Y.-K.; Myung, S.-T. $NaCrO_2$ Cathode for High-Rate Sodium-Ion Batteries. *Energy Environ. Sci.* **2015**, *8* (7), 2019–2026. https://doi.org/10.1039/C5EE00695C.

(161) Chen, S.; Niu, C.; Lee, H.; Li, Q.; Yu, L.; Xu, W.; Zhang, J.-G.; Dufek, E. J.; Whittingham, M. S.; Meng, S.; Xiao, J.; Liu, J. Critical Parameters for Evaluating Coin Cells and Pouch Cells of Rechargeable Li-Metal Batteries. *Joule* **2019**, *3* (4), 1094–1105. https://doi.org/10.1016/j.joule.2019.02.004.